Constrained Parameterization of the Multichannel Analysis of Surface Waves Approach with Application at Yuma Proving Ground, Arizona

By

Jacob Tyler Schwenk
B.S., University of Kansas, 2009

Submitted to the graduate degree program in Geology and the Graduate Faculty of the University of Kansas in partial fulfillment of the requirements for the degree of Master of Science.

_____

Chairperson Richard D. Miller

_____

Georgios P. Tsoflias

_____

Jennifer A. Roberts

_____

Steven D. Sloan

Date Defended: July 11, 2013

The Thesis Committee for Jacob Tyler Schwenk

certifies that this is the approved version of the following thesis:

Constrained Parameterization of the Multichannel Analysis of Surface Waves Approach with Application at Yuma Proving Ground, Arizona

_____

Chairperson Richard D. Miller

Date approved: July 11, 2013

Abstract

Field data from Yuma Proving Ground, Arizona was used to test the feasibility of merging common multichannel analysis of surface waves (MASW) processing routines with mode-consistent shear-wave refraction traveltime tomography and synthetic modeling to optimize and constrain inversion results. Shear-wave first-arrival refraction tomography was used to enhance layer-model resolution and refine the MASW layer model with independent body-wave information. Shear-wave tomograms suggested a high-velocity layer, not found in initial 'smooth' MASW velocity sections that were used as initial models for tomographic inversion. Increasing the stratification of the MASW layer model, to generally match tomogram structure, resulted in a higher-resolution MASW model constrained through joint analysis. This mutual analysis of shear-wave velocity (*Vs*) provided multiplicity to the structural interpretation of the site. Constrained-parameterization MASW results, compressional-wave tomography (*Vp*:*Vs* ratio), and density well logs populated a 2D model for numerical modeling, which was manually updated over several iterations to converge upon the site's first-arrival and dispersion characteristics. Further evaluation of the synthetic seismograms gave insight into the relationship between acquisition geometry (offset selection) and the associated dispersion-image character. Furthermore, modeling gave a secondary measurement on depth to half-space, velocity structure, and relative *Vp*:*Vs* ratios, which formulated a final MASW profile. The gradual change of the earth model, given an evolving hierarchy of constraint, is seen as the main finding of this thesis. The calculated movement towards a higher-resolution inversion based on joint geophysical measurements, analysis, and interpretation, engenders a constrained-parameterization solution with highest confidence.

Acknowledgments

I thank Rick Miller, Shelby Peterie, Brett Bennett, Benjamin Rickards, Joseph Kearns, Owen Metheny, Anthony Wedel, Brett Wedel, and Joe Anderson for their work in acquiring the data that this research was based on. Many stories originated from the two acquisition phases and I am grateful for their labors.

Special thanks goes to Rick for making all this possible and bringing a healthy mix of levity and seriousness into the halls of Moore. I also thank my committee members, Julian Ivanov, and Shelby Peterie for their time and thoughts throughout my career at the KGS on my various research projects, problems, and concerns. I thank my family: Philip, Dee Ann, Lauren, and the little man Gabriel (Schwenk) for their continual support during my tenure at KU. I also thank my grandparents Glen and Dee, uncles and aunts Brett, Cathy, Bruce, and Johna (Butler) and note their support during my time at JCCC; your investment paid dividends. Lastly, I thank my fellow Jayhawks, graduate and undergrad alike, for their support and help throughout my scholarly career. I wouldn't have made it without all of you.

TABLE OF CONTENTS

ABSTRACT ..... **III**
ACKNOWLEDGMENTS ..... **IV**
1. INTRODUCTION **1**
1.1. REGIONAL AND LOCAL GEOLOGY 4
1.2. MASW METHOD 8
2. DISPERSION IMAGING **11**
2.1. IMAGING METHODS 16
2.2. IMPLICATIONS WITH APPLICATION 19
3. INVERSION THEORY **21**
3.1. FORWARD MODELING 21
3.2. LEAST-SQUARES APPROACH 23
3.3. GLOBAL OR STOCHASTIC APPROACH 25
3.4. FUNDAMENTAL VS. MULTI-MODE COMPLEXITY 26
3.5. MODEL SPACE AND PARAMETERIZATION 27
4. DATA ACQUISITION **32**
5. PROCESSING METHODS **37**
5.1. PRELIMINARY MASW 40
5.2. *VS*-JARS APPROACH 50
5.3. *VP*-TOMOGRAPHY (JARS) 55
6. CONSTRAINED-PARAMETERIZATION MASW DISCUSSION **60**
6.1. *VS*-JARS AND MASW 60
6.2. RMS ERROR 64
6.3. P-WAVE TOMOGRAPHY (JARS) 65
7. CONSTRAINED INVERSION CONCLUSION **68**
8. MODELING OF SITE CHARACTERISTICS **70**
8.1. MODEL GENERATION 71
8.2. ACQUISITION EFFECTS 76
8.3. MODELING CONCLUSIONS 81
9. FINAL THOUGHTS **83**
10. REFERENCES **84**
11. APPENDIX I **90**
12. APPENDIX II **91**
13. APPENDIX III **93**
14. APPENDIX IV **94**

TABLE OF FIGURES

FIGURE 1: (A-C) LARGE- TO SMALL-SCALE MAP SEQUENCE OF THE YUMA PROVING GROUND TUNNEL DETECTION SITE. 2

FIGURE 2: PHYSIOGRAPHIC REGIONS OF THE AREA SOUTH OF QUARTZITE, AZ (AFTER EASTMAN, 2007). 5

FIGURE 3: STRUCTURAL MAP WITH GEOLOGIC OVERLAY OF THE NORTH AND SOUTH TRIGO PEAKS AND THE SOUTHERN EXTENT OF THE DOME ROCK MOUNTAINS (AFTER SHERROD AND TOSDAL, 1991). 6

FIGURE 4: GEOLOGIC LOG INTERPRETATION AFTER RICKARDS (2011). 7

FIGURE 5: LEFT) DIAGRAM OF A PHASE-SHIFTED SV REFLECTION AND AN EVANESCENT CRITICALLY REFRACTED P-WAVE INDUCED FROM AN INCIDENT POSTCRITICAL REFLECTED SV WAVE. LARGE ARROWS DEPICT PARTICLE MOTION, SMALL ARROWS AND PERPENDICULAR LINES GIVE PLANE-WAVE PROPAGATION DIRECTION. RIGHT) THE INTERFERENCE OF THE EVANESCENT P-WAVE AND S_V-PARTICLE MOTION AT THE FREE SURFACE PRODUCE RAYLEIGH WAVES. 12

FIGURE 6: LEFT) DISPLACEMENT COMPONENTS SHOWN AS A FUNCTION OF PERIOD FOR ONE POINT IN THE SUB-SURFACE. RIGHT) COMPONENT DISPLACEMENTS AS A FUNCTION OF DEPTH. 13

FIGURE 7: REFERENCE SHOT GATHER FROM THE YUMA SITE WITH RAYLEIGH-WAVE DISPERSION HIGHLIGHTED. 15

FIGURE 8: REFERENCE DISPERSION CURVE FROM THE YUMA SITE. 15

FIGURE 9: GRAPHICAL REPRESENTATION OF THE P-τ METHOD, WITH THE DATA TRANSFORMED FROM THE OFFSET-TIME DOMAIN TO THE SLOWNESS VS. TIME DOMAIN (YILMAZ, 2001) 18

FIGURE 10: A FOUR-TRACE TRANSFORM USING (LEFT TO RIGHT): F-K METHOD, P-τ METHOD, AND PHASE-SHIFT METHOD (AFTER DAL MORO ET AL., 2003). 20

FIGURE 11: RESULTS AFTER DAL MORO ET AL. (2003) WITH A SEQUENCE OF DISPERSION CURVES CALCULATED FROM 24-GEOPHONE GATHERS WITH THE A) F-K METHOD, B) P-τ METHOD, AND C) PHASE SHIFT METHOD. COLUMN 1 IS WITH A (0-2-20-30) BANDPASS FILTER, COLUMN 2 IS THE SAME AS COLUMN 1 WITH A NORMALIZATION FACTOR, AND COLUMN 3 IS WITH A (0-3-50-70) BANDPASS FILTER. 20

FIGURE 12: AQUALOCK GEOLOGIC SAMPLING SYSTEM AT WORK ON THE YPG SITE. 32

FIGURE 13: PHOTO OF THE WEIGHT DROP USED FOR P-WAVE REFRACTION AND MASW PROCESSING WITH THE TRIGO PEAKS IN THE BACKGROUND. 33

FIGURE 14: SHEAR-BLOCK SETUP FOR SHEAR-WAVE TOMOGRAPHY. THE OPPOSITE DIRECTION OF INITIAL MOTION IS NOT SHOWN IN THE DIAGRAM. THIS IS A SIMPLIFICATION, BOTH S_V AND S_H SOURCES WILL GENERATE BOTH SHEAR-WAVE MODES; HOWEVER ONE IS DOMINANT. 34

FIGURE 15: PICTURE OF THE IVI MINIVIB SYSTEM USED AT YPG WITH THREE DIFFERENT ORIENTATIONS OF THE HYDRAULIC MASS: TOP LEFT) S_H-; BOTTOM LEFT) S_V-; RIGHT) P-WAVE. NOTE THE WAFFLE PLATE USED FOR SHEAR GENERATION IN THE LOWER LEFT IMAGE AND THAT THE SURVEY LINE IS PARALLEL TO THE LONG AXIS OF THE MINIVIB. 35

FIGURE 16: GENERALIZED WORKFLOW FOR A CONSTRAINED-PARAMETERIZATION MASW APPROACH. PRELIMINARY, FIRST-RUN MASW ALLOWS A *VS*-JARS/JARS APPLICATION, THE RESULTS OF WHICH MAY BE USED TO UPDATE THE LAYER MODEL OF THE NEXT GENERATION MASW INVERSION. LATER SECTIONS WILL DISCUSS THE ADDITION OF SYNTHETIC MODELING FOR ADDITIONAL CONSTRAINT ON DISPERSION INTERPRETATION AND LAYER-MODEL REFINEMENT. ARROWS DEPICT UPDATES WITH EACH ADDITIVE CONSTRAINT OR INFORMATION. 38

FIGURE 17: FOUR 47 INCH TELEVISION SETUP USED TO PICK DISPERSION CURVES. 39

FIGURE 18: DISPERSION CURVE SHOWING GOOD SIGNAL TO 80 HZ WITH VARIABLE HM CONTAMINATION ABOVE 30 HZ. SQUARES HIGHLIGHT SEVERAL INSTANCES OF THE COMPETING SIGNAL BETWEEN THE FUNDAMENTAL AND THE HIGHER-MODE. THE BOLD BLACK LINE HIGHLIGHTS A QUESTIONABLE TRAJECTORY FOR THE FUNDAMENTAL. 42

FIGURE 19: LEFT) UNMUTED SHOT GATHER. RIGHT) MUTED SHOT GATHER. 43

FIGURE 20: UPPER) UNMUTED RECORD WITH STRONG HIGHER-MODE CONTAMINATION PAST 30 HZ. LOWER) MUTED RECORD ABOVE AN APPROXIMATE PHASE VELOCITY OF 450 M/S WITH INCREASED BANDWIDTH TO 80 HZ. 44

FIGURE 21: WELL LOG SUITE FOR WELL 11. LOGS INCLUDE: TEMPERATURE, DENSITY, GAMMA, NEUTRON, AND RESISTIVITY/CONDUCTIVITY. 47

FIGURE 22: INITIAL, FEW-LAYER MASW INVERSION OF THE YPG DATA. NOTE THE LACK OF STRATIFICATION AND APPARENT SMOOTH TRANSITION TO 9 M. 49

FIGURE 23: REPRESENTATIVE S_H-WAVE HAMMER SHOT GATHER OF REVERSED AND VERTICALLY STACKED POLARITIES, WITH FIRST-ARRIVAL PICKS (IN GREEN). 50

FIGURE 24: S_H-WAVE REFRACTION TOMOGRAM USING *VS*-JARS APPROACH. NOTE THE HIGH-VELOCITY LAYER AT APPROXIMATELY 6 M. 51

FIGURE 25: CONSTRAINED MASW *VS* SECTION. NOTE THE INCORPORATION OF THE HVL AT 6M. 52

FIGURE 26: RESULTS OF REPEATED METHODOLOGY FOR LINE 3. NOTE THE SIMILAR STRUCTURAL PATTERN OF THE S_H- AND S_V-METHODS AND ALSO THE MISMATCH OF THE SV-VIBE VELOCITY VALUES. 53

FIGURE 27: TOMOGRAM COMPARISON FOR LINE 2. NOTE THE STRUCTURAL AND VELOCITY AGREEMENT BETWEEN THE S_H- AND S_V-METHODS. 54

FIGURE 28: LINE 2 *VP*-TOMOGRAPHY RESULTS AND *VP*:*VS* RATIO MAP. 55

FIGURE 29: LINE 3 *VP*-TOMOGRAM AND *VP*:*VS* RATIO MAP. 56

FIGURE 30: FIRST-ARRIVAL GATHER WITH 3-LAYER REFRACTION INTERPRETATION. 57

FIGURE 31: GRAPH OF A MOVING 20-POINT LEAST-SQUARES FIT OF THE FIRST-ARRIVAL DATA GIVEN IN FIGURE 29. NOTE THE OSCILLATION OF APPARENT VELOCITY NOT INTERPRETED WITH THE STANDARD 3-LAYER ASSESSMENT. 58

FIGURE 32: FIGURE DISPLAYING DATA FROM 274 BOREHOLES, WITH POISSON'S RATIO LINES IN VARIOUS COLORS (AFTER BOORE, 2007). NOTE THE LOWER TREND CENTERED BELOW OR IN THE VICINITY OF 0.3 (*VP*:*VS*-1.87, THE GREEN LINE) WITH MANY VALUES BELOW 0.2 (*VP*:*VS*-1.63, THE LOWEST PINK LINE). YPG DATA AVERAGED ACROSS LAYERS IS OVERLAIN FOR COMPARISON. 67

FIGURE 33: LEFT) SYNTHETIC SHOT GATHER OF FINAL LAYER MODEL. RIGHT) REFERENCE FIELD GATHER FOR THE YPG SITE. NOTE THE RELATIVE MATCH OF THE FIRST-ARRIVAL TREND. 72

FIGURE 34: SYNTHETIC MODEL WITH EQUIVALENT FINAL LINE 2 AND LINE 3 CONSTRAINED-PARAMETERIZATION MASW RESULTS TO HALF-SPACE DEPTH. 75

FIGURE 35: GRAPH OF PHASE-VELOCITY VARIATION WITH SPREAD LENGTH. ALL SUBSETS HAVE A 1 M SOURCE OFFSET, WHERE SHORT REFERS TO A 78M 65-GEOPHONE SPREAD AND LONG REFERS TO A 178M 147-GEOPHONE SPREAD. AT MAXIMUM DEVIATION, PERCENT DIFFERENCE IS UNDER 6% FOR CORRESPONDING SPREAD LENGTHS. THE SLIGHT OVERESTIMATION AT HIGH-FREQUENCY MODEL DATA, IN COMPARISON TO THE THEORETICAL CURVE, IS A RESULT OF THE AUTOMATIC PICKING ROUTINE. 76

FIGURE 36: DISPERSION CURVE COMPARISON FOR THE FULL 147-GEOPHONE SPREAD LENGTH (178 M SPREAD: SYNTHETIC DATA TO LEFT, FIELD DATA TO RIGHT). NOTE THE HIGHER-AMPLITUDE HM ENERGY IN THE FIELD DATA. 78

FIGURE 37: DISPERSION CHARACTER COMPARISON FOR THE OPTIMIZED 65-GEOPHONE SPREAD LENGTH (78 M SPREAD: SYNTHETIC DATA TO LEFT, FIELD DATA TO RIGHT). NOTE THE AMPLIFIED HM INTERFERENCE AT FREQUENCIES GREATER THAN 25 HZ ON THE FIELD DATA. 78

FIGURE 38: SEQUENCE OF DISPERSION CURVES PREPARED FROM DIFFERENT ACQUISITION PARAMETER SUBSETS: LEFT) MODEL DATA, RIGHT) FIELD DATA. 79

FIGURE 39: MUTED GATHERS OF THE MODEL (LEFT) AND FIELD (RIGHT) DATA. NOTE THE IMPROVEMENT IN OVERALL QUALITATIVE MATCH BETWEEN THE CURVES' MODAL TRENDS. 80

1. Introduction

A site at the Yuma Proving Ground (YPG) near Yuma, Arizona, has been designated the Joint Tunnel Test Range (JTTR) for use with the Joint Capability Technology Demonstration (JCTD) (ONDCP, 2009). The site is located in the Sonora Desert on the Joint Experimentation Range Complex (JERC) in the North Cibola Range sector of YPG (Figure 1-B). Specifically, the Exploration Services section of the Kansas Geological Survey (KGS) was tasked for the development and testing of anomaly-detection seismic methods and establishing baseline data for future testing at the JTTR.

With the present political and societal pressures on both domestic and foreign border stability, a systematic and reliable means for tunnel detection and delineation is made necessary. For the purposes of discovery, plans were made for the emplacement of tunnels at JERC with funding for the JTTR and the JCTD. A more-perfect procedure can be outlined for future real-world applications by preparing a sterile site for experimentation and methodology enhancement. The emplacement of foreign material and/or the disruption of native substrate will be used to the advantage of geophysical response. The change in bulk composition and the predominant material properties of density (ρ) and elastic moduli (μ, k, etc.) will be associated to anomalous changes in wave-mode properties (*Vp*, *Vs*) that correspond to the excitation of the incident wave field. Due to the unprecedented nature of this experimentation and its theoretical development, there is a requisite need for extensive knowledge of the test site's geophysical properties before the emplacement of tunnel features.

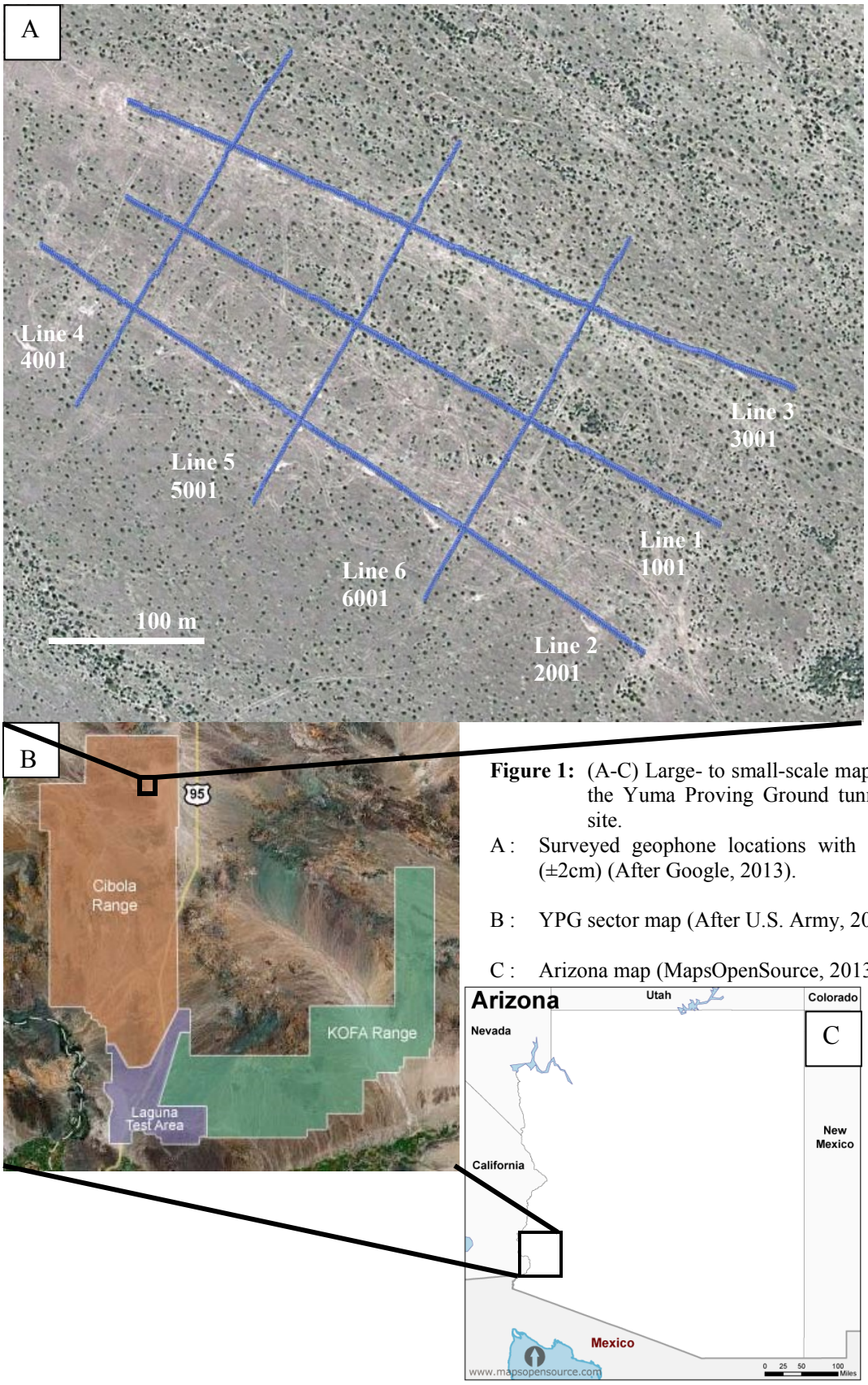

Figure 1: (A-C) Large- to small-scale map sequence of the Yuma Proving Ground tunnel detection site.

A : Surveyed geophone locations with line markers (±2cm) (After Google, 2013).

B : YPG sector map (After U.S. Army, 2010).

C : Arizona map (MapsOpenSource, 2013).

For adequate modeling/method restraint, wave propagation must be understood to the greatest degree possible before and after tunneling activity. As such, a baseline survey was attained during two trips in the summer and fall of 2009; data were collected from July 10th through the 16th and from October 13th through the 17th. This research was funded and designed to process the data collected during these two trips which encompassed a broad spectrum of geophysical sources and sensors (Table 1).

Table 1: List of the various source/receiver methods undertaken at the JTTR site (Miller et al., 2010c).

Line #	Receiver	Source	# Receiver Stations	# Shot Stations	Shots per Station
1,2,3	4.5-Hz V	Weight Drop	340	190	3
4,5,6	4.5-Hz V	Weight Drop	192	115	3
2,3	twin 40-Hz V	Weight Drop	340	190	3
2,3	14.5-Hz H	Vibrator S_H	340	190	2
2,3	14.5-Hz H	Vibrator S_V	340	190	2
2,3	14.5-Hz H	Vibrator S_H (reverse)	340	17	2
2,3	14.5-Hz H	Vibrator S_V (reverse)	340	17	2
2,3	14.5-Hz H	Hammer/Block	340	17	6
Wells 7, 13	3C Uphole	Hammer/Block	n/a	20	9
TOTAL				**>2,200**	

The acquisition strategy allowed for multiple seismic tests of the area through time, before and after the emplacement of tunnel features (see Appendix I). Although it encompasses a small portion of the data set collected and processed, the portion reported on here is centered upon the multichannel analysis of surface waves (MASW). The technique uses the property of Rayleigh-wave dispersion to garner a shear-wave (S-wave) velocity (*Vs*) profile, through standard off-end shooting techniques. The method was studied for enhancements to the standard work-flow that would bring about more stable, constrained, and higher-resolution *Vs* profiles.

The resulting 2D-*Vs* profiles will be compared to shear- and compressional-wave refraction and relative density logs as a correlation tool for model and inversion refinement. These comparisons should validate the layer structure and interval velocities, as well as provide a relative

Vp:*Vs* ratio. Furthermore, seismic modeling will be used to substantiate the geologic model with the production and processing of synthetic seismograms. Synthetic comparisons shall compare the relative match between shot gathers within the x-t domain and look at matching the effects of the domain transformations related to the MASW method, as a means to justify dispersion and acquisition-subset interpretations. These additional and unrelated measurements will be used as *a priori* information to parameterize the inversion scheme. The use of multiple geophysical methods to constrain the solution space, along with additional techniques to broaden both the applicability and information content beyond standard MASW surveying, will engender higher-resolution, more constrained (more 'unique') solutions with more confidence in the final results.

1.1. Regional and Local Geology

Located within the basin and range province of the southwestern United States, the regional geomorphology is denoted by uplifted regions bounded by normal faults in an extensional regime. The extension throughout the area is believed to have started during the early Miocene (Sherrod and Tosdal, 1991; Tosdal, 1990). With respect to physiographic region, the area is located within the Trigo Peaks Area, at the margin of the La Posa Plain (Figure 2) (Eastman, 2007). The site is bounded to the North by the Dome Rock Mountains and to the west and southwest by the North and South Trigo Peaks, respectively. The Tyson Wash to the south-southeast and the Felipe Pass to the south form the primary drainage for the area. The relief throughout the arid region transitions to down-dropped lowlands by alluvial fan and bajada formation along with colluvium deposits of grus, etc. The site lies off the tail of alluvial fans produced from volcanic tuff formations to the west.

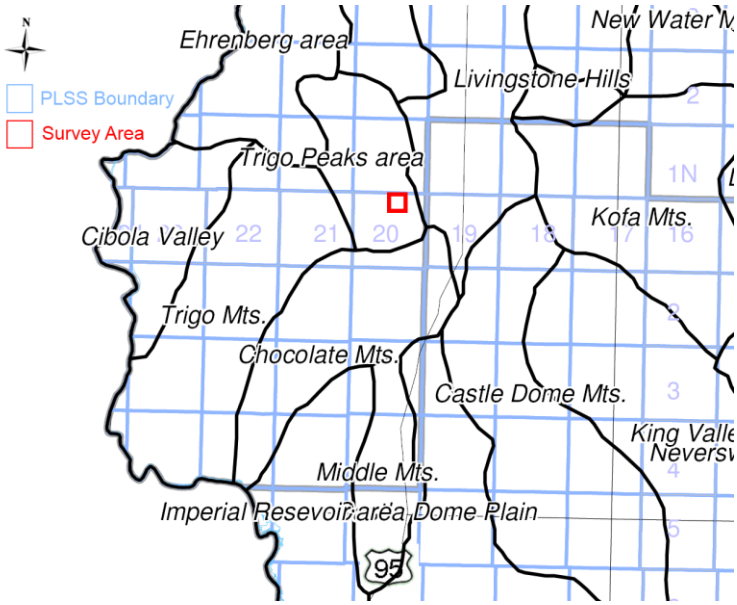

Figure 2: Physiographic regions of the area south of Quartzite, AZ (After Eastman, 2007).

Sherrod and Tosdal (1991) undertook a structural study of the area, denoting general geology and rock ages (Figure 3). The Dome Rock Mountains are composed of metasedimentary rocks of the "Jurassic (?) and the Cretaceous McCoy Mountains Formation," which were then overthrust by Jurassic metavolcanic and plutonic rocks by way of the Late Cretaceous Mule Mountains thrust system (Sherrod and Tosdal, 1991; Tosdal, 1990). The Trigo Peaks are composed of Jurassic granitic structural panels that are tilted to the northeast through normal faulting in a general northeast to southwest extensional regime (Tosdal and Sherrod, 1985). East- to northeast-striking tear faults have dextral strike-slip offsets of up to several kilometers and follow/modify the fabric of the Mule Mountains Thrust (Sherrod and Tosdal, 1991; Tosdal and Sherrod, 1985). The granitic blocks are overlain by distally derived arkosic sandstone (Miocene to Oligocene) and the Felipe Pass silicic tuff sequence sourced from the calderas of the Kofa Mountains to the south during the Miocene (Sherrod and Tosdal, 1991). Between the Dome Rock Mountains and the Trigo Peaks, and along the local drainage valleys, there are bands of Miocene fanglomerates and Holocene to Pleistocene alluvium deposits (Sherrod and Tosdal, 1991).

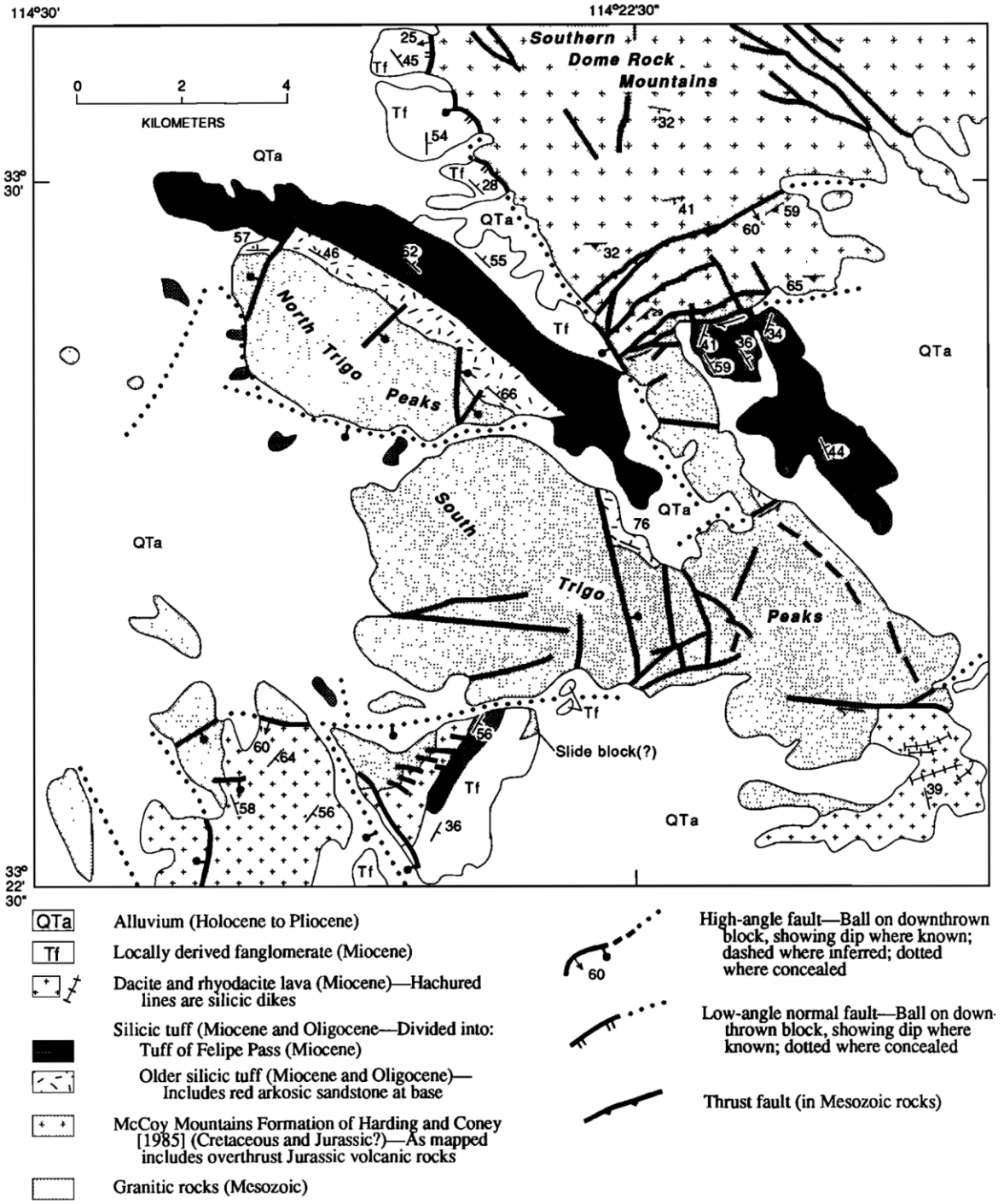

Figure 3: Structural map with geologic overlay of the North and South Trigo Peaks and the southern extent of the Dome Rock Mountains (after Sherrod and Tosdal, 1991).

The site is located at the edge of the La Posa alluvial plain, with soil primarily characterized by SM (USCS) classification and Superstition-Rositas (USDA-NRCS) texture (McDonald et al., 2009; Miller et al., 2010b). Located between two natural drainage ditches, there is a slight dip to the southeast with scattered vegetation. As characteristic of alluvial plains, the locality is denoted by a broad outwash basin with little elevation change across the site. Well logging and sample retrieval generated a suite of geologic logs: gamma, neutron, resistivity, density, and temperature (Davis and Culig, 2009). The substrate contains large amounts of clay and silt, with lesser amounts of coarse- to fine-grained sand. Limited quantities of biotite and chlorite, with larger granules of quartz and feldspar were documented (Miller et al., 2010b). Some work was done to correlate the sedimentary units between wells; however, due to the highly variable nature and sparse and intermittent sampling of the subsurface, the results were deemed unreliable. Nevertheless, figure 4 relates the variable clay-content of the geologic logs across line 3.

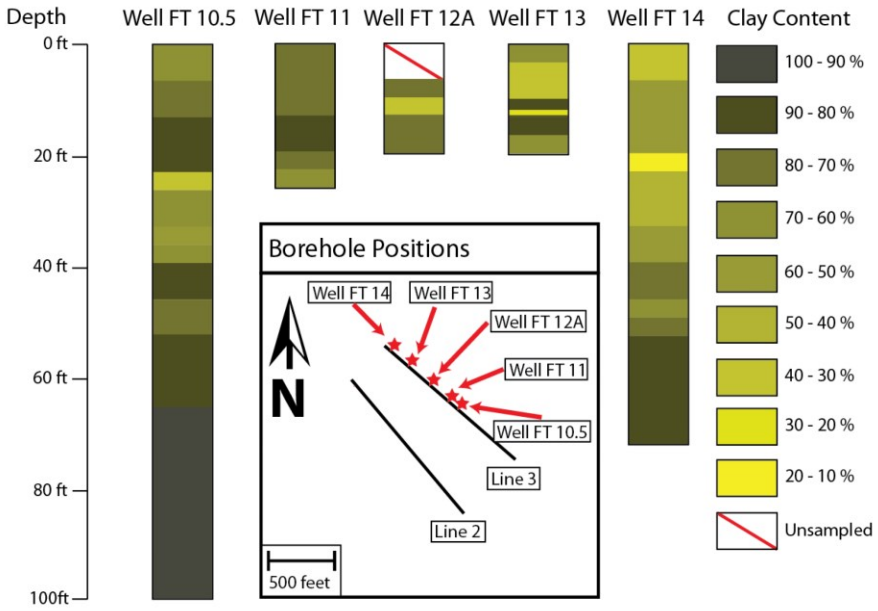

Figure 4: Geologic log interpretation after Rickards (2011).

1.2. MASW Method

During the past several decades, Rayleigh-wave dispersion has increasingly been used to study *Vs*. The multichannel analysis of surface waves (MASW) is used for Rayleigh-wave *Vs* estimations (Miller et al., 1999a). MASW employs a linear line of low frequency (e.g., <10 Hz) vertical geophones, with off-end/in-line source acquisition, to record the local variation in dispersion properties (*Vs*) of the near-surface (<100 m). The shot gathers are then examined using a spectral analysis to retrieve a phase-velocity vs. frequency plot, which is interpreted for dispersion curves. These curves are then inverted, assuming a layered-earth model, to form sequential 1D-*Vs* profiles.

Drilling and seismic-method comparisons have confirmed the accuracy of the MASW approach and its sensitivity to changes in *Vs* (Xia et al., 1999). Surface-wave investigations have included: depth to bedrock (Casto et al., 2009; Miller et al., 1999a), comparison with refraction microtremor analysis (Anderson et al., 2007; Richwalski et al., 2007; Stephenson et al., 2005), hydrophone acquisition (Kaufmann et al., 2005), pavement characterization (Ryden et al., 2004), mapping of complex dipping structures (Xu and Butt, 2006), stratigraphic analysis (Watabe and Sassa, 2008), and time-lapse levee investigations (Ivanov et al., 2005b; Ivanov et al., 2006a). Hazard evaluations of anthropological voids and natural sinkholes have used *Vs* analysis to delineate such structures through their anomalous signatures (Billington et al., 2006; Miller et al., 2010a; Xia et al., 2007b). Furthermore, the relation between *Vs* and shear modulus (μ) may be exploited to assess the sensitivity of a site to ground motion (Anbazhagan and Sitharam, 2008; Hunter et al., 2010; Parolai et al., 2006; Yilmaz et al., 2006). Others have studied dispersion-curve imaging (Dal Moro et al., 2003; Duputel et al., 2010; Luo et al., 2008). Sensitivity testing has

included method resolution (Boiero and Socco, 2010; O'Neill et al., 2008; Xia et al., 2005; Xia et al., 2007a) and repeatability (Beaty and Schmitt, 2003).

Care must be taken to limit inaccurate inversion of an under- or over-parameterized problem. The nonuniqueness inherent with the stratification of a layer model may restrict vertical 1D resolution if too coarse or create situations of inversion instability if too fine. In contrast to the number and thickness of layers, the overall depth to the halfspace is often a subjective calibration based on knowledge of a site and rules of thumb (depth conversion ratio). In light of this, multi-mode inversion (Luo et al., 2007; O'Neill and Matsuoka, 2005; Xia et al., 2003) and constrained inversion schemes (Renalier et al., 2010; Socco et al., 2009) act to limit inversion nonuniqueness and instability. Although some have worked to lessen model parameterization, caution must be taken with standard MASW techniques.

Additionally, both deterministic and stochastic inversion schemes depend upon 'perfect' imaging of a site's dispersion characteristics. Domain transformation, and the finite windowing of the x-t space, introduces possible dispersion misinterpretation due to spectral leakage (Lyon, 2009), inadequate sampling of low-frequency Rayleigh waves, higher-mode (HM) contamination, and insufficient resolution of dispersion characteristics (wavenumber and phase velocity). Adopting new methods of domain transformation may lessen these effects (Ivanov et al., 2010; Luo et al., 2008). In the end, only a strenuous examination of dispersion characteristics and site-dependent offset-selection effects can lead to proper dispersion interpretation.

The inversion and dispersion-imaging techniques of the relatively new method rely on several subjective processing decisions that may result in inaccurate *Vs* estimations. The use of *a priori* information from other geophysical methods or geologic and borehole studies are suggested to limit such ambiguities of classical MASW routines. In the same light, numerical modeling of

synthetic data may help reduce the uncertainty of dispersion-image interpretation, inversion instability, and model parameterization. Current research seeks incremental, modular improvements of the MASW technique. Assimilating these various singular adaptations is proposed to further the methodology of MASW by engendering a more constrained routine which provides higher resolution, higher confidence velocity models.

2. Dispersion Imaging

MASW uses the property of dispersion to image the near-surface. When compared to contemporary spectral analysis of surface waves (SASW) (Nazarian and Stokoe, 1984), more accurate phase-velocity information requires a multichannel approach (Park et al., 1999). Gathers are analyzed for Rayleigh-wave dispersion to solve the inverse problem of S-wave velocity. Interpretation of the dispersion image (overtone image) is imperative for proper inversion and accurate resulting *Vs* models. The resolution and quality of the overtone image (OT) is a function of the analysis used to extract velocity information. The purpose of this section is to discuss the procedure of several imaging methods, compare their capabilities, and discuss possible implications to ongoing research. The phase shift method developed, and currently used, at the Kansas Geological Survey (KGS), outperforms standard methods because of its versatility and resolution (Park et al., 1998; Dal Moro et al., 2003).

Dispersion is defined by Sheriff (2002) as "variation of velocity with frequency." Dispersive waves may include:

Guided or channel waves – Induced when a wave guide traps seismic energy

Lamb waves – High-stiffness contrast, trapped (guided) waves

Love waves – Free-surface excitation with horizontal shear motion (S_H)

Rayleigh waves – Free-surface excitation with retrograde elliptical motion (S_V)

Stoneley waves – Solid-Solid boundary excitation

Sholte waves – Solid-Liquid boundary excitation

This thesis discusses Rayleigh waves, which propagate as the interference of P- and S_V-waves along the free surface (Figure 5; Stein and Wysession, 2003; Xia, 2008; Xu et al., 2006). Postcritical S_V waves incident on the free surface (XY plane) give rise to critically refracted P-waves and phase-shifted reflected S_V waves. The simultaneous existence of these wave modes gives rise to the Rayleigh wave.

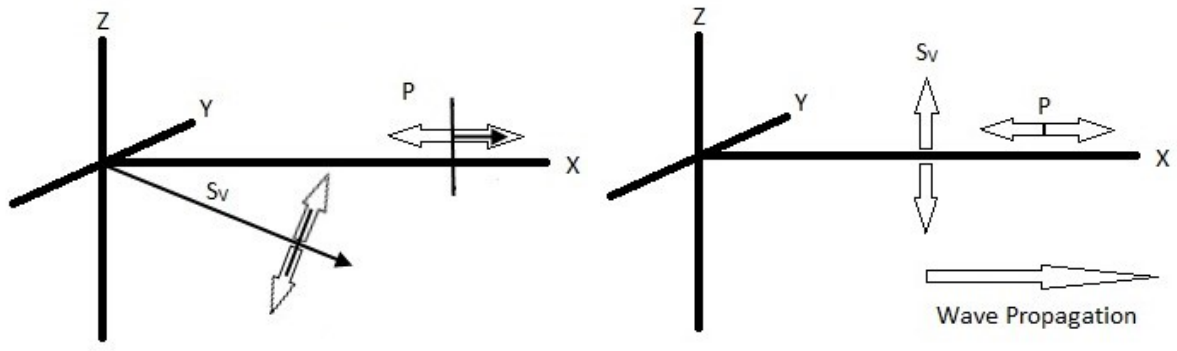

Figure 5: Left) Diagram of a phase-shifted Sv reflection and an evanescent critically refracted P-wave induced from an incident postcritical reflected Sv wave. Large arrows depict particle motion, small arrows and perpendicular lines give plane-wave propagation direction. Right) The interference of the evanescent P-wave and S_V-particle motion at the free surface produce Rayleigh waves.

Using the equations after Stein and Wysession (2003), the Rayleigh-wave motion for a Poisson solid halfspace may be modeled (Figure 6). As the waves are coupled to the air-earth boundary, investigation depth is a function of frequency (wavelength) and attenuation. At roughly one fifth of a wavelength, the motion becomes purely vertical. Below this, the motion converts to a prograde-elliptical motion as the attenuation vector changes sign.

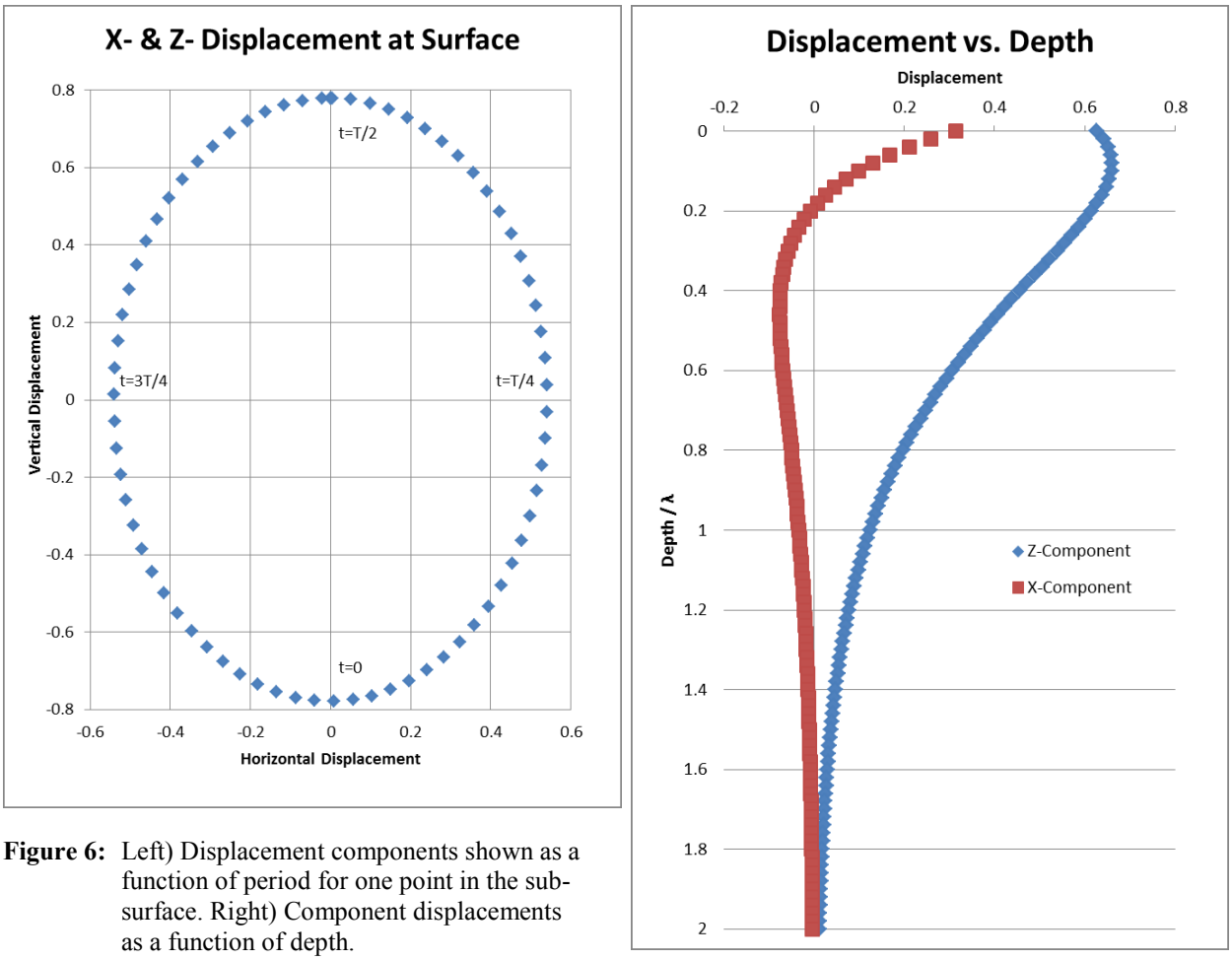

Figure 6: Left) Displacement components shown as a function of period for one point in the sub-surface. Right) Component displacements as a function of depth.

Assuming a media with distinct velocity layering, dispersion results as the various frequencies of Rayleigh waves travel within different velocity horizons of the subsurface. As seen on shot gathers, the variable phase velocities of individual wavelengths result in surface-wave dispersion (Figure **7**). Through domain transforms, phase velocity may be extracted from standard shot gathers to produce the overtone image (Figure 8). Curvilinear maxima are most usually studied for the apparent fundamental-mode Rayleigh-wave curve (Socco et al., 2010). As discussed in later chapters, the compressional-wave velocity (*Vp*) component of the Rayleigh wave has a relatively small effect on the Rayleigh-wave phase velocity when compared to the *Vs*

component. This dominant character allows us to obtain a *Vs* model, through deterministic inversion, given a picked dispersion curve.

The proper identification of the fundamental modal-curve, and its separation from harmonic higher modes, is of particular interest. Resolution of the overtone image is a result of both transformation technique and survey parameterization (Park et al., 1998). As a dispersion curve is generated over a selected range of geophones, the dispersion curve can be seen as a laterally averaged measure of the velocity structure. Horizontal model-resolution is therefore a function of the spread length, with longer lengths resulting in increased averaging. While longer spreads may limit final lateral resolution, research shows that higher overtone resolution and the separation of harmonic modes are achieved with longer spreads (Ivanov et al., 2008; Xu et al., 2006; Dal Moro et al., 2003). Some sites may require a reduction in *Vs*-model resolution to guarantee an adequate quality threshold and overall clarity of the dispersion curve/image. In the presence of HM excitation, the trade-off between overtone image and model resolution is critical. Considering this, optimal dispersion curve generation will give the greatest resolution over the largest range of offset, survey parameters, and geologic setting. Appendix II reiterates the variables and equations listed in the following sections.

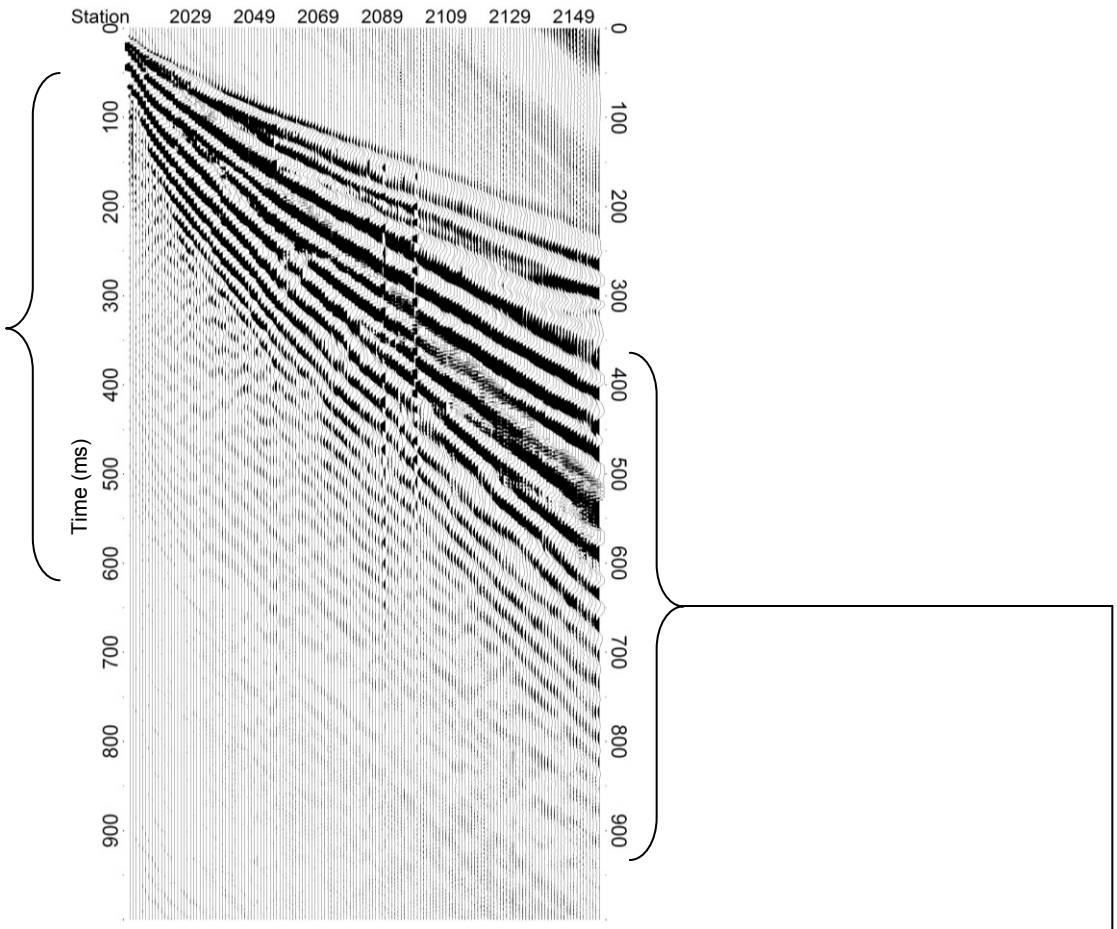

Figure 7: Reference shot gather from the Yuma site with Rayleigh-wave dispersion highlighted.

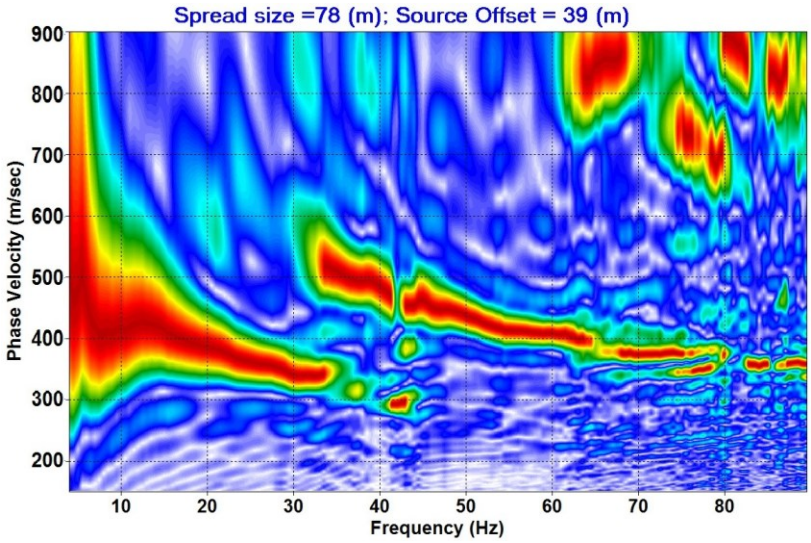

Figure 8: Reference dispersion curve from the Yuma site.

2.1. Imaging Methods

2.1.1. f-k

The *f*-k method uses Fourier analysis to apply a 2D transformation from the *x*-*t* to the k_x-ω domain (eq. 1-2).

$$\text{Input Data Function } F(x,t)$$

$$F(x,\omega) = \int P(x,t)e^{-i\omega t}dt \tag{1}$$

$$F(k_x,\omega) = \int P(\omega,x)e^{ik_x x}dx \tag{2}$$

The first step is to apply the Fourier transform in time (t) to result in angular frequency (ω) vs. offset (x). The next step involves a Fourier transform in the spatial domain (offset), which results in spatial wavenumber (k_x). The phase velocity is then interpreted from the relation of frequency divided by wavenumber. This method is clear and straightforward; however, it lacks resolution of phase velocity, and, as such, has limitations in distinguishing higher modes. In general, the method is more suited to SASW and passive methods that deal with non-linear arrays that often require more processing than common MASW surveys (Socco et al., 2010). Other issues of this method are the dense spatial sampling required to prevent spatial aliasing and the need for long receiver arrays for proper wavenumber resolution (Foti et al., 2002).

2.1.2. p-τ

McMechan and Yedlin (1981) first proposed the slant-stack, or slowness-tau (p-τ) method (eq. 3-5).

$$\text{Linear Moveout: } \tau = t - p_{\mathrm{n}}x\,, \qquad \text{for } p_{\mathrm{n}} = [p_1, p_2, \dots, p_{\mathrm{m}}] \tag{3}$$

$$\text{Slant Stack: } S(p_{\mathrm{n}}\,, \tau) = \int F(x, t = \tau + p_{\mathrm{n}}x)\, dx \tag{4}$$

$$S(p_{\mathrm{n}}\,, \omega) = \int S(p_{\mathrm{n}}\,, \tau) e^{\mathrm{i}\omega\tau} \mathrm{d}\tau \tag{5}$$

Here, data are first coordinately transformed with a linear move-out ($t \rightarrow \tau$), whose application transforms the time axis (t) by a specific slowness (p_{n}), the inverse of velocity (v) (eq. 3). Amplitudes are then stacked across offset (x) (eq. 4); the process is repeated for a range of phase velocities that are concurrent with the site-specific Rayleigh-wave dispersion. In relation to the p-τ transform, reflection hyperbolas map onto ellipses, and linear events map onto points. In a layered earth, the dispersion of surface waves will result in a series of points in the p-τ domain. Transformed to the frequency domain (eq. 5), the moving maxima along frequency may be interpreted as the dispersion curve (McMechan and Yedlin, 1981). The sensitivity of this method is largely a function of the step-size used for ω, p, and x (Park et al., 1999). Where p, f, and their step value are arbitrary and set by the user, the geophone spacing is a survey parameter that may affect the quality of the dispersion curve. Figure 9 shows a graphical representation of the transform.

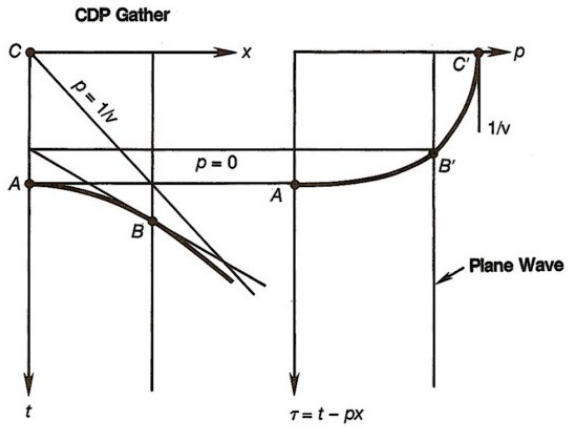

Figure 9: Graphical representation of the p-τ method, with the data transformed from the offset-time domain to the slowness vs. time domain (Yilmaz, 2001)

2.1.3. Phase Shift

The phase shift method was pioneered at the KGS, mainly through the work of Choon B. Park. The technique can be thought of as a particular implementation of the p-τ method (eq. 6-9) (Park et al., 1998).

$$U(x,\omega) = \int F(x,t)e^{\mathrm{i}\omega t}\mathrm{d}t \tag{6}$$

$$U(x,\omega) = P(x,\omega)A(x,\omega) \tag{7}$$

$$U(x,\omega) = e^{-\mathrm{i}k_{\mathrm{x}}x}A(x,\omega), \text{where } k_{\mathrm{x}} = \omega/c_{\mathrm{R}} \tag{8}$$

$$V(\omega,\phi) = \int e^{\mathrm{i}\phi x}\left[\frac{U(x,\omega)}{|U(x,\omega)|}\right]\mathrm{d}x \tag{9}$$

$$= \int e^{\mathrm{i}(k_{\mathrm{x}}-\phi)x}\left[\frac{A(x,\omega)}{|A(x,\omega)|}\right]\mathrm{d}x$$

The (x-t) data are first transformed to the frequency domain (eq. 6). At this point, the wave field may be thought of as a two-spectrum system of amplitude and phase (eq. 7). This leads to equation 8, where the phase spectrum is expressed as a function of Rayleigh-wave phase velocity (c_{R}), or the associated wavenumber (k_{x}). Next, an operation reminiscent of a slant-stack is applied across offset normalized amplitudes, at a particular frequency, and assuming a particular Rayleigh-wave velocity that corresponds to a phase-shift across offset (ϕ) (eq. 9). The dispersion

curve is a result of the phase-correction values measured across moving, maximum-stacked amplitudes of $V(\omega, \phi)$, which are transformed to $I(\omega, c_R)$ through the relation of $c_R = \omega/\phi$. Due to the separation of frequencies at the initial transformation, this method is considered more accurate than the standard p-τ method, which loses resolution along the frequency axis.

Where the p-τ method may suffer from loss of resolution with HM interference or superpositioning, the phase method offers "perfect resolution" (Park et al., 1998). As Park et al. (1998) mentions, the algorithm still retains the p-τ limitation of phase velocity resolution, but has proven effective across a multitude of applications. Additionally, the normalization factor may help to reduce spectral leakage and HM interference.

2.2. Implications with Application

Of those studied, the phase-shift method gives the highest resolution dispersion-curve images. The *f*-k method lacks resolution and the ability to accurately separate harmonic modes; also, it is not dependable when surveys are under-sampled in time or space. While the p-τ method makes improvements over *f*-k analysis, it may lack resolution in phase velocity at specific frequencies. Dal Moro et al. (2003) studied the effect of a short spread length on each method (Figure 10), and demonstrated the effects of normalization and bandpass filtering on the overtone image (Figure 11). A short spread resulted in spatial aliasing of the *f*-k method, while filtering and normalization had a lesser effect on the phase shift method as compared to the conventional p-τ method. Dal Moro et al. (2003) concluded that the phase shift method proved most insensitive to survey design and processing. As the most robust across broad survey configurations and processing routines, the phase-shift method is the first choice in dispersion analysis. It should be noted that other techniques exist that were not studied here (e.g., SPAC)

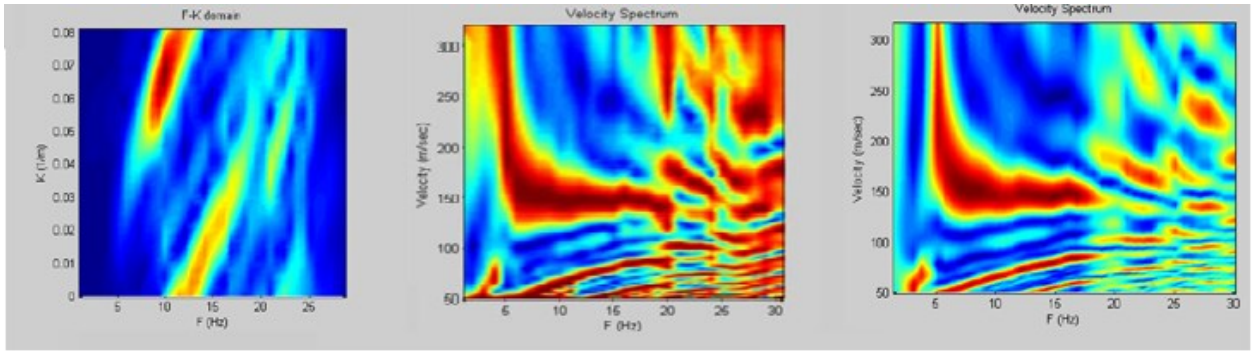

Figure 10: A four-trace transform using (left to right): f-k method, p- τ method, and phase-shift method (after Dal Moro et al., 2003).

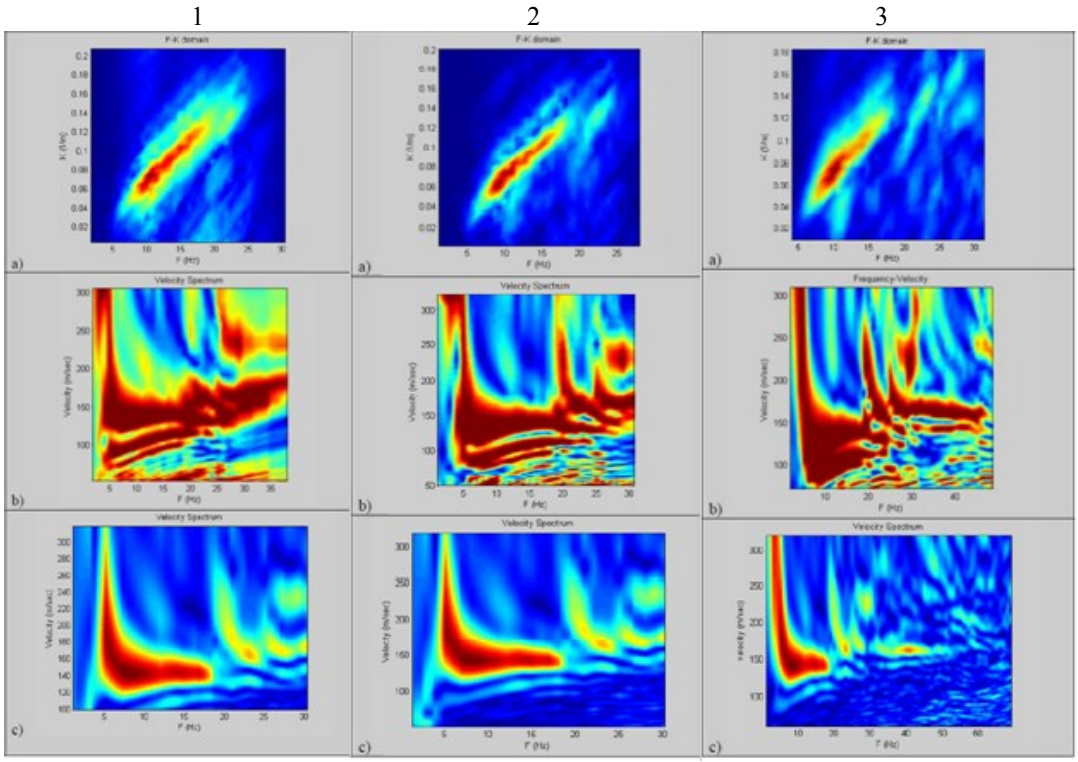

Figure 11: Results after Dal Moro et al. (2003) with a sequence of dispersion curves calculated from 24-geophone gathers with the a) f-k method, b) p-τ method, and c) phase shift method. Column 1 is with a (0-2-20-30) bandpass filter, column 2 is the same as column 1 with a normalization factor, and column 3 is with a (0-3-50-70) bandpass filter.

3. Inversion Theory

Sheriff (2002) describes inversion as "[d]eriving from field data a model to describe the subsurface that is consistent with the data." The previous section described how Fourier analysis was used to assess a site's dispersion characteristics and develop a relationship between frequency and phase velocity. Forward modeling is then implemented, which can be thought of as the opposite of inversion, to transform a layered-earth velocity model (*Vs*, *Vp*, density (ρ), and thickness (h)) into a dispersion curve. This forward problem is the basis for the inversion and ties the model parameters, specifically *Vs*, to the phase-velocity data through wave theory. Inverse methods minimize the difference between this earth-model generated curve and that of the experimental data through an update of the model-space parameters (*Vs*). This process is looped to iteratively minimize the data mismatch until an acceptable model converges to site characteristics. The following sections discuss, in more detail, the methods of the MASW inversion scheme. As a clerical note, matrices are indicated in bold and variables in italic.

3.1. Forward Modeling

The equations of motion for a Rayleigh wave have long been known. Texts such as Ewing, Jardetzky, and Press (1957) have fundamental equations, and their derivations, for the motion of the Rayleigh wave. The advancement of computers led to the development of software code that allowed for the modeling of such wave processes. Early work by Thomson (1950) and Haskell (1953) centered on the formulation of matrix expressions of the elastodynamic equations and their implementation as code, known as the 'transfer matrix method' (propagator matrix). The transfer matrix method is based on the assumption of a layered earth model. Limiting factors, such as numerical overflow and precision limits hampered the initial implementation of Raleigh-wave motion numerical modeling. Today, the transfer matrix numerical solutions to wave-equation

motion are widely utilized.

Schwab and Knopoff (1972) developed a particular code that reduced the aforementioned computational problems and resulted in faster forward-calculation of the Rayleigh-wave dispersion curve. Particularly, they implemented precision-loss normalization and a layer-reduction scheme into their formulation of the wave equations. This code is used for the forward modeling of surface-wave dispersion curves in the SurfSeis program. The objective function, in its linear, implicit form is:

$$F(f_{\mathrm{j}}, c_{\mathrm{Rj}}, \mathbf{v_s}, \mathbf{v_p}, \boldsymbol{\rho}, \mathbf{h}) = 0 \;\; ; \text{ where } (\mathrm{j} = 1, 2, \ldots, \mathrm{m}) \tag{10}$$

where f_{j} is the frequency; c_{Rj} is the Rayleigh-wave phase velocity at frequency f_{j} ; $\mathbf{v_s} = (v_{\mathrm{s1}}, v_{\mathrm{s2}}, \ldots, v_{\mathrm{sn}})^T$ is the *S*-wave velocity vector, where v_{si} is the shear-wave velocity of the *i*th layer and *n* is the number of layers; $\mathbf{v_p} = (v_{\mathrm{p1}}, v_{\mathrm{p2}}, \ldots, v_{\mathrm{pn}})^T$ is the compressional P-wave velocity vector, with $\mathrm{v_{pi}}$ being the P-wave velocity of the *i*th layer; $\boldsymbol{\rho} = (\rho_1, \rho_2, \ldots, \rho_{\mathrm{n}})^T$ is the density vector, with ρ_{i} being the density of the *i*th layer; and $\mathbf{h} = (h_1, h_2, \ldots, h_{\mathrm{n-1}})^{\mathrm{T}}$ is the thickness vector, with h_{i} being the thickness of the *i*th layer (Xia et al. 1999). If given an input **h**, $\mathbf{v_s}$, $\mathbf{v_p}$, and $\boldsymbol{\rho}$ model, along with a range of frequencies (f_{j}), one can calculate the Rayleigh-wave phase velocities (c_{Rj}) from the roots of equation 10. The roots of equation 10 are found using the bisection method to find the phase velocities c_{Rj} (Press et al., 1992). This process involves bounding the equation about zero and continuously halving the interval distance, using subsequent end members for further calculation, until a certain amenable threshold is reached. Repeating this search for various frequencies, results in a set of dispersion points ($f_{\mathrm{j}}, c_{\mathrm{Rj}}$) that together may be compared to the experimental curve for minimization.

3.2. Least-Squares Approach

Xia et al. (1999) wrote the code that SurfSeis uses to invert dispersion curves for *Vs*; his work forms much of the following computational explanation (Xia et al., 2008). The inversion follows the basic theory of a least-squares approach. The method applies a weighted, damped least-squares method to reduce the error between the calculated forward-model and the observed data. In particular, the Levenberg-Marquardt (LM) method is used to hamper non-singularity and to ensure convergence of the model. The technique also applies singular value decomposition (SVD) in order to limit computing costs and allow fluid variability of the damping factor with convergence.

The non-linear problem is linearized through Taylor series expansion, by looking at small perturbations of the system, and setting up a finite-difference numerical calculation (Lourakis, 2005; Xia et al., 1999). This leads to the application of equation 11:

$$\mathbf{J}\Delta\boldsymbol{x} = \Delta\mathbf{b} \tag{11}$$

where $\Delta\mathbf{b} = \mathbf{b} - \boldsymbol{c}_{\mathrm{Rj}}(\boldsymbol{x_0})$ and is the difference between the observed data ($\mathbf{b}$) and the forward model response ($\boldsymbol{c}_R$) to the initial *S*-wave velocity estimates ($\mathbf{x_0}$), which is minimized; $\Delta\boldsymbol{x}$ is the stepwise adjustment of the initial estimation; $\mathbf{J}$ is the Jacobian matrix. The elements of the Jacobian matrix are the first-order partial derivatives of $\boldsymbol{c}_{\mathrm{R}}$ with respect to S-wave velocities ($\mathbf{v}_{\mathrm{si}}$) (eq. 12).

$$\mathbf{J_S} = -\frac{\partial F/\partial v_{\mathrm{si}}}{\partial F/\partial c_{\mathrm{Rj}}}\bigg|_{f=f_{\mathrm{j}}} \tag{12}$$

The Jacobian is calculated using Ridders' method of polynomial extrapolation and finite-difference evaluation employing Neville's algorithm (Press et al., 1992; Xia et al., 1999). Neville's algorithm extrapolates numerical finite-difference derivatives and, at each step size, a higher-order extrapolation is checked against those of lower-order for optimization (Press et al.,

1992).

For a damped, weighted least-squares inversion, the objective function becomes:

$$\Psi = \|\mathbf{J}\Delta\mathbf{x} - \Delta\mathbf{b}\|_2 \, \mathbf{W}\|\mathbf{J}\Delta\mathbf{x} - \Delta\mathbf{b}\|_2 + \alpha\|\Delta\mathbf{x}\|_2^2 \quad (13)$$

where $\| \quad \|_2$ is the L_2-norm length of a vector, α is the damping factor, and $\mathbf{W}$ is a weighting matrix. The weighting matrix is a function of changes in Rayleigh-wave phase velocities with respect to frequency change, as denoted by the Jacobian; this is a representation of the resolution of such frequencies and therefore the basis for such weighting (Xia et al., 1999). Transforming the weighting matrix to:

$$\mathbf{W} = \mathbf{L}^T\mathbf{L} \quad (14)$$

where $\mathbf{L}$ is a diagonal matrix, the objective function may be represented in terms of the LM method as:

$$\Delta\boldsymbol{x} = (\mathbf{A}^T\mathbf{A} + \alpha\mathbf{I})^{-1}\mathbf{A}^T\mathbf{d} \quad (15)$$

where $\mathbf{A} = \mathbf{LJ}$, $\mathbf{d} = \mathbf{Lb}$, and $\mathbf{I}$ is the identity matrix (Xia et al., 1999; Zhdanov, 2002). Using singular value decomposition for the model space $\mathbf{A}$, the objective function may be minimized while adjusting the damping factor without recalculating the inverse matrix in equation 15:

$$\Delta\boldsymbol{x} = [\mathbf{V}(\boldsymbol{\Lambda}^2 + \alpha\mathbf{I})^{-1}\boldsymbol{\Lambda}\mathbf{U}^{\boldsymbol{T}}]\mathbf{d} \quad \text{or} \quad \Delta\mathbf{x} = [\mathrm{G}]^{-1}\mathbf{d} \quad (16)$$

where matrix $\mathbf{A}$ is decomposed as $\mathbf{A} = \mathbf{U}\boldsymbol{\Lambda}\mathbf{V}^{\boldsymbol{T}}$; where $\mathbf{V} = [v_1, v_2, \ldots, v_i]$ is composed of the eigenvectors that span $\mathbf{A}^{\boldsymbol{T}}\mathbf{A}$, where $\mathbf{U} = [u_1, u_2, \ldots, u_i]$ is the matrix of eigenvectors that span $\mathbf{A}\mathbf{A}^{\boldsymbol{T}}$, and where $\boldsymbol{\Lambda}$ is the diagonal monotonically increasing matrix of the square roots of the eigenvalues of $\mathbf{A}^{\boldsymbol{T}}\mathbf{A}$ and $\mathbf{A}\mathbf{A}^{\boldsymbol{T}}$ (Gavin, 2011; Pujol, 2007).

The LM method allows for a combination of steepest decent and Gaussian-Newton convergence by changing the damping factor from large ($\alpha\rightarrow\infty$) to small ($\alpha\rightarrow 0$) values, respectively. The convergence starts with high values of α using steepest decent to constrain movement, and then reduces α to converge quickly upon a solution in a Gaussian-Newton sense.

This implementation minimizes the objective function while remaining robust.

3.3. Global or Stochastic Approach

Other inversion approaches use stochastic inversion to conduct global searches of the solution space (Socco and Boiero, 2008; Ryden and Park, 2006; Wathelet et al., 2004). These schemes are generally used to reduce the risk associated with local minima and the non-uniqueness problem of the non-linear Rayleigh-wave problem. The computational cost and the subjective control on the search range, step sequence, regularization, and misfit criteria make them impractical for many applications and limit their robustness. These approaches may also lack any greater rationalization of the layer-model when using static layering and/or underparameterizing the problem. Socco and Boiero (2008) developed an optimized Monte Carlo scheme that was capable of limiting the effects of inversion controls with the ability to search outside the original search space (velocity) and allowing varying layer thickness. When using global-search methods, choosing a proper layer-model is compounded with the exponential rise in computational costs seen with increasing stratification. Stochastic inversion may better define the minimum(s) within the search range, but they do not intrinsically protect against global minimization of an incorrect or underparameterized model space.

In preliminary investigations, the ability to quickly test and compare differing parameter-sets, particularly the number of layers, across an entire survey area is essential. Global-search methods are frequently commended for their production of multiple models that converge to site characteristics. The multiplicity is seen as a greater sampling and more complete mapping of the solution space. The issue with such reasoning is when, in the end, a singular model must be decided upon. If such a sample formulates the final interpretation, few applications allow such variance outside of error estimation. Furthermore, relying only on error minimization may

lead to solution variability unrelated to site characteristics. The decoupling of parameterization from fitness estimations (whether quantitative or qualitative) makes relative noise thresholds, uncertainty, and processing methods more critical. As the solution complexity and variance increases within global searches, some metric outside of minimizing RMS error is needed.

3.4. Fundamental vs. Multi-Mode Complexity

The standard approach of surface wave methods is to solve the inverse problem through the minimization of the fundamental-mode curve (Socco et al., 2010; Xia et al., 1999). The forward-model waveform equations of motion are solved specifically for the fundamental-mode Rayleigh wave. Research later proved the usefulness of including HM information during the inversion (Luo et al., 2007; Maraschini et al., 2010; Xia et al., 2003). Higher-modes were shown to increase the depth of investigation and the model resolution of the inverse problem, while stabilizing the inversion by limiting the solution space. This improvement comes at the cost of a more-difficult interpretation.

Authors have shown that fundamental-mode inversion may be imperfect due to mode superposition and HM contamination. The effects of higher modes on dispersion characteristics, particularly the idea of an apparent curve, must be considered (O'Neill and Matsuoka, 2005; Tokimatsu et al., 1992). Due to the sampling of the Rayleigh-wave, which is a function of both acquisition parameters and dispersion imaging, individual modes may be masked, hidden, or skewed. This can create an apparent curve that may jump from mode to mode along the frequency axis rather than following the true fundamental-mode trend. This brings into question not only the phase-velocity picks, but also their mode assignment. However, muting in the x-t domain has been shown to reduce HM interference at high frequencies (Ivanov et al., 2005a). Moreover, some methods implicitly solve for an apparent curve which negates the need for mode assignment (Lai

and Rix, 1998). This strategy, however, only guards against misinterpreted modes and provides no constraint for the inherent effects of the transformation. An ill-posed acquisition scheme could control the dispersion character and result in inaccurate results.

To confidently incorporate HM data into the inversion scheme, the processor must accurately identify mode-number/HM superposition and empirically test the effects of acquisition on dispersion-curve characteristics. An initial processing scheme, suggested by Ivanov et al. (2008), is to vary the source offset and the spread length to gain an understanding of the variance of the phase-velocity curve found using different parameter sets. General practice assumes that a long initial spread gives the highest-resolution, most-accurate curve (especially at low frequencies). Departures from this spread length are made to increase the lateral resolution of the survey, but must be assessed for inaccurate sampling of the Rayleigh-wave. Also, as the method averages the wave field over the entire spread length, there is no inherent way to separate local heterogeneity from sampling effects.

3.5. Model Space and Parameterization

Xia et al. (1999) analyzed the Jacobian matrix and the effect of $\mathbf{v_s}$, $\mathbf{h}$, $\boldsymbol{\rho}$, and $\mathbf{v_p}$ on the phase velocity solution for a given synthetic model. They found that the ratio of percentage change in phase velocity to percentage change for each variable to be 1.56, 0.64, 0.4, and 0.13, respectively. This comparison shows empirical evidence of the sensitivity of Rayleigh-wave phase velocity to *Vs* structure. It also restates the importance of the layer model, specifically layer thickness (**h**), to *Vs* inversion. Considered small, and within known values for most sites, the divergences seen with *Vp* and density variation were deemed minimal. For sites where such values are not known to 25%, as suggested in Xia et al. (1999), such generalizations may not be acceptable. Ivanov et al. (2009) demonstrated that *Vs* inversion may not always be insensitive to

density; the research revealed that the density gradient, rather than a bulk shift, is important to achieve accurate results for some sites. Others have studied the significance of the initial layer model (layer: number, velocity, thickness; and depth to halfspace) on inversion results (Casto et al., 2009; Renalier et al., 2010; Wathelet et al., 2004). For all considered, and whenever available, *a priori* information should be used to constrain the inversion and improve the method's reliability.

The 1D-inversion scheme results in interval velocities that correspond to a layer model for each dispersion-curve midpoint. This layer model may be entirely generalized to best fit the initial dispersion properties of a site, or be more constrained through evaluation of *a priori* information. The initial *Vs* layer model may be guided by the asymptotic values of the apparent fundamental dispersion curve, which are approximately 90% of the *Vs* of the first and halfspace layers. Serving as an initial smooth case, a less parameterized, fewer-layer (<10) model may converge to the experimental dispersion curve, while limiting the instability of the inversion. Departures from this initial model may be affected by borehole data, or other geophysical methods, that dictate a particular stratigraphic sequence. With MASW, the lack of high-frequency content may limit the confidence of the uppermost velocity interval(s). Similarly, the further stratification of basal layers may destabilize the inversion as deeper structures are sampled by longer wavelengths which smear the velocity field. The adoption of a more parameterized layer model, especially within regions that have limited or no dispersion-curve data may result in a profile not representative of the true *Vs* structure.

A proper balance between model smoothness, inversion stability, and vertical resolution is not always intuitive. To limit such ambiguity, the incorporation of refraction tomography is suggested as a means to constrain the layer model of MASW. This allows a more discretized

model whose layers may not have direct frequency to depth constraint using the general half-wavelength association of the dispersion curve to depth (Song et al., 1989), yet are upheld by tomographic inversion results.

3.5.1. Refraction Tomography and Joint Analysis

The inverse refraction traveltime problem (IRTP) poses several dilemmas due to nonuniqueness. Ivanov et al. (2006b) discussed the continuous multi-dimensional valley that defines the topology of the IRTP solution space. The occurrence of local minima and hidden/low-velocity layers make the IRTP difficult to properly invert, and leads to an infinite number of possible solutions that reasonably fit the traveltime data (Ackermann et al., 1986; Healy, 1963). The parameterization of the geologic model, from which the inverse problem initially precedes, is imperative as it will drive the convergence of a deterministic inversion scheme (Ivanov et al., 2006b; Palmer, 2010). Ivanov et al. (2006b) suggested the use of a reference model, derived from MASW, to properly constrain the convergence of *Vp*-refraction tomography (i.e., the joint analysis of refractions with surface waves (JARS)). The inclusion of *a priori* information is needed to accurately account for IRTP nonuniqueness.

Authors have documented the benefit of incorporating refraction and surface-wave methods (SWM) data into parallel processing routines. The similar acquisition techniques of the two approaches produce dual-purpose and cost-effective surveys. Near-surface refraction studies have been combined with SWM to reach more stable and constrained *Vs* inversions. Dal Moro (2008) used a Multi-Objective Evolutionary Algorithm (MOEA) to jointly invert P-wave refraction and Rayleigh-wave dispersion curves with *a priori* fixed Poisson's ratios. Foti et al. (2003) used a constrained inversion scheme that used P-wave refraction results to parameterize the inverse *Vs* problem. Schuler (2008) used the method after Dal Moro to separately and jointly invert

Rayleigh and Love waves with P- and S-wave refractions. Piatti et al. (2012) discussed a least-squares joint inversion of P-wave first arrivals and Rayleigh-wave dispersion that reached greater accuracy for low-velocity layers (LVL) than Dal Moro for synthetic data. Joint inversions, although more statistically precise, necessitate rigorous computational development essential to constraining the added degrees of freedom. The regularization and subjective *a priori* information needed to properly formulate joint inversion schemes act as fundamental limitations on their robustness and ease of use.

Where several papers discuss constrained layer-model inversion, they often reduce near-surface stratigraphy to a linearly smooth or several-layer problem. This is often a function of the limitations of common refraction theory (e.g., increasing velocity with depth), stochastic inversion's computational costs, or a belief in the parsimony of Occam's razor. While this may adequately formulate many analysis functions, higher-resolution models are often needed for various applications (e.g., modeling). The degree of smoothing may be compounded when SWM seek to delineate increasingly deeper strata with the inclusion of passive data (Di Giulio et al., 2012; Louie, 2001). Increasing the depth to the half space, while keeping the layer parameterization constant, may result in an over-simplification of the ultra near surface.

Most applications interpolate many 1D-profiles into a 2D-model space. In contrast, many research groups, especially those using stochastic approaches, implicitly use a single 1D profile to confer their conclusions. Although this is a correct representation of the initial results, few real-world applications rely on 1D-estimations, but rather seek to expand a site's characterization to 2D. Socco et al. (2009) and then Bergamo et al. (2012) used a laterally constrained inversion that mitigates the decoupling of 2D-imaging with many 1D-profiles. Their inversion routine simultaneously solves a set of 1D dispersion curves, constraining 2D-lateral variation and

improving structural imaging. They also displayed results in a 2D-fashion using non-interpolated sets of 1D-profiles. When incorporating tomographic methods, which intrinsically use 2D-grids, a direct SWM comparison would benefit from the use of interpolated imaging.

4. Data Acquisition

The YPG JTTR site was developed to advance the research of current tunnel-detection methods. To provide adequate control on the experimental testing of seismic tunnel detection, a baseline survey was conducted before the emplacement of a tunnel at the site. Data acquisition was approached with the intent of diversification, giving the broadest possible data set for future comparison. A multitude of seismic source and receiver methodologies were used to garner a well-balanced dataset for comparison study (see Table 1). Different sources imparted varying amounts of energy with different frequency signatures and dominant wave-mode propagation. Several natural frequency geophones were used to optimize the sampling of certain wave modes (surfaces waves, reflection, diffraction, shear vs. compressional, etc.). The KGS also procured a geologic investigation through drilling and well-log analysis. Due to the dry and unconsolidated nature of the predominantly fine-grained substrate, sonic drilling methods were used along with an AquaLock sampler to optimize sample retrieval (Figure 12).

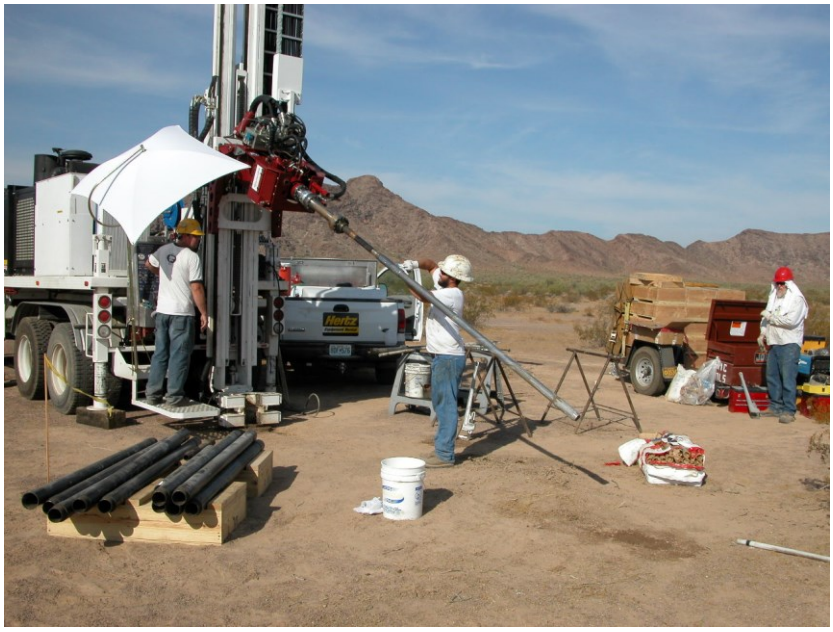

Figure 12: AquaLock geologic sampling system at work on the YPG site.

Although six lines were acquired, this thesis focuses on the two lines that had the full complement of source and receiver pairs, line 2 and line 3 (see Figure 1). A compressional-wave survey was conducted for MASW and refraction analysis, while several shear-wave surveys were acquired to garner a suite of *Vs* tomograms. The P-wave survey used a bungee-assisted drop-weight source (Figure 13) in conjunction with a fixed spread of 4.5 Hz vertical geophones spaced at 1.2 m, with three impacts at each station. The surveys used the Geometrics distributed Geode system, with line tap unit (LTU) implementation, and a custom KGS 'Gator' acquisition vehicle.

Figure 13: Photo of the weight drop used for P-wave refraction and MASW processing with the Trigo Peaks in the background.

For comparison, shear-wave surveys were designed with concurrent stations parallel and proximal to the MASW line. Horizontal 14 Hz geophones' direction of sensitivity were orientated perpendicular to the line with the source energy vector similarly orientated for S_H-wave recording; an in-line sensor and energy source were used for the S_V-wave mode (Figure 14). Hammer blows were struck three times in both directions every 24 stations using a shear block; vertically stacking both polarizations at each station sought to enhance S-wave energy and destructively counteract spurious P-wave energy (Helbig, 1986).

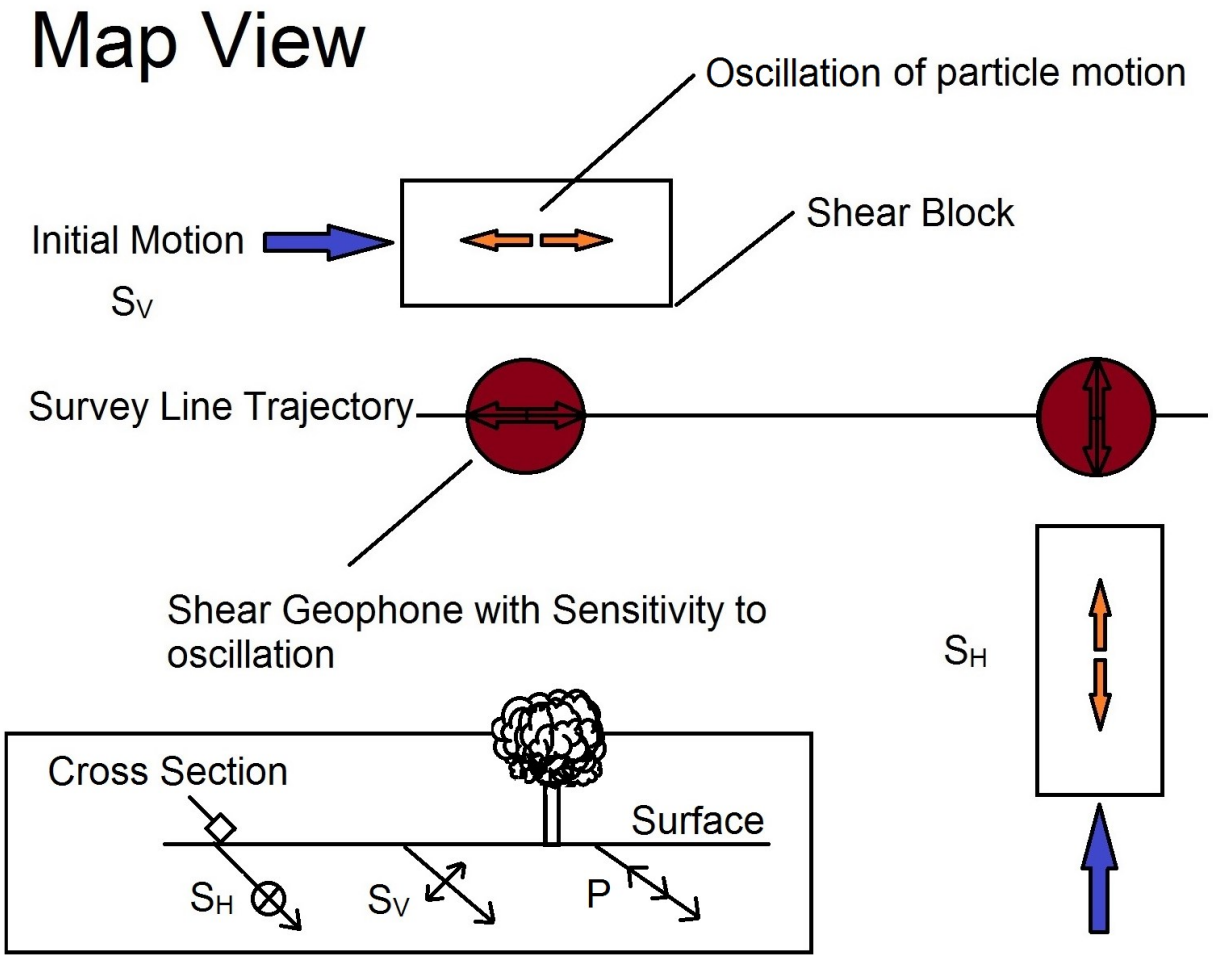

Figure 14: Shear-block setup for shear-wave tomography. The opposite direction of initial motion is not shown in the diagram. This is a simplification, both S_V and S_H sources will generate both shear-wave modes; however one is dominant.

Similarly, both S_H- and S_V-modes were recorded using an Industrial Vehicles International Minivib and a waffle plate; however, the density of source locations was increased to every 2 stations (Figure 15).

Figure 15: Picture of the IVI Minivib system used at YPG with three different orientations of the hydraulic mass: top left) S_H-; bottom left) S_V-; right) P-wave. Note the waffle plate used for shear generation in the lower left image and that the survey line is parallel to the long axis of the Minivib.

The vibroseis data were given least confidence in light of the common issues found in interpreting correlated first-arrivals. They are included to add multiplicity, strengthen the confidence of the shear-wave refraction results and, thereby, the MASW *Vs* models. S-wave hammer data and polarization comparisons helped to determine zero-phase first-arrival signatures.

Different modes of the seismic wavefield may illuminate the subsurface distinctly. As Rayleigh waves intrinsically rely on the interference of S_V- and P-waves, there is likely to be some disagreement between the MASW calculated shear wave velocity field and S_H–tomography velocity profiles. The degree to which anisotropy causes a disassociation of the *Vs* profiles is not directly measured here and was assumed to be negligible. The use of separate wave-mode propagation, along with two geophysical methods, should allow for independent assessment of site stratigraphy and velocity. As it relates to refining the MASW layer model, the velocity structure calculated from the refraction survey, rather than absolute values, is of primary interest.

5. Processing Methods

The various processes listed above: muting, offset selection, dispersion interpretation, inversion convergence and instability, refraction regularization, nonuniqueness and starting/ reference models, must be formed into one cohesive routine (Figure 16). Each round of processing conveys additional information which guides dispersion interpretation, layer-model refinement, and complimentary inversion of refraction and surface-wave methods.

The integration of MASW and refraction tomography incorporates layer-model refinement and inversion constraint (reference model), while producing multiplicity for *Vs*-model comparison. Where classical MASW assumes stratigraphic sequences based on regional geology or default layer schemes (Renalier et al., 2010; Xia et al., 1999), a constrained-parameterization approach uses independent measurements and data driven methods to constrain the layer-model inversion scheme. Refraction methods refine the reference velocity model (i.e. preliminary MASW) using non-Rayleigh wave seismic data (i.e., body waves) and an unrelated inversion scheme using the JARS methodology (Ivanov et al., 2006b). The resulting tomograms are interpreted for structural patterns to define a more-stratified parameterization of the Rayleigh-wave inversion, which compliments body-wave information (optimized constrained-parameterization MASW). Although there is some degree of dependence built into this system based on the use of reference models, independent data sources ultimately drive the convergence. The constrained-parameterization MASW routine progresses from a smooth, less-stratified solution to a constrained, higher-resolution *Vs* model, with refraction-tomography enhancement.

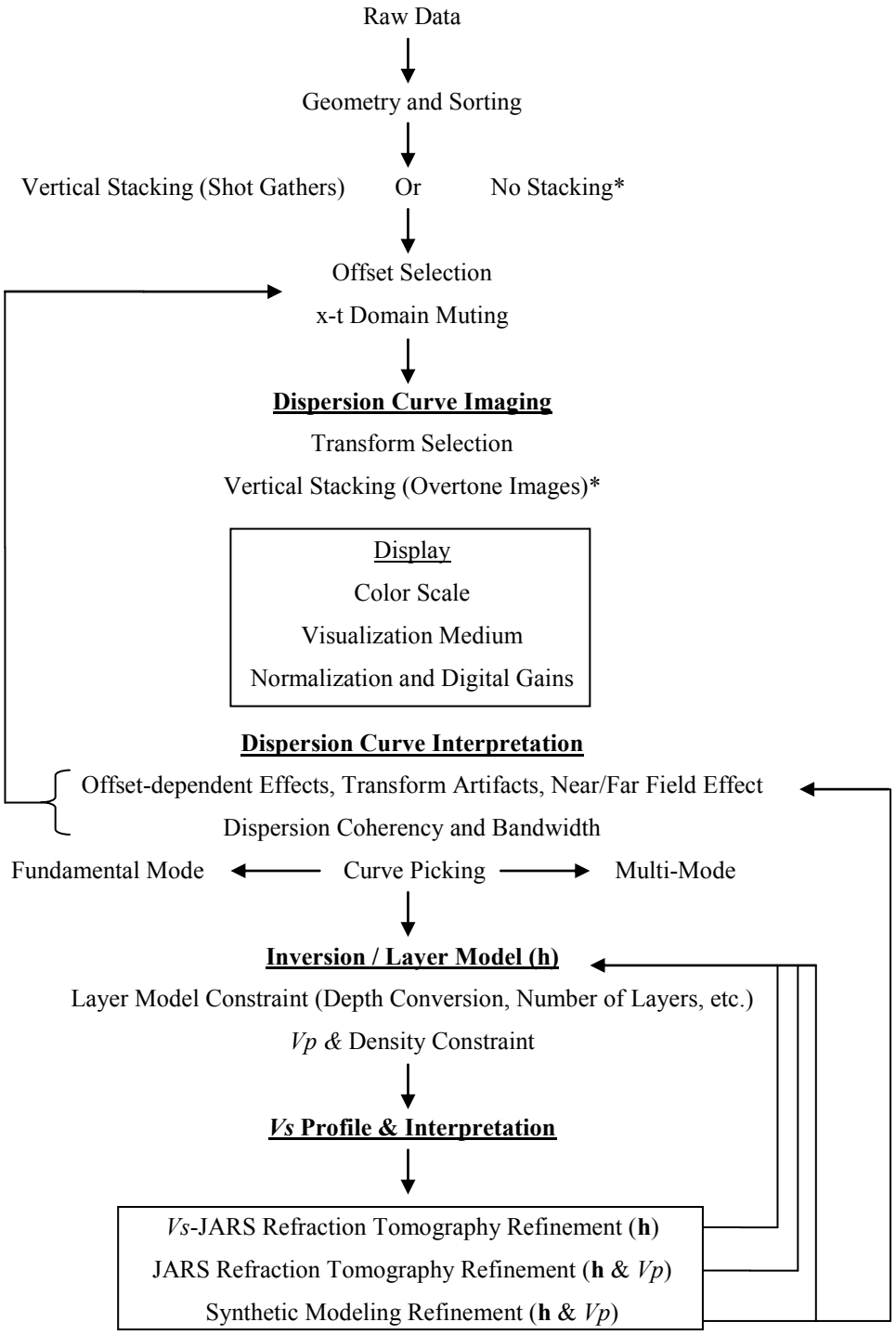

Figure 16: Generalized workflow for a constrained-parameterization MASW approach. Preliminary, first-run MASW allows a *Vs*-JARS/JARS application, the results of which may be used to update the layer model of the next generation MASW inversion. Later sections will discuss the addition of synthetic modeling for additional constraint on dispersion interpretation and layer-model refinement. Arrows depict updates with each additive constraint or information.

Proprietary software, developed at the KGS, was used for all processing steps. KGSSeisUtilities was used for initial geometry assignment, sorting, and first arrival picking. SurfSeis was used for overtone analysis, dispersion-curve picking, and *Vs* inversion. TomoSeis was used to invert the first-arrival data for velocity models. In house modeling software (FFDM) was used to produce synthetic seismograms and layer models (Zeng et al., 2011). Golden Software's® Surfer 8® and FFDMGUI were used as a gridding and display tool.

All dispersion curves were picked using a 47 inch LCD television (TV). The high-definition, high-resolution screens allowed an unparalleled picking environment (Figure 17). A simple comparison between manual picks made on the TV and a 19 inch laptop showed clear separation in point density, curve smoothness, and curvilinear trend. Quite simply, this is a product

Figure 17: Four 47 inch television setup used to pick dispersion curves.

of pixilation, or discretization, and an ability to increase point coverage and better define the dispersion curve over an arc length. Furthermore, the relative change from one pixel to another is reduced allowing for greater picking control and reduced sensitivity to minor adjustments in the curve. This scheme is somewhat irrational for many applications; however, the ability to more confidently follow trends across noise/amplitude irregularities, HM contamination, and within the phase-velocity resolution band is worth noting.

5.1. Preliminary MASW

The first round of testing resolves an initial, classical MASW study of the site's velocity structure using conservative layering and inversion parameters. These parameters typically include a smooth, relatively few layer (i.e., <10 layers; Xia et al., 1999) model to restrict inversion instability and improve convergence. Of great importance is the offset selection that controls the sampling of the Rayleigh wave and eventual overtone image. Dispersion interpretations are guided by analysis of offset-range sampling effects, x-t domain muting, and lateral changes in dispersion character. Moreover, curve analysis should dictate a relative depth of investigation and layer structure assuming a depth conversion ratio (Song et al., 1989). Additional information from well logs, etc. may be used to constrain the layer model if available; density values are used here. The preliminary, smooth MASW solution will guide further refinement using refraction methods.

5.1.1. Offset Selection

Initial processing focused on searching the geophone array for an appropriate parameter set (offset range in the x-t domain) that maximized lateral resolution, adequately sampled low frequencies, and reduced transformation effects in the frequency vs. phase velocity domain. A minimum offset of 1.2 m and a maximum offset of 78 m was determined to be optimal for the site.

This correlates to a 65 geophone spread with a 1.2 meter source offset. Common rules of thumb would dictate this source offset as detrimental to long wavelength, low frequency sampling of Rayleigh waves due to the near-field effect (Park et al., 1999; Xu et al., 2006). At close offsets, swept-frequency shot gathers would contain erratic linear inconsistencies at low frequencies that still behave non-linearly.

Rayleigh waves can only be treated as plane waves past a certain offset dependent on velocity structure and distance from the source (Richart et al., 1970). However, past studies at locations near the site have suggested the use of small source offsets are necessary for proper sampling of the Rayleigh wave (Ivanov et al., 2008). Through parameter analysis, the near-field disruption was deemed limited and marginal in comparison to the benefit of modal-separation, an expansion of bandwidth to higher frequencies, and overall dispersion coherency across frequency. The relatively longer length of the line (78m) acts to prevent the near-field effect through statistical averaging across offset. In comparison, longer offsets and shorter spreads lead to the degradation of the fundamental mode and HM interference (see Chapter 8). Without additional data control, there wasn't any definitive way to prove offset-specific changes in the overtone images (i.e., near/far-field effects, HM interference) were not related to velocity heterogeneity (lateral and vertical) rather than spatial sampling within the x-t domain.

5.1.2. Higher-Mode Contamination & Muting

Understanding HM contamination and using muting in the x-t domain to interpret its effects are an integral part of dispersion interpretation during offset selection and curve picking. In relation to section 3.4, higher-modes may be a valuable addition to Rayleigh-wave inversion (Luo et al., 2007; O'Neill and Matsuoka, 2005; Xia et al., 2003). However, in a different context, they may be equally adverse to the method. Of particular concern is HM contamination (Boore, 1969).

HM contamination encompasses all mode-phenomena that restrict the signature or strength of the fundamental-mode. This usually manifests as a strong-amplitude HM trend that starts above a certain 'cut-off frequency'. Classical texts use 'cut-off frequency' as the theoretical lowest observable frequency of an n^{th} mode. At these transitions, the fundamental-mode amplitude and/or coherency across frequency is denigrated as the higher-mode(s) is excited.

As the optimal spread was rolled down the line, there were changes in HM excitation, and strength (amplitude) of the fundamental mode (Figure 18). Although there is sporadic loss of amplitude, the dispersive signature is interpretable to 80 Hz on many overtone images. The fundamental-mode curve reaches an asymptotic value at approximately 200 m/s, which assuming a 90% correlation, estimates a first-layer velocity of 222 m/s.

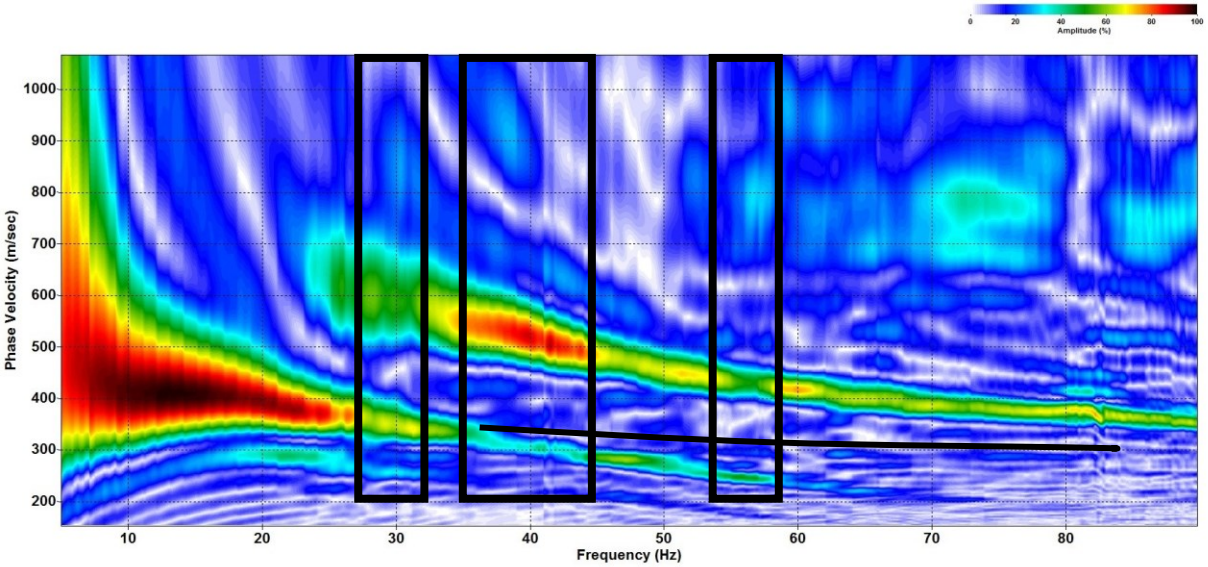

Figure 18: Dispersion curve showing good signal to 80 Hz with variable HM contamination above 30 Hz. Squares highlight several instances of the competing signal between the fundamental and the higher-mode. The bold black line highlights a questionable trajectory for the fundamental.

The dispersion-curve's high-frequency tails oscillated between two interpretable pathways across all lines (e.g., Figure 18). As many curves did not have high-amplitude high frequencies (>40 Hz), there was a need to assess whether the dispersion characteristics were related to site-wide geology or an anomalous lateral change in velocity.

In the presence of HM contamination, Ivanov et al. (2005a) suggested muting HM signatures on x-t domain gathers (Figure 19) to increase the signal strength, bandwidth, and interpretability of the fundamental mode (Figure 20). Linear muting increased the interpretable bandwidth of the fundamental-mode curve toward higher frequencies, but also adversely affected the low-frequency trend. Comparison between the muted and unmuted overtone image brings confidence that the previous record's curve properties (i.e., Figure 18) were not a result of a lateral change in velocity.

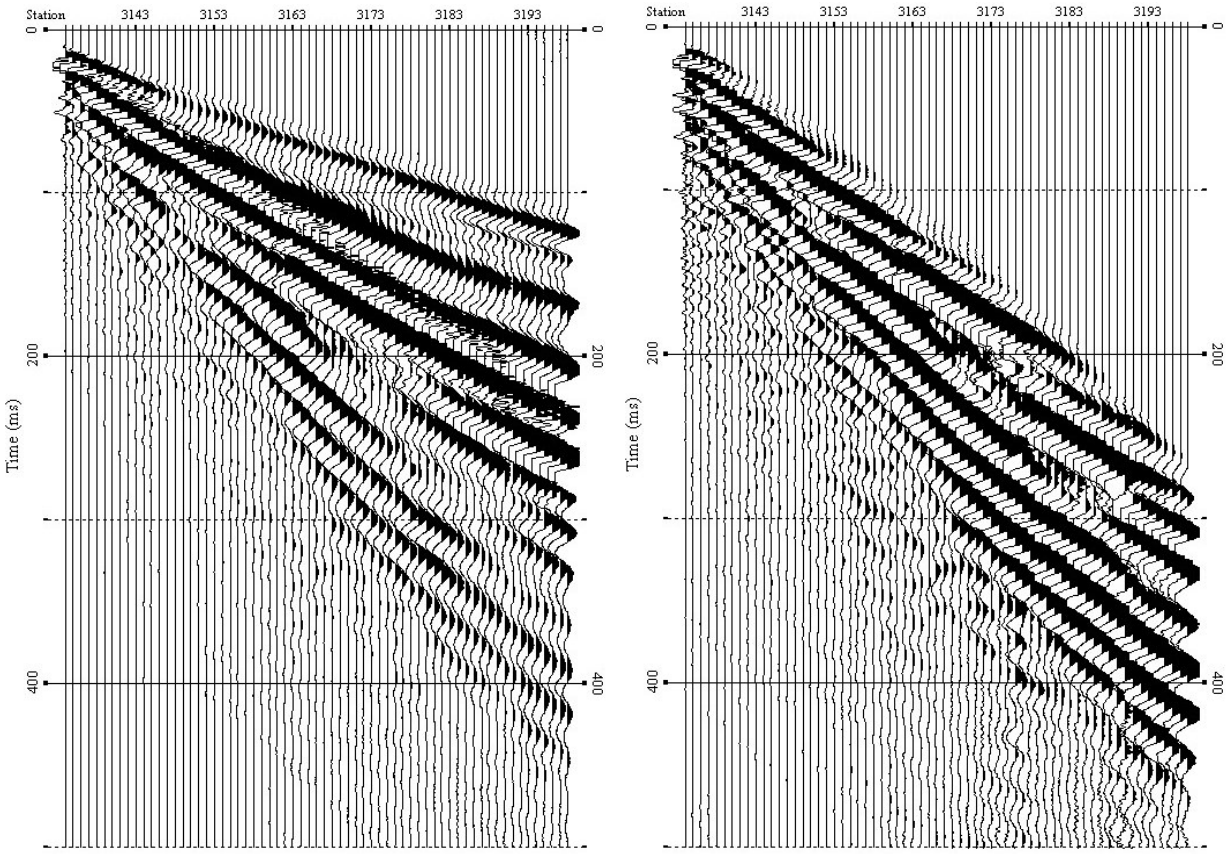

Figure 19: Left) Unmuted shot gather. Right) Muted shot gather.

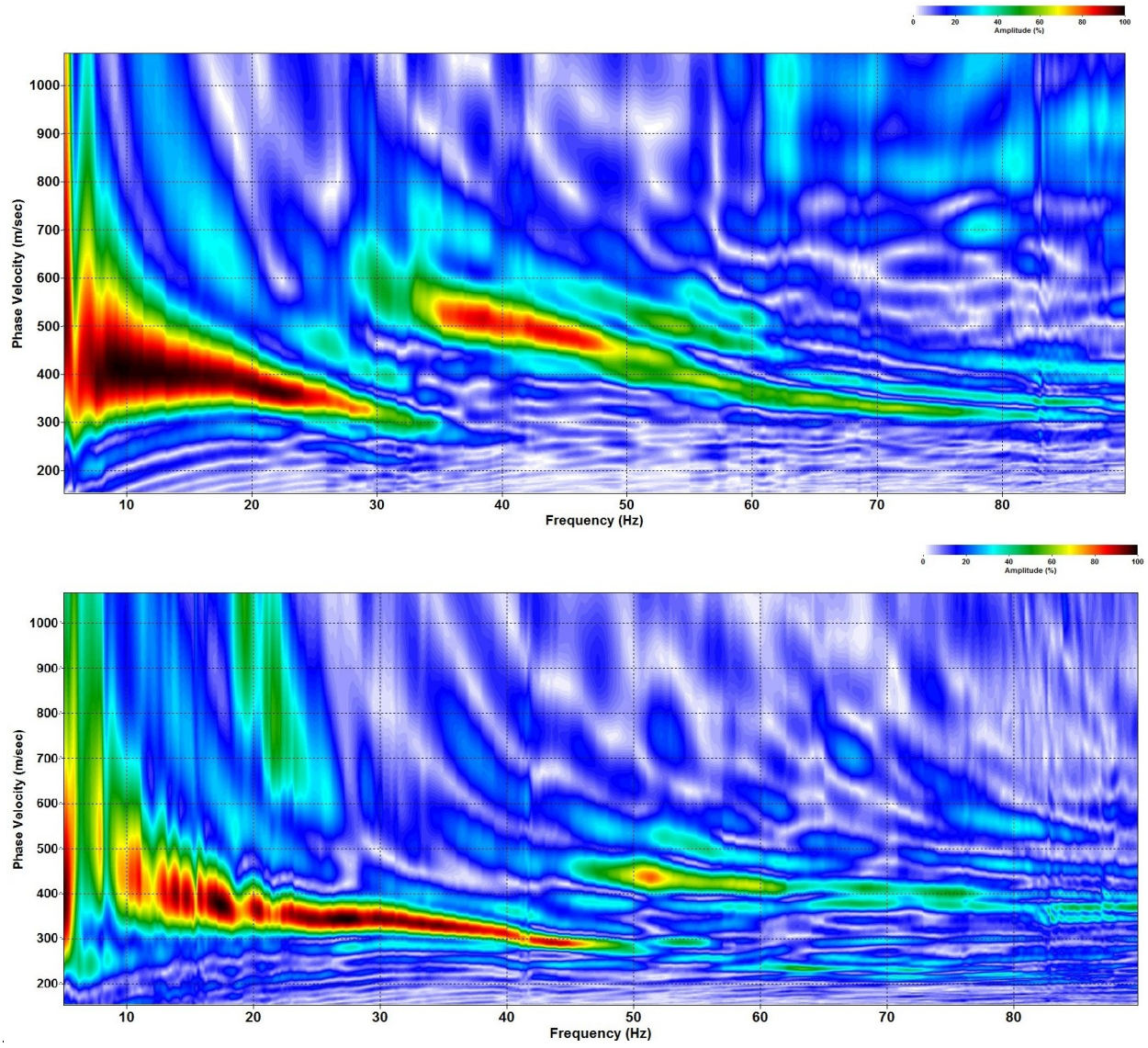

Figure 20: Upper) Unmuted record with strong higher-mode contamination past 30 Hz. Lower) Muted record above an approximate phase velocity of 450 m/s with increased bandwidth to 80 Hz.

Instead, it is related to a general velocity trend across the line with relative changes in the excitation of higher-modes resulting in variable cut-off frequencies. It is also noted that the fundamental frequencies below 30 Hz become less reliable as certain frequency data traveling near the velocities of the higher-frequency higher modes are partially muted. This agrees with the original research conducted by Ivanov et al. (2005a) where a disruption of low-frequency data was noticed with high-frequency gains. Thus, the muting technique acts as a two-edged sword in

extending higher-frequency data, while constricting the lower.

Although muting allows for a more aggressive picking scheme beyond strong fundamental signatures, inverting a line using this approach would create processing challenges. To limit uncertainty, the user would need to combine the low-frequency data from unmuted gathers, while appending higher-frequency picks from the muted record (Ivanov et al., 2005a). Also, there is some disagreement between the records for the intermediate-frequency phase velocities, so the cross-over frequency may need to be fluctuated with each midpoint. Muting was used intermittently across the line to constrain the dispersion-curve interpretations at high frequencies where HM contamination resulted in low amplitudes. This procedure ultimately ensured proper inversion, especially for the high frequencies of the ultra near surface, while limiting possible errors seen with low-frequency interference.

An in-depth analysis of a site's dispersion character is necessary to properly invert Rayleigh waves for *Vs*. Avoiding or restraining HM contamination with muting and an optimal offset range prevents erroneous inversion of curves that do not follow true fundamental signatures. Extending curves to reach asymptotic velocities ensure appropriate fundamental inversion of the uppermost stratigraphic layers. High-confidence picking routines lead to more accurate *Vs* estimations with layer models that converge to true velocity characteristics of a site.

5.1.3. Layer Model and Inversion

With an initial interpretation of dispersion character, the method continues to parameterization of the layer model and *Vs* inversion. Preliminary MASW sections applied 7-layer models to limit inversion instability and match assumptions of a homogeneous 'sand box'. This conservative parameterization ensured fast convergence to measured curves and restricted instability. A *Vp*:*Vs* ratio of 1.87 (Poisson's ratio of 0.3) was assumed to set initial *Vp* and

Poisson's ratio values as required by the inversion. The arid climate and negligible rain-fall of the area, along with initial assessment of the refraction data, confirm minimal subsurface saturation. A depth conversion ratio of approximately 35 percent generated an initial model and established the depth to the halfspace.

Wishing to incorporate accurate density values into processing, borehole logging was undertaken at all the wells drilled on site (Figure 21). However, as the AquaLock sampler system was used, the local substrate was subjected to water flooding. The sonic sampler works with water above the cutting shoe that acts to create a vacuum seal to extract samples. When retrieving a sample, some of this water is transferred to the sample, and some is transferred into the casing. This resulted in a water flood of the borehole with each extraction phase. As a detailed log of the drilling progress was not kept, specifically when each well was completed and how much water was 'lost' per well, the pore saturation at the time of the density logging cannot be estimated. Therefore, the density values may be skewed from the material properties of the site. As such, individual wells were not tied to proximal sections of the survey lines. Each well's density data was smoothed along the depth axis using a 21-pt (0.6 m) moving average filter. These smoothed well values were then averaged at each depth increment to obtain a mean density profile for each line.

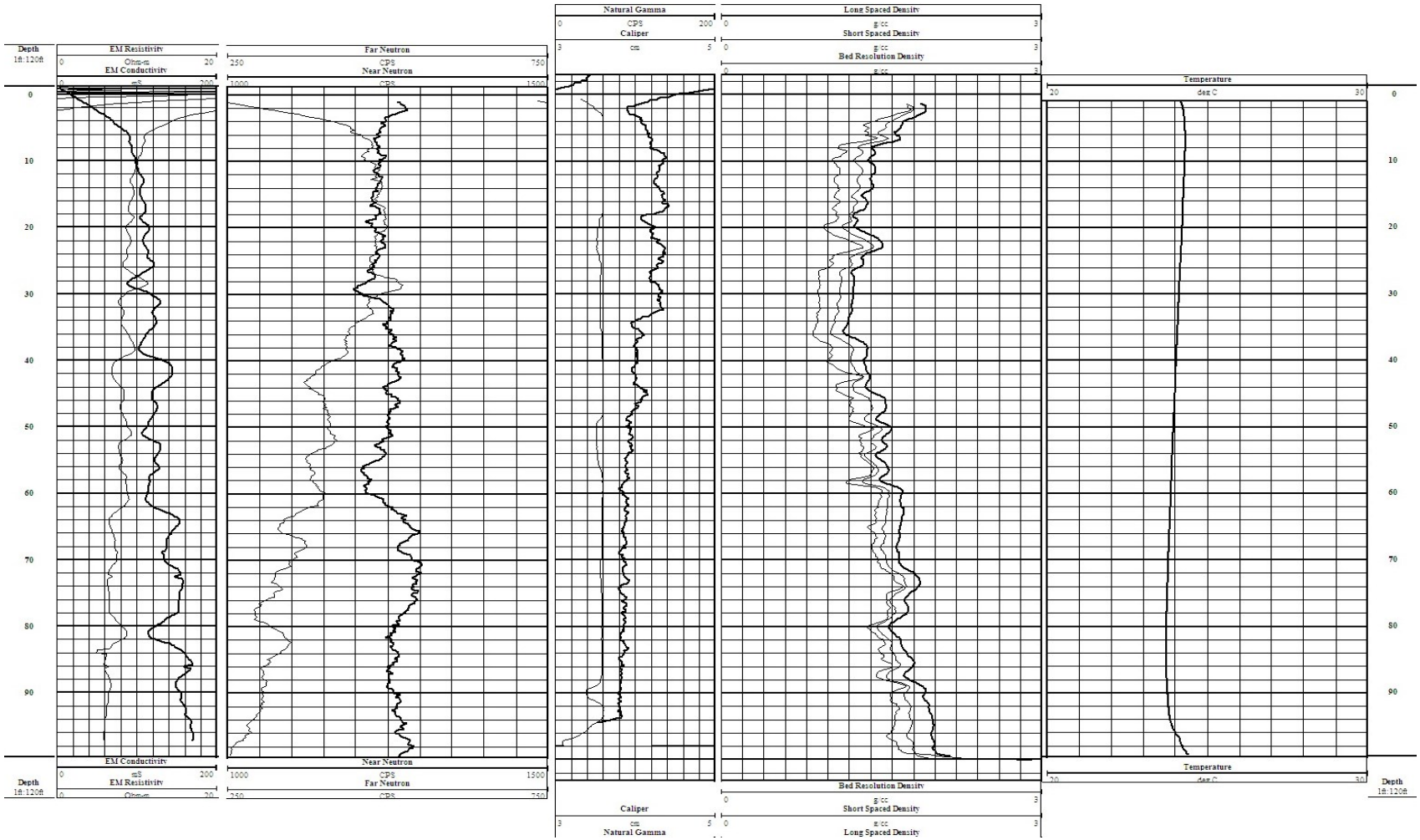

Figure 21: Well log suite for well 11. Logs include: temperature, density, gamma, neutron, and resistivity/conductivity.

This treatment sought to limit the possibility of local water-saturation effects on the borehole density; however, it assumes that the elastic properties are relatively equivalent across the site and the stratigraphic layering is consistent with the negligible changes in surface elevation.

Inversion was initially guided by a smooth convergence of the misfit function to a reasonable match between the calculated and picked curves. Stopping RMS error was somewhat inconsequential as solutions were manually stopped as convergence reached an asymptotic trend and a reasonable curve match. Careful attention guarded against large fluctuations of *Vs* values for individual layers that corresponded to small changes in curve character or RMS error. This procedure kept the inversion from converging to unrealistic models that conform to the non-unique topology of the misfit function. The inversion keeps the Poisson's ratio constant while updating *Vs* values (and *Vp* assuming a Poisson's ratio) with convergence.

5.1.4. Preliminary MASW Results

The above parameterization formulated an initial inversion scheme for the Yuma site. Due to the variability of the fundamental energy, the inversion results disregard the upper 3 m. Velocities values above this depth have limited or no frequency to phase-velocity data to constrain the inversion. Although the layer model takes this uppermost section into consideration, the lack of data constraint limits the confidence of these measurements and ultimately results in an averaging of the wave field beyond the intrinsic sampling of the Rayleigh-wave. This treatment ensures the results are representative of the data. This is especially important with the interpolation of 1D midpoints into 2D grids. The tomographic methods assume 'thin rays', which lose coverage as rays bend at velocity transitions. As initial constraints will work with refraction results that were limited to such depths, all models are shown to 12 m below the surface. Later sections will include MASW results that extend to deeper strata (see Chapter 8). To facilitate viewing, all models have

an approximate 4:1 vertical exaggeration; all profiles are shown from E-W (low-high station number). The 2D interpolated results are pictured below in (Figure 22).

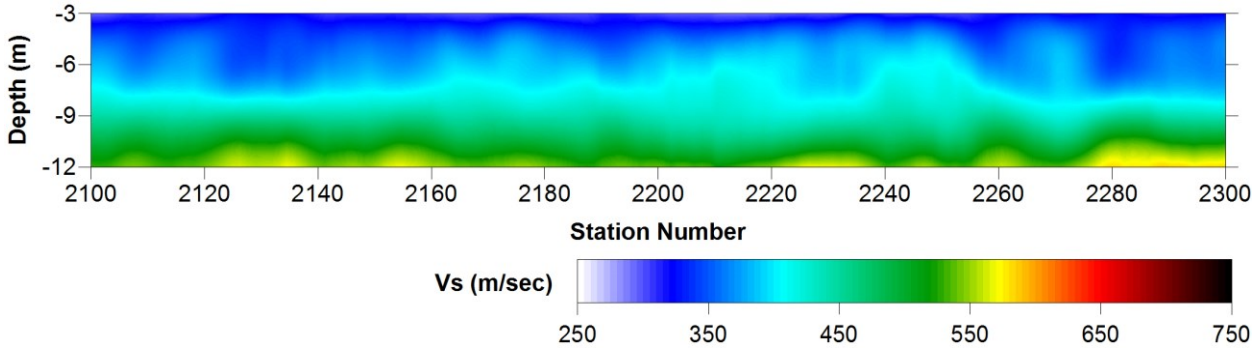

Figure 22: Initial, few-layer MASW inversion of the YPG data. Note the lack of stratification and apparent smooth transition to 9 m.

As expected, the low number of layers produces a statistically smoothed 'average' of the 1D velocity estimate. Intrinsically, a smooth model creates layers that cover wider sections of the curve. Any fluctuations of the curve will be linearly approximated by a reduced number of layers, thereby restraining the possible *Vs* oscillation with iterative convergence. Moving away from a sparse layer model, care must be taken to adequately constrain increased stratification.

5.2. *Vs*-JARS Approach

Next, the preliminary MASW *Vs* profile (Figure 22) is used as a reference model and refined with a complimentary refraction inversion using S_H first-arrival tomography. This scheme allows body wave information to update a smooth-parameterized velocity function that constrains the nonunique refraction solution space. The model was re-gridded using Surfer, to obtain a 1.2 m by 1.2 m cell size following the JARS implementation (Ivanov et al., 2006b). Polarized shot gathers were vertically stacked to enhance shear-wave arrivals (Figure 23).

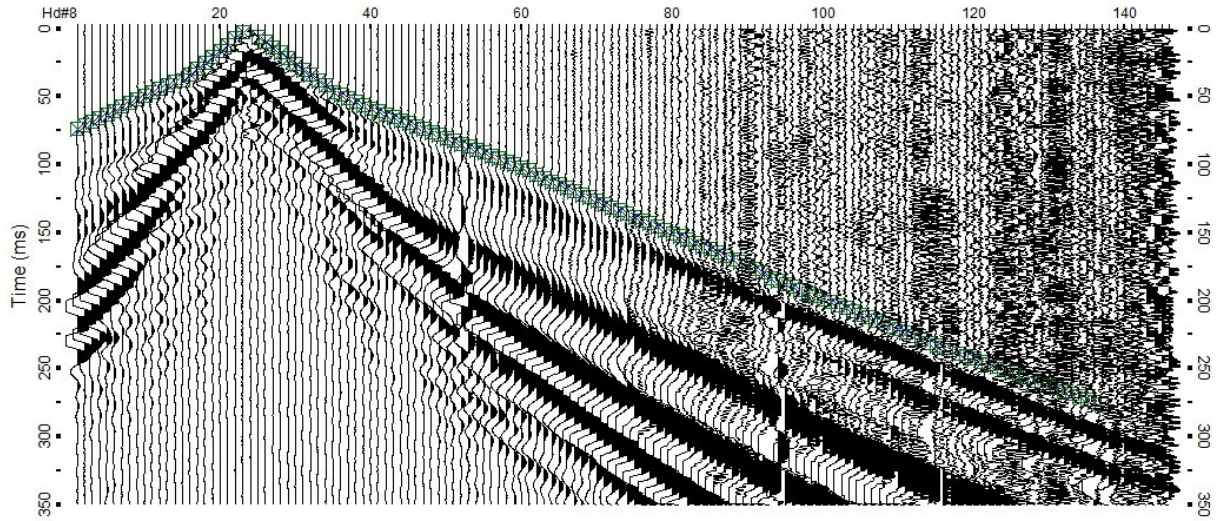

Figure 23: Representative S_H-wave hammer shot gather of reversed and vertically stacked polarities, with first-arrival picks (in green).

After an initial search for smoothing and iteration values, a *Vs* profile was attained using first-order horizontal regularization (Figure 24). Regularization coefficients were selected that allowed for stable conversion to a realistic model that agreed with relative velocity values found during previous geophysical surveys in the area. Incorrect coefficients resulted in unrealistically high velocity values (>50% deviation from MASW), velocity discontinuities produced by irregular ray coverage, and non-convergence. By relying on the initial MASW model to steer conversion, and applying reasonable horizontal smoothing parameters, a more realistic model is

reached that relies on physical measurements rather than gradient generalizations or best-guess approximations. Using smooth MASW models as a reference reduces the threat of hidden-layer scenarios and produces *Vs*-models in accordance with local geology. Additionally, the relaxation of vertical regularization, in lieu of letting the MASW model drive initial vertical gradients, allows a LVL solution not accepted in many refraction approaches.

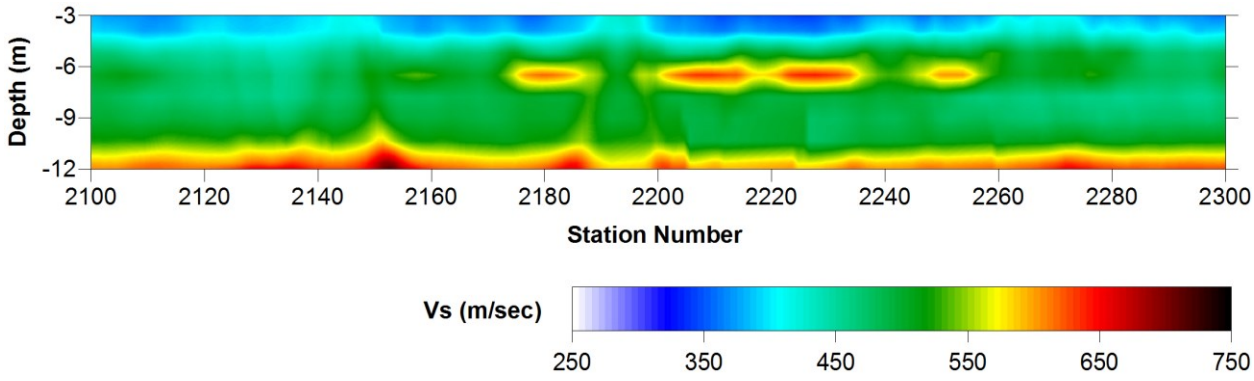

Figure 24: S_H-wave refraction tomogram using *Vs*-JARS approach. Note the high-velocity layer at approximately 6 m.

The updated velocity model found with *Vs*-JARS application, presents a constrained layer-model guided by Rayleigh-wave and body wave information and distinct inversion methods. These complimentary methods garner a higher-resolution image of the subsurface, not previously found with classical smooth MASW techniques. The structural findings of the refraction study (i.e. Figure 24) give empirical data to support a more stratified MASW layer model.

With evidence to support increased layering, the *Vs*-JARS tomogram was then used to update the layer model of the initial preliminary MASW inversion. The new MASW model was formulated on the velocity structure (layer thickness) of the tomogram and updated density values from the borehole-logging investigation (Figure 25). Such an approach mimics the layer-splitting strategy presented by Socco et al. (2010a), although here the method is not limited to the intercept

time method's layer-parameterization. Furthermore, this method may further divide layers along sections of interest, in the vertical sense, to allow greater flexibility during inversion.

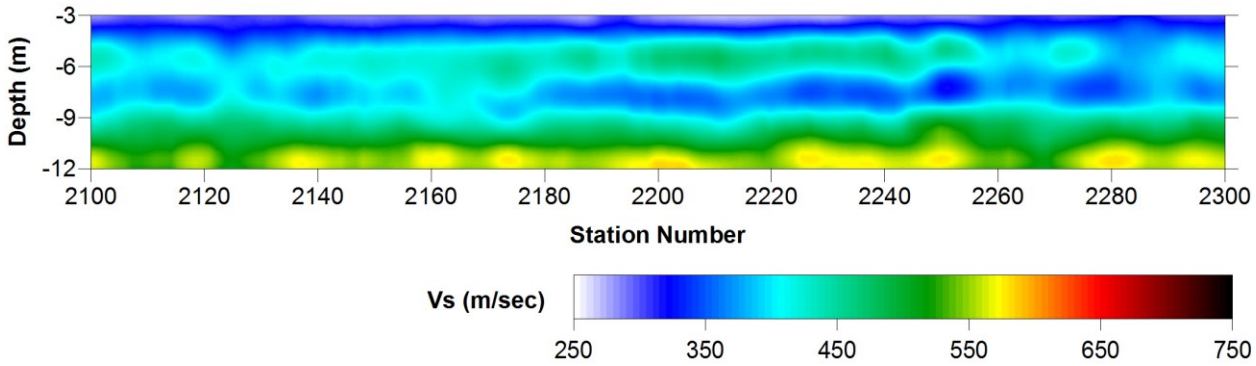

Figure 25: Constrained MASW *Vs* section. Note the incorporation of the HVL at 6m.

To demonstrate repeatability, increase the confidence of the velocity models, and reevaluate the methodology, the constrained-parameterization process was repeated for line 3. Moreover, refraction tomography analysis was performed with both S_H- and S_V-vibroseis data along both lines. The line 3 data sets followed the same general trend from smooth to higher-resolution imaging of the Rayleigh wave field using optimized constrained-parameterization MASW techniques (Figure 26). A HVL layer is also apparent using the S_H-hammer data for line 3; however, the signature is more subtle with a decreased vertical velocity gradient. The S_H-vibroseis results also show a HVL, giving more confidence to the analysis. In comparison, a greater disparity is seen between the S_H-wave datasets and the S_V-vibroseis tomogram.

A complete compliment of line 2 data is shown below (Figure 27). In contrast to line 3, the four velocity profiles show greater agreement across source and shear-wave mode.

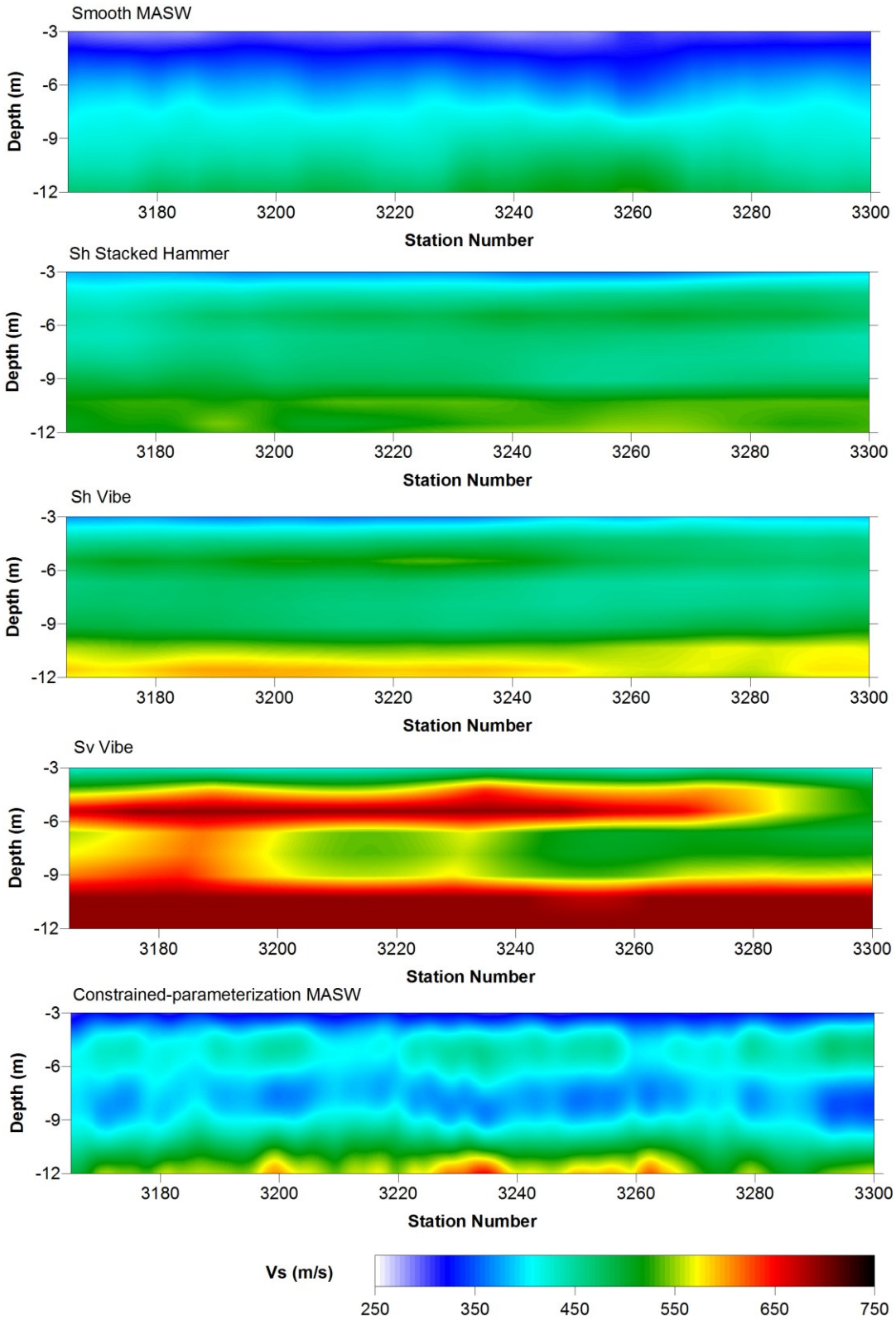

Figure 26: Results of repeated methodology for line 3. Note the similar structural pattern of the S_H- and S_V-methods and also the mismatch of the Sv-Vibe velocity values.

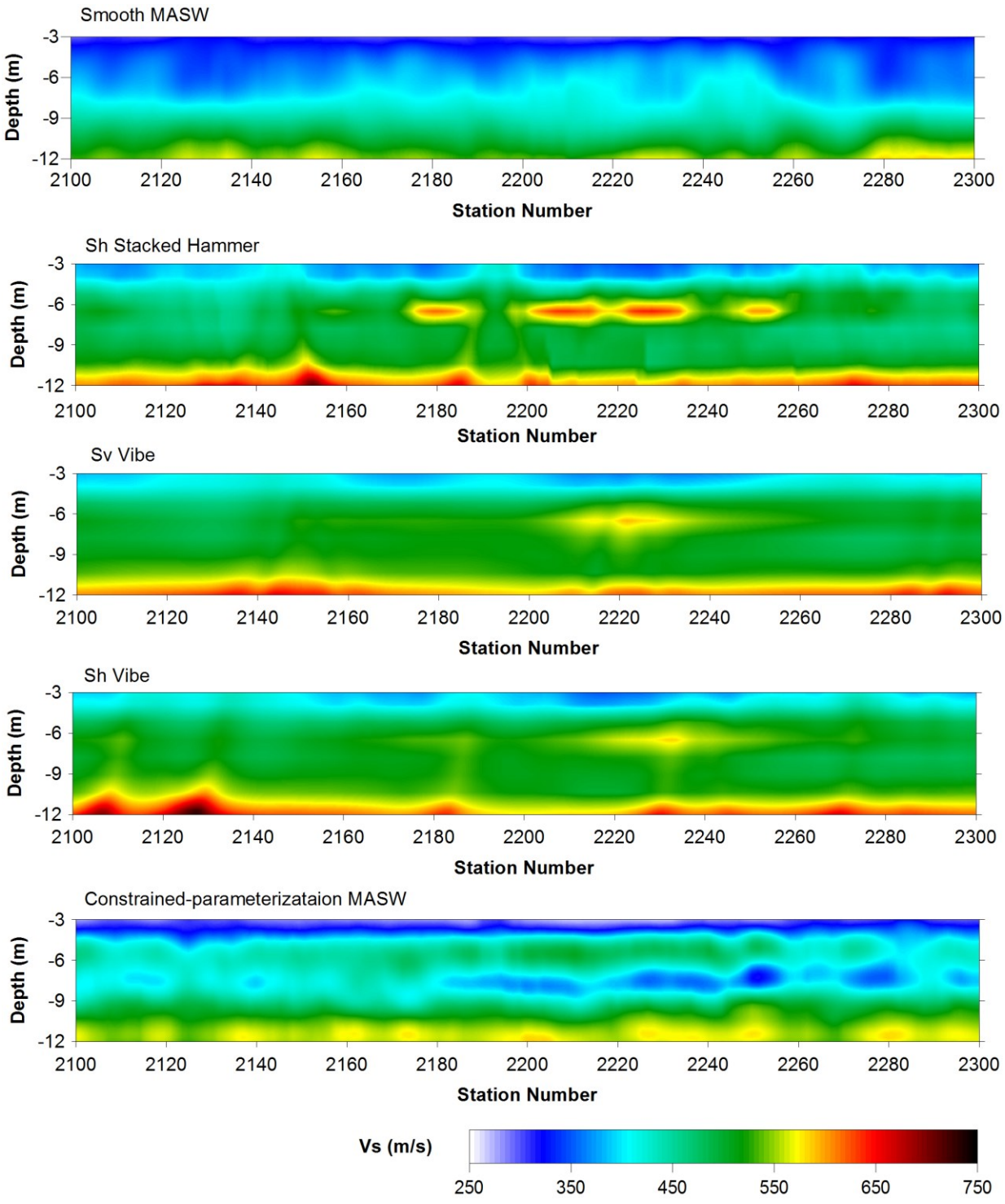

Figure 27: Tomogram comparison for line 2. Note the structural and velocity agreement between the S_H- and S_V-methods.

5.3. *Vp*-Tomography (JARS)

In an attempt to further constrain the MASW inversion to include *Vp* information, *Vp* tomography was performed for both lines. In a similar manner to the *Vs*-JARS approach, regridded smooth MASW results served as reference models to constrain the solution space of the tomographic inversion. As a caveat, these inversions don't use the same parameterized layer-models as discussed above for the *Vs* tomograms. The JARS approach assumes a *Vp*:*Vs* ratio to formulate the starting layer model; the results presented below assume a ratio of 2. A *Vp*:*Vs* ratio map was also calculated from the *Vs* constrained-parameterization MASW results (Figure 28 and 29).

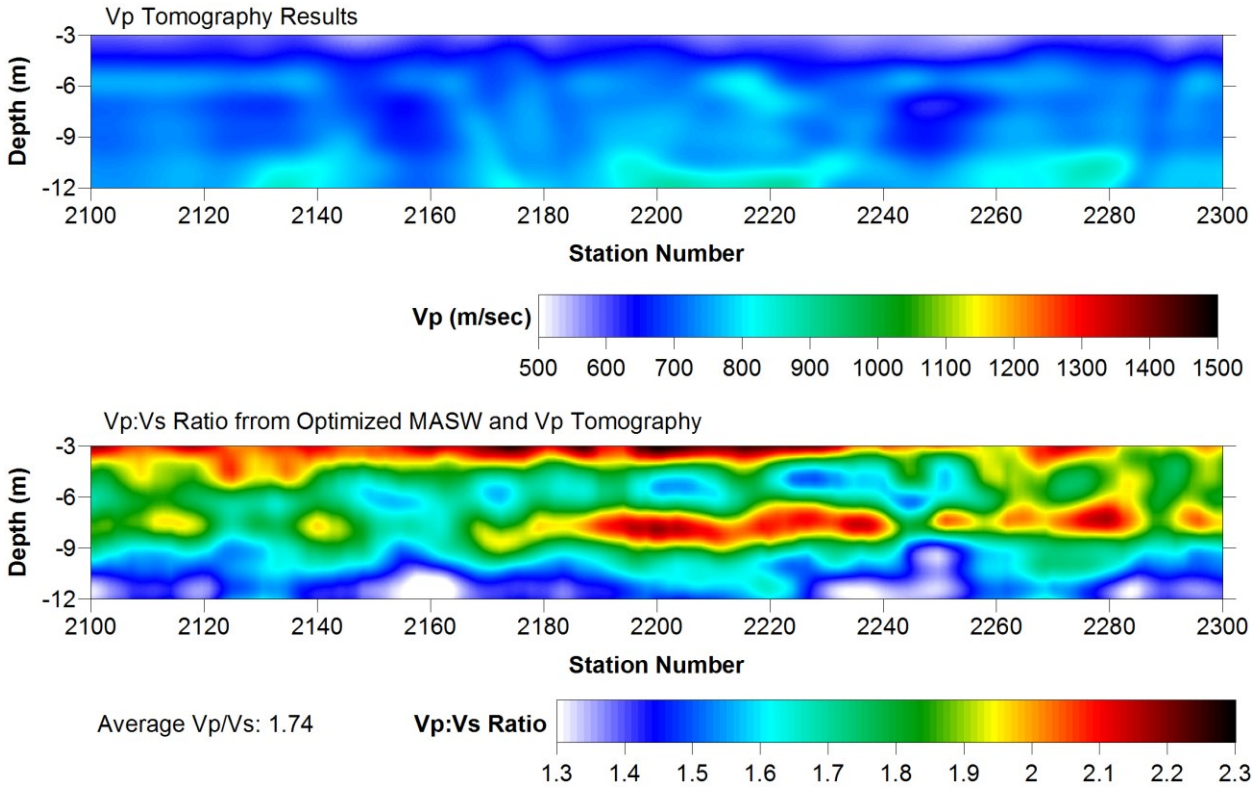

Figure 28: Line 2 *Vp*-tomography results and *Vp*:*Vs* ratio map.

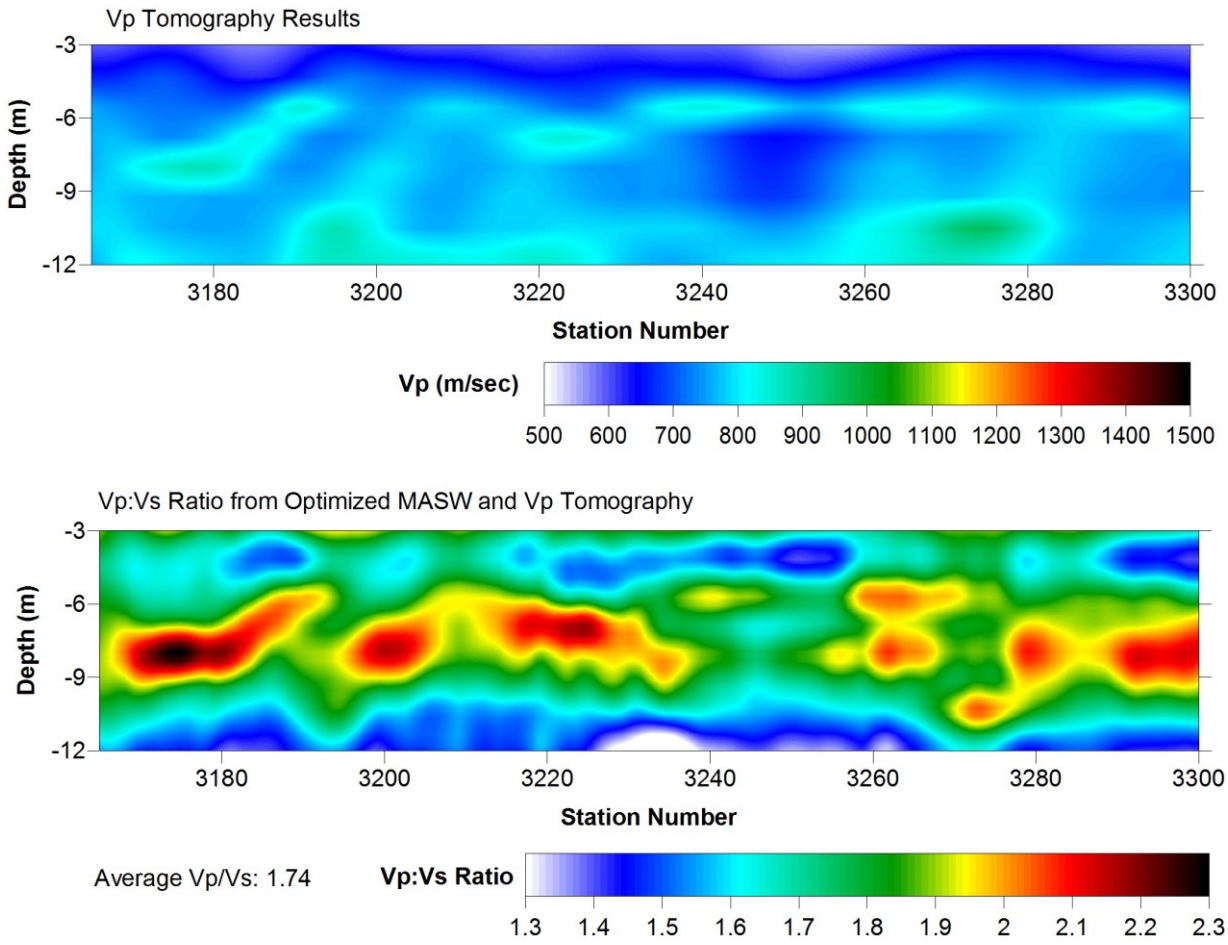

Figure 29: Line 3 *Vp*-tomogram and *Vp*:*Vs* ratio map.

Both *Vp*:*Vs* ratio maps include uncharacteristically low values (<1.5). These are thought to be an effect of the relative accuracy and non-unique convergence of both geophysical methods. Also, the *Vp*:*Vs* maps suggest there is a disconnect between the *Vp* results and the *Vs* constrained-parameterization MASW model, particularly at the layer transition below 10 m. Including updated *Vp* results (e.g., Poisson's ratio, layer structure) in final MASW processing, is needed to increase *Vp*:*Vs* ratios to more realistic values (> 1.5). Interestingly, both lines have an average *Vp*:*Vs* ratio of 1.74 for the images shown.

To further substantiate the *Vp*-tomography findings, a standard velocity/intercept time depth calculation was made for representative refraction data of line 2. First arrivals were manually assessed, across several shot points, to reduce near-source and time-break variation. Following visual changes in dips, the arrivals were then fitted with a three-layer model (Figure 30).

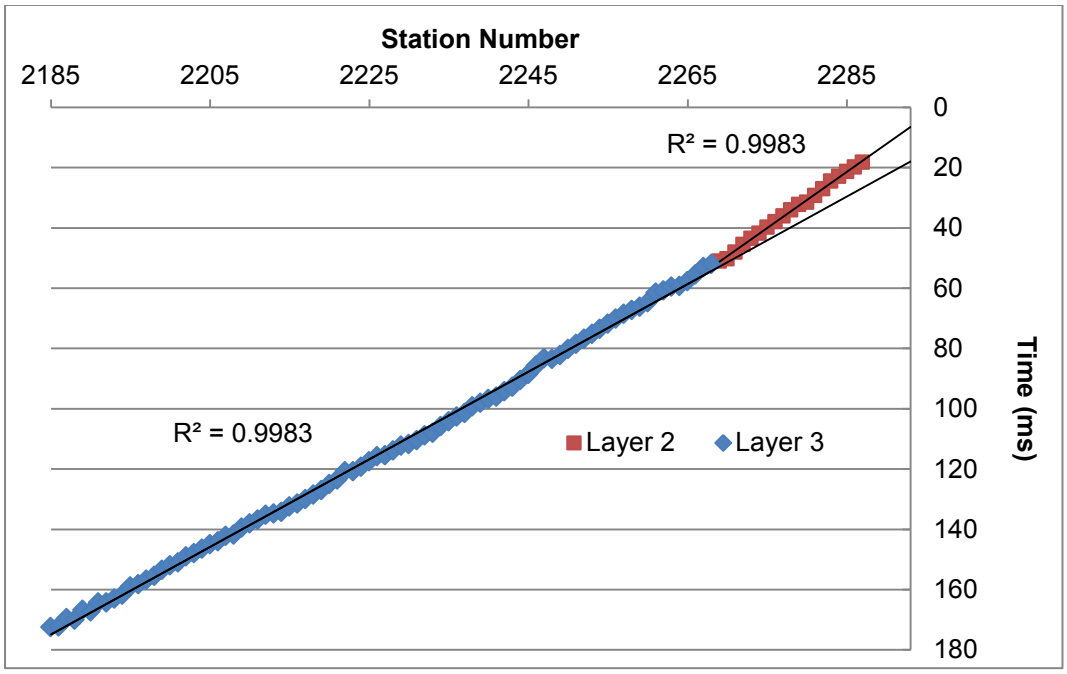

Figure 30: First-arrival gather with 3-layer refraction interpretation.

Standard least-squares methods fitted a line to the arrivals from which velocity and intercept time estimates were calculated. Depths to the second and third layers were calculated using standard intercept-time methods. An estimate of the apparent velocity variation was obtained by examining the variation of velocity for a 20-station segment across offset (Figure 31).

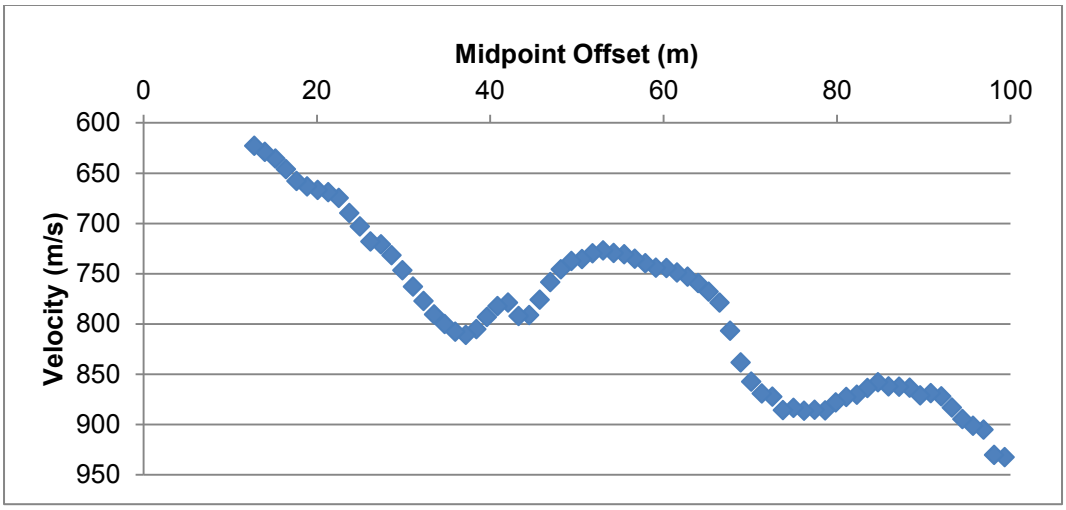

Figure 31: Graph of a moving 20-point least-squares fit of the first-arrival data given in figure 29. Note the oscillation of apparent velocity not interpreted with the standard 3-layer assessment.

One may notice that there are several inflection points across offset and a general increase in velocity with offset. While some variance is related to signal/noise ratio, statics, etc., the geology that causes these variations is not resolved using standard methods and a several-layer parameterization. However, the three-layer velocity and depth estimates generally agree with tomographic inversion (Table 2).

Table 2: Intercept-time refraction results.

V1	396 m/s
V2	653 m/s
V3	838 m/s
Z2	1.6 m
Z3	5.5 m

Using this simple method, the more statistical refraction approaches discussed above may be confirmed. The direct wave is in line with Rayleigh-wave character using the asymptotic value of the dispersion curve (222 m/s), which correlates to a *Vp*:*Vs* ratio of 1.8. The second layer moves the velocity gradient transition seen on the *Vp* tomography at 3 m to 1.6 m. The third-layer

estimates match well with the ~6 m HVL given in optimized MASW results and the previous *Vp* tomography analysis. Moreover, the *Vp*:*Vs* ratio for the third layer is in agreement with the previous results, with a value of 1.76. Although there are slight differences (layer 2), the relative velocity values and layer depths are consistent with the *Vp* refraction inversion methods.

6. Constrained-Parameterization MASW Discussion

6.1. *Vs*-JARS and MASW

Refraction and surface-wave methods incorporate different assessments of velocity-model resolution with unique inversions of independent seismic information. MASW's vertical resolution is a function of both the interpretable frequencies and the layer model. As we invert surface-wave data, longer wavelengths average velocities over their 'ray' paths, resulting in increased smearing for deeper layers. Ignoring such effects and interpolation, the number of layers in a 1D profile will determine the overall smoothness and vertical differentiation of the resulting 2D model. In comparison, refraction-tomography resolution is a function of cell size and ray coverage/density (assuming 'thin rays'). Additionally, the regularization of the refraction problem affects the resolving power of rays, as each iteration step is modified by these subjective controls. A highly regularized solution may reduce artifacts at the cost of horizontal and vertical model resolution. Similarly, MASW's vertical 1D approach to *Vs* inversion restricts lateral resolution by averaging heterogeneity over the spread length. The use of both inversion schemes works to balance the limitations of each method and increase the overall resolution of final *Vs* models.

Compared to MASW, the nonuniqueness and regularized solution to refraction tomography introduces a more dynamic inversion routine prone to processing-induced error and artifacts. However, the *Vs*-JARS method reduced the solution space inherent with tomographic inversion and ensured confident layer parameterization. More importantly, this application was able to provide a LVL solution, which may not have been possible using standard tomography methodology. With MASW, the use of a distinct layer model results in a more constrained, simplified 1D inversion and interval velocities that are directly related to the dispersion curve. Conversely, if not adequately stratified, the layer model may exaggerate smoothing. The solution

variability of refraction tomography is guided by MASW results to effectively constrain convergence.

The HVL structure, found with *Vs*-JARS routines, may be interpreted as an artifact of our parameterization. A linearly increasing velocity gradient and classical refraction methods may adequately converge to site first-arrivals. However, the constrained-parameterization approach is guided by physical measurements (seismic response) of the site, rather than generalizations. Moreover, the optimized MASW results independently confirm the presence of a HVL. It is the joint analysis that gives greater weight to a more stratified MASW layer model, while limiting concerns of instability and confirming refraction findings. The constrained-parameterization approach increases the confidence of the HVL structure due to repeatable, independent analysis using multiple geophysical methods for support.

6.1.1. Line 2

The MASW survey had shot points located every 2.4 m, while the refraction analysis was limited to a 20-station or greater shot-point interval. Also, the MASW line used a 78 m spread to create the dispersion images, where the refraction survey could theoretically differentiate 1.2 m^2 cells. The high degree of smoothing required to stabilize (regularize) the refraction inversion, along with further spaced shot points may hamper imaging smaller-scale horizontal anomalies. However, the refraction survey initially identified the HVL and indicated more-distinct lateral breaks compared to the final MASW profile. It was only after a more stratified layer model was implemented with refraction constraint that MASW was able to delineate the upper HVL.

The *Vs* tomograms and constrained-parameterization MASW model imaged a lateral pinch-out, or loss of coherence, of the HVL left of station 2175 and right of station 2260. Nevertheless, the S_H-hammer refraction profile provided more distinct lateral and vertical

boundaries. Conversely, the hammer tomogram had multiple artifacts resulting from raypath coverage and ineffective smoothing; the elliptical arcs at 2194 and the abrupt lateral velocity change at 2225 and 9 m are examples in the S_H-hammer section. With respect to other features, all surveys confined the uppermost layer to 4 m depth and the lowermost layer to 11 m. It is noted that the refraction tomograms (hammer vs. vibe) are not identical. Due to changes in source and geophone coupling, shot point coverage, raypath geometry, time-picks, smoothing constraints, and convergence there are small differences in the velocity field for each section.

This study reaffirms the intrinsic smearing of MASW (horizontal and vertical), and suggests that refraction analysis may better define anomalies at the cost of velocity artifacts. The ray coverage varied for specific inversions as convergence, dependent upon regularization controls, dictated preferential velocity structures. Final models were chosen to limit the loss of ray coverage across the model in response to regularization controls and convergence. Model sections below zones of high *Vs* must be analyzed for ray coverage to assure adequate resolution of the model to depth and defend a 2D interpolation and expression of LVL solutions. Overall, the two methods produce complimentary *Vs* information that strengthens the site's velocity interpretations.

6.1.2. Line 3

The refraction results display more variance for line 3, expressing the vulnerability of the refraction method to subjective inversion controls. Elevated smoothing parameters notably reduced ray-coverage artifacts, as seen in line 2 results, but also limit the methods ability to resolve lateral heterogeneity. The S_H-hammer refraction tomogram had a lower gradient HVL, in comparison to line 2 S_H-hammer results. Line 3's shear-wave vibroseis surveys also show more differentiation as a result of inversion convergence error. However, the S_H-vibe tomogram

conforms to the structural interpretations of line 2 with a more distinct HVL layer. The line 3 results identify a trade-off between model smoothness (artifact reduction) and horizontal model resolution.

The S_V-vibe refraction model was chosen to give an example of the issues of non-uniqueness and the limitations inherent with the convergence of deterministic methods. The model converged upon over-estimated velocities as raypaths passing through the HVL and basal layers drove the model to higher velocities at the precipice of nonconvergence. As more rays pass through the HVL portions of the model (following Snell's Law), intermediate LVL rays (lower in number) receive less weight on each iterative update. In effect, the solution is moving towards a several layer solution that negates the LVL solution and promotes a high-velocity gradient. Limiting the iteration number before such structure and velocities are manifested is evidence of tomography's nonuniqueness and demonstrates the subjective control that is essential for proper inversion of first-arrival refraction tomography in the presence of LVL solutions.

As a whole, line 3 results suggest a more coherent and laterally continuous HVL across the site. There is also a shift in the top of the HVL from approximately 6 m across line 2 to approximately 5 m on line 3; MASW results show a less dramatic shift. The basal layer signature of the HVL is comparable to line 2 results with a similar velocity (MASW) and depth (both tomography and MASW). Likewise, the top layer is evident above 4 m, although slightly thinner with the shift of the HVL. Lastly, the LVL below the 6-m deep HVL is more laterally continuous with a consistent thickness of 3 m.

Density logs across the site and the sparsely sampled geologic logs along line 3 suggest high material variability (e.g. clay content, Figure 4); however, in situ measurements lack great correlation on the order of stratigraphic interpretations as only one well continuously sampled the

site (well 10.5; Miller et al., 2010b).

The iterative approach to updating both the tomographic and MASW starting layer-models resulted in complimentary *Vs* profiles. The *Vs*-JARS application was proven successful for both lines at the YPG site. However, line 3's Sv-vibe data express the need for careful analysis of refraction convergence to limit instability and unstable divergence from realistic solutions (nonconvergence). Also, regularization-data incompatibility may result where smoothing constraints inhibit convergence or numerically over-smooth a problem. This is manifested as lateral inconsistencies in the first-arrival convergence (preferential velocity/shot-to-shot-point match). Multi-method assessment of a site's velocity structure allows a qualitative assessment of solution fitness to guide refraction-inversion parameterization. Refraction solutions should be relatively similar to the initial values of MASW inversion and dispersion trends. By using multiple sources/inversions, a constrained velocity profile was garnered for the respective lines with extraneous velocity perturbations (>50% deviation) recognized and accounted for.

6.2. RMS Error

Further iterations and starting-model refinement of the tomography's inversion parameterization (iteration number, smoothness values, starting layer model), not shown here, lead to decreased RMS errors, but also resulted in unrealistically high velocities for the HVL and deeper strata based on known material properties, resultant *Vp*:*Vs* ratios, and relative MASW values (e.g., line 3 S_V-vibe tomogram). Taking into consideration an ambient noise/error floor, imperfect data constraint (non-infinite data, cell discretization, etc.), and the effects of smoothing constraints, a global minimum (lowest RMS error) may reach a solution that is less related to the data/geology, but rather a statistical manifestation of the inversion scheme.

Indeed, the idea of global minima may be misunderstood during any inversion study. Care must be given to understanding the limitations of specific inversion schemes to defend against 'over-working' a data set. The processor must make a calculated decision on where to stop an iterative, deterministic problem. The same applies to global search methods, which are more sensitive to such miscalculations as there is often unrestrained variance and no qualitative measure of a model's fitness beyond RMS error.

6.3. P-wave Tomography (JARS)

P-wave tomography has the same inversion limitations as the *Vs*-JARS methods listed above. The results for line 2 and line 3 show general agreement for the structural character garnered from the *Vs*-JARS approach. In contrast, the HVL is less pronounced and coherent across line 3 and both lines show a less coherent basal layer. In general, the P-wave tomograms used lower smoothing constraints which might have guided the solution to a more discontinuous stratigraphic sequence. On the other hand, the models have near identical basal signatures from X200-X220 and X260-X280. When compared to the S-wave tomogram results, the HVL has a smaller variability in depth across lines.

Of interest for many engineering studies is the Poisson's ratio, or the comparable *Vp*:*Vs* ratio, which generally speaking is a measure of the ratio of bulk to shear moduli. The *Vp*:*Vs* ratio was calculated for both lines 2 and 3 using the *V*p-tomography and *Vs* optimized MASW profiles. The results (Figure 28 and Figure 29) may lead many to question the validity of the velocity measurements from field data at this site. One explanation is that dispersion is often not accounted for in laboratory testing, which tends to lead to overestimated *Vp*:*Vs* ratios (Mavko et al. 2009). Das (2002) gave a ratio range of 1.63-2.5 for loose sands. White (1965) and Gregory (1977) give a minimal *Vp*:*Vs* value of 1.5 for loose sands. Indeed, the lower values for the site push below the

acceptable levels for the geology of the area.

When looking at the geologic report (e.g., Figure 4) the high clay content would suggest higher *Vp*:*Vs* ratios more consistent with those as found in lab tests (Prasad et al., 2004). However, the geologic report suggests most depths have greater than 40% clay content, which means the soil matrix (load-bearing) is clay with lesser amounts of sand/silt. With this composition, we may expect the bulk system to respond to the increased porosity associated with increased clay content beyond a critical limit (Marion et al., 1992). Salem (2000) gave an overview of several Poisson's ratio studies and restated the relation to a decrease in the *Vp*:*Vs* ratio with increasing porosity. We may speculate that the porosity increase seen with an increase in clay, with variable sand and silt content, is driving the system to lower Poisson's ratios. Similarly, we would expect lower ratios given a more pure sand layer, as indicated in some geologic reports (i.e., well 14, Figure 4).

David Boore's unpublished data on unconsolidated sediments' *Vp*:*Vs* ratios also gives credence to the low ratios of the YPG site (Boore, 2007). Boore examined data from 274 borehole sites in southern California and found many wells trend to a *Vp*:*Vs* ratio of approximately 1.87 (0.3 Poisson's ratio) with routine variance to below 1.63 (0.2 Poisson's ratio) when under unsaturated conditions (Figure 32).

The average change in velocity needed to alter all the values found in the *Vp*:*V*s maps to 1.6 or greater would correlate to a change of less than 5%. This deviation is within the inherent uncertainty of the MASW method (Xia et al., 2002) without consideration of the affects of refraction tomography's uncertainty. However, the low values (<1.5) are a sign of inversion error, or method incompatibility (*Vp* data point vs. *Vs* data point). The final MASW inversion will need to incorporate *Vp* information to adequately constrain the inversion and keep ratios above a given threshold (1.5). Also, the *Vs* tomography and MASW results suggest a more laterally continuous

layer structure, particularly below 10 m. Increasing the smoothing parameters for the *Vp* tomography would smear the velocity section, and increase the *Vp*:*Vs* ratios.

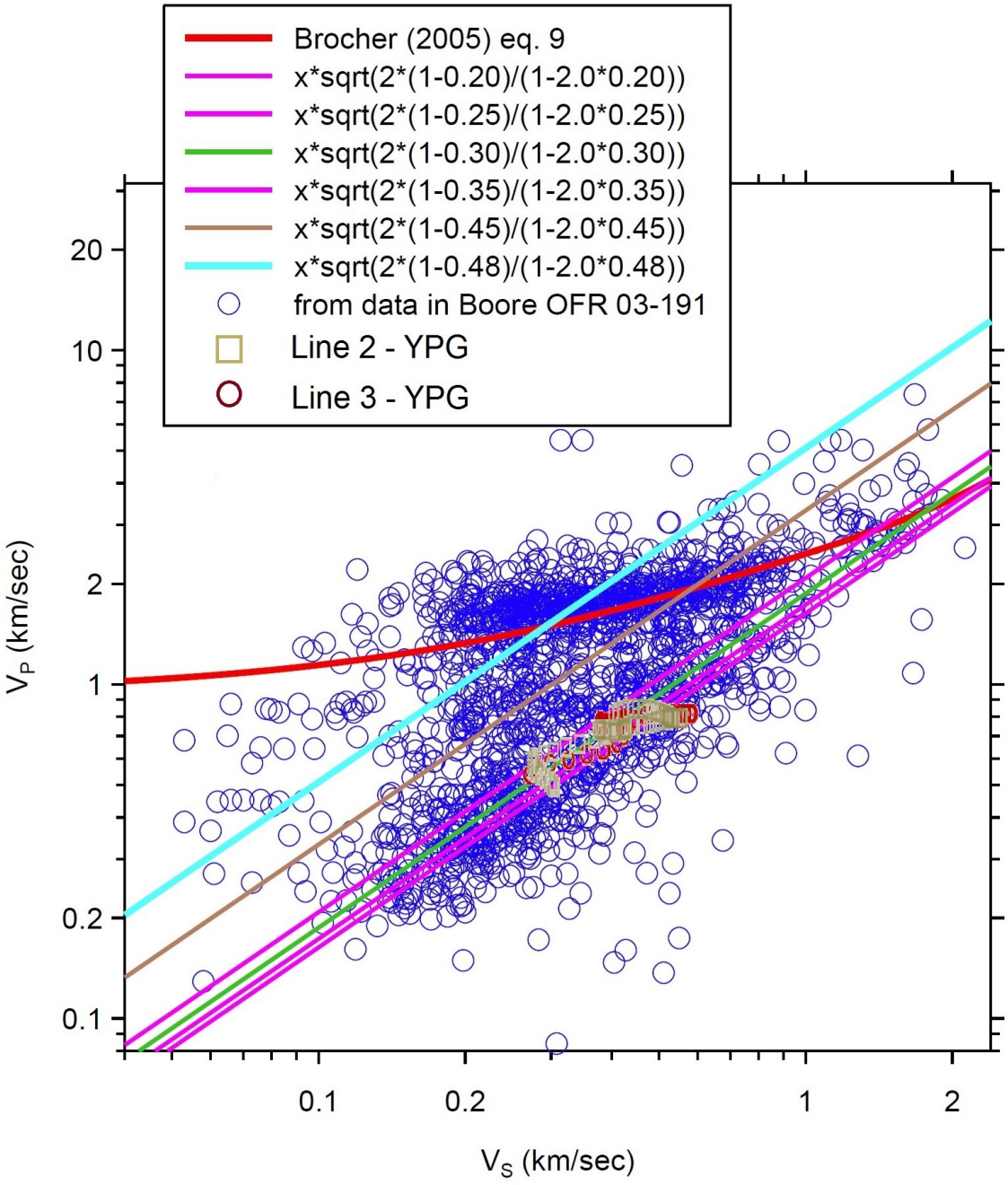

Figure 32: Figure displaying data from 274 boreholes, with Poisson's ratio lines in various colors (after Boore, 2007). Note the lower trend centered below or in the vicinity of 0.3 (*Vp*:*Vs*-1.87, the green line) with many values below 0.2 (*Vp*:*Vs*-1.63, the lowest pink line). YPG data averaged across layers is overlain for comparison.

7. Constrained Inversion Conclusion

The proposed *Vs*-JARS application with coincident analysis of the MASW method provides more possibilities for near-surface seismic-data analysis. The application of MASW and refraction traveltime tomography permits evaluation of the *Vs* structure of an area using different yet complementary portions of the seismic wave field. As the methods utilize entirely different inversion schemes and wave-mode propagation, their integration should garner a more complete understanding of the velocity structure. This evaluation suggests the integration of MASW with refraction traveltime tomography leads to a more constrained MASW layer model with increased vertical resolution and a refraction tomogram that better defines lateral heterogeneity. The refraction solution provided superior lateral resolution and additional *a priori* data control for MASW layer-model constraint. The integrated approach may offer advantages to *Vs* estimation, especially for those sites that have limited information to steer initial study. This work recommends this joint methodology for future shear-wave investigations using MASW.

Using the constrained-parameterization approach, higher-resolution models were achieved for both geophysical methods that honor site first-arrival and dispersion characteristics. The limitation of LVL solutions and hidden layer problems associated with refraction analysis was mediated by incorporating MASW's initial model as *a priori* information. The relaxation of the vertical increase in velocity demanded by most inversion techniques, and the initiation of horizontal smoothing constraints, resulted in a more representative refraction image of the subsurface. Moreover, by using both P- and S-wave refraction information, we were able to assess *Vp*:*Vs* ratios, and add another fitness criteria to the layer model.

The method I am reporting on here suggests incorporating mode-consistent *Vs* tomography into MASW workflows may improve *Vs* estimation in several ways:

1. As found previously by Foti et al., (2003), Ivanov et al., (2006b), and others:
    a. Limit the non-uniqueness of the solution space inherent in refraction inversion
    b. Ability to confidently incorporate low-velocity layers into refraction solutions
        i. Capacity to mediate the hidden-layer phenomena of refraction problems
2. Compare mode-consistent (S-wave) velocity values through separate inversion schemes
3. Compare 2D (or pseudo-2D) variation of S- and P-wave fields
    a. Quasi-check on 2D approximation of interpolated 1D *Vs* sections
4. Create high-resolution MASW and refraction results constrained through joint analysis
    a. Increase lateral and vertical resolution of near-surface models
5. Construct QA/QC analysis based on a multi-method approach
    a. Associate model fitness beyond standard RMS criteria

8. Modeling of Site Characteristics

Inversion schemes ultimately assume 'perfect' imaging of dispersion characteristics. Imperfect spread parameters (offset selection) may produce images with poor resolution of modes (Foti et al., 2002), higher-mode domination (Cercato et al., 2010; Cornou et al., 2006), near-field non-plane-wave interference (Park et al., 1999), or poor sampling of longer wavelengths (Ivanov et al., 2008). An optimized offset selection will reduce negative effects and enhance the fundamental-mode signature. Rules of thumb have been developed for acquisition design, but are routinely disputed with actual field application (Xia et al., 2009; Xu et al., 2006; Zhang et al., 2004). The optimum offset distance for proper formation and sampling of Rayleigh waves is often determined during acquisition, but rarely involves adequate testing of acquisition effects on dispersion images.

Numerical modeling of the constrained-parameterization MASW layer model gives a measure of acquisition effects on dispersion imaging in the absence of noise and lateral heterogeneity. Without rigorous testing, or *a priori* knowledge, a balance between imaging lateral heterogeneity with shorter spreads and adequately sampling longer wavelengths with relatively longer spreads is not intuitive. Moreover, if there are geologic transitions across a site, competing fundamental-mode trends may overlay one-another. It is proposed that modeling may act to reduce uncertainty in acquisition effects and dispersion interpretation, thereby confirming/refuting preliminary findings.

Furthermore, the development of a layer model permits the forward-modeling of the theoretical modal curve(s) which should help in separating specific mode signatures from transformation effects and mode superpositioning. While the initial processing and interpretations are geared toward the fundamental mode and its inversion, this procedure will allow an

independent interpretation of the overtone image that includes higher-modes. The dispersion image may be thought of as an amplitude map with various independent events including: higher-modes, cross-over/cut-off frequencies, spectral leakage, coherent noise, etc. A 2D lateral sampling of the synthetic seismogram, gives an enhanced interpretation of the layer-model developed using the constrained-parameterization MASW approach.

The algorithm discussed by Zeng et al. (2011) was used to create synthetic seismograms that closely match both P-wave first-arrivals and Rayleigh-wave dispersion characteristics. The previous constrained-inversion techniques of Chapter 6 form the basis of the initial layer models ($\mathbf{v_s}$, $\mathbf{v_p}$, $\boldsymbol{\rho}$, $\mathbf{h}$; see section 3.1). The resulting synthetic S- and P-wave velocity models permitted an inference of the site's *Vp*:*Vs* ratio. Spread-length comparison led to qualitative estimations of lateral heterogeneity and the effects of acquisition parameters on specific frequency segments of dispersion images. In the presence of complex velocity structures, the use of modeling may help to constrain and improve the interpretation of Rayleigh-wave dispersion characteristics.

8.1. Model Generation

The modeling algorithm takes a layer model ($\mathbf{h}$), populated with density ($\boldsymbol{\rho}$), P-wave velocity ($\mathbf{v_p}$/*Vp*), and S-wave velocity ($\mathbf{v_s}$/*Vs*) to generate synthetic shot gathers. The initial values were guided by the results of Chapter 6. Preliminary layer models applied successively more discretized layering to assimilate the gradients apparent in the constrained-parameterization MASW *Vs* profiles. Refraction results were also central in guiding stratification of the synthetic layered-earth model.

The modeling algorithm used several parameters to match field acquisition. The source wavelet was a 35-Hz center-frequency first-order Gaussian derivative, mimicking the impulsive source. In order to match spectral characteristics, the wavelet was selected based on frequency vs.

amplitude analysis of the field/synthetic data and qualitative analysis of the synthetic wavelets, specifically the first arrivals. Simulating the field layout, the source offset was 1.2 m from the first geophone with a 1.2 m geophone spacing. The common-source gather consisted of 147 geophones. The full-spread seismogram, generated using the above parameters, was used for further processing (Figure 32).

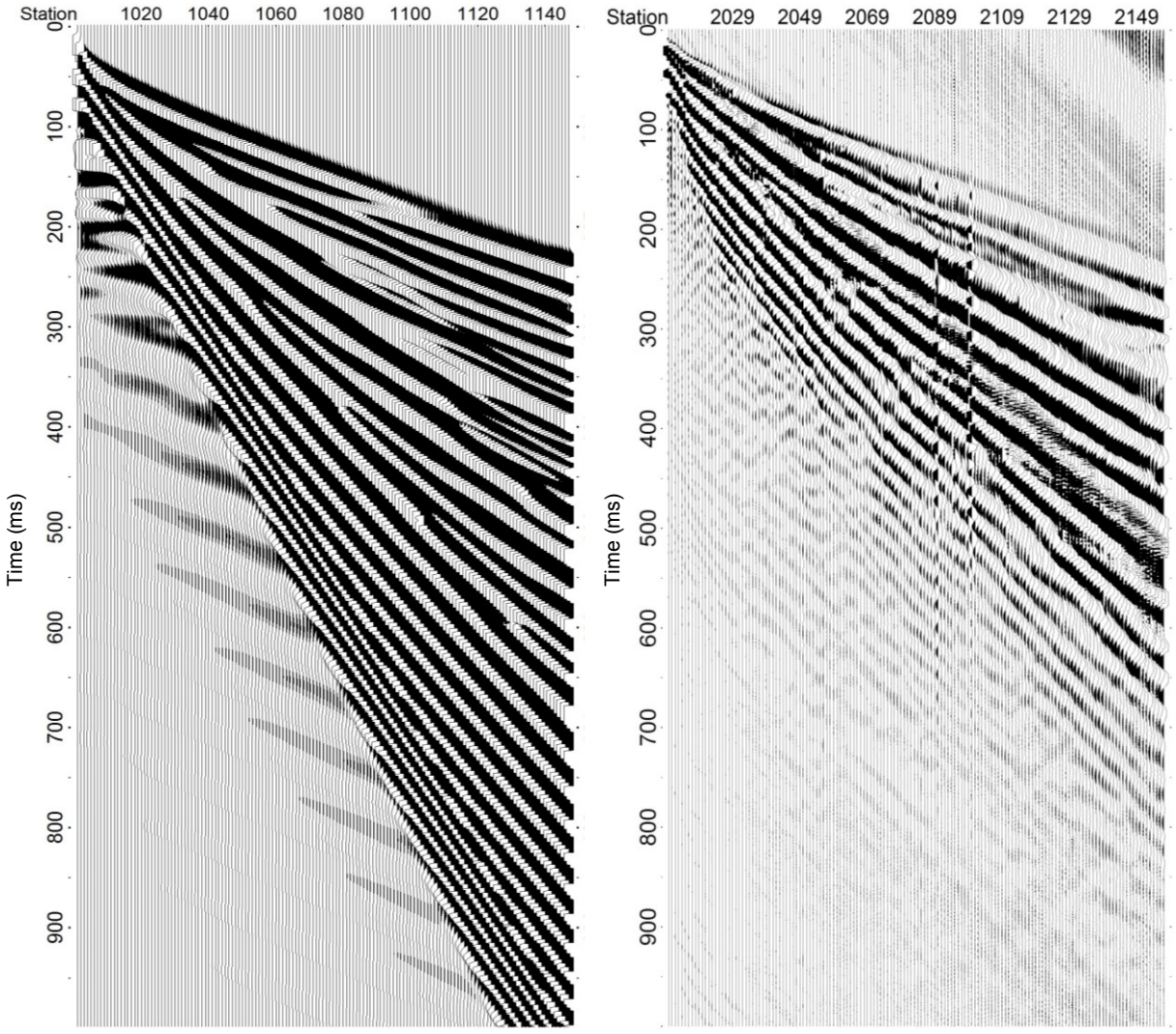

Figure 33: Left) synthetic shot gather of final layer model. Right) reference field gather for the YPG site. Note the relative match of the first-arrival trend.

Dispersion-curves were analyzed from consecutive synthetic seismograms (layer models). Each dispersion image was fitted to experimental data for comparison of both the fundamental and higher-mode curves. After minimal adjustments, a reasonable match was obtained between the experimental and synthetic dispersion curves. In addition, the P-wave first arrivals were assessed in relation to changes in the *Vp*:*Vs* ratio of the input models. The synthetic P-wave first arrivals were compared to several field gathers. From these comparisons, the average RMS error between offset-consistent picks was calculated to be approximately 9ms. The *Vp*:*Vs* ratio of the synthetic velocity models was 1.7, reaffirming the average previous calculated from independent tomography and MASW surveys.

The 11-layer half-space model used to generate the synthetic seismogram was the final constraint applied to the MASW layer model for lines 2 and 3 (Figure 33). The MASW models vary slightly with those of Chapter 6 (upper 12 m); they integrate the layer constraint of both P- and S-wave tomography along with the depth to halfspace and the *Vp*:*Vs* ratio of 1.7 found with the synthetic study (Poisson's ratio). The final models use more discrete layers, which resulted in lower velocities for the layer below 10 m and the LVL below 20 m. This also led to an increase in the *Vp*:*Vs* ratios as compared to the models in section 5 (>1.57). This exemplifies the necessity of continually adapting velocity models as site analysis dictates. As each new piece of information is added to the inversion scheme, the earth model will converge to a slightly different solution. Additionally, the synthetic modeling allowed for a final check on the depth to the half-space and a confirmation of the deepest structure, or layers, of the model-space. Although the cyclical methodology is laborious, the treatment gives the processor the most control and eventual highest confidence in the final model.

Local heterogeneities cause lateral changes in the individual layer velocities. Where the

model case assumes a homogeneous, horizontally layered system, vertical discontinuities are evident across the lines. Moving from one 1D profile to the next, there are obvious changes in the dispersion character, which are not accounted for in the synthetic modeling. The lowest velocities of the LVL, centered at 25 m, may suggest some instability of the problem. The homogenous, synthetic model nowhere 'perfectly' matches the final *Vs* MASW images, however, the general character of the velocity section is maintained.

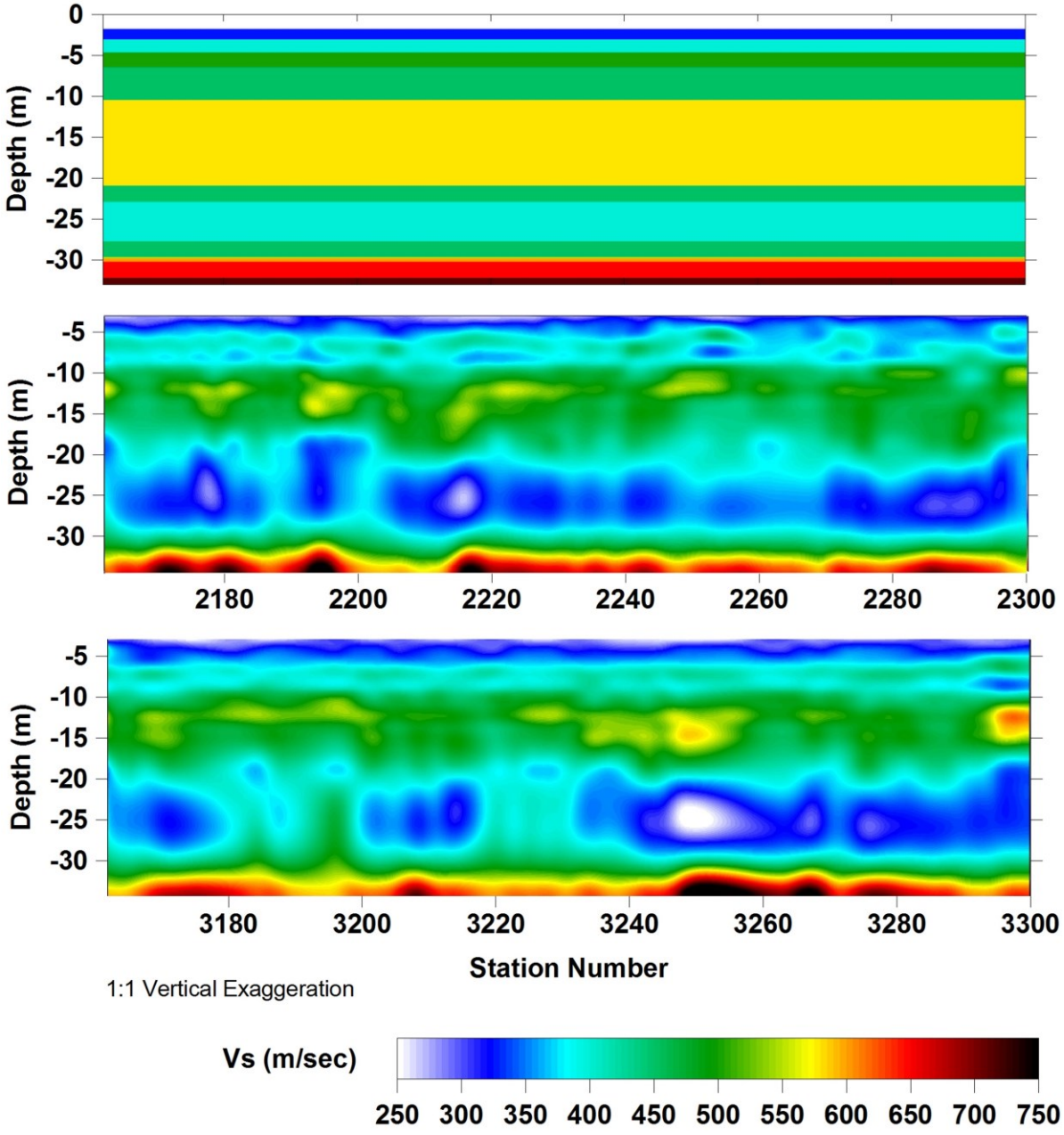

Figure 34: Synthetic model with equivalent final line 2 and line 3 constrained-parameterization MASW results to half-space depth.

8.2. Acquisition Effects

This section will look at conclusions drawn from the dispersion character of the synthetic data based on changes in the recording parameters (offset selection). Interpreting dispersion properties correctly, especially in the presence of complex velocity structure (LVL, HVL, HM excitation, etc.), is paramount to accurate inversion of Rayleigh waves. The figures of this section focus on the change in dispersion trends as a function of different spread lengths and source offset. This mimics the methods of Ivanov et al. (2008), as previously mentioned. As with any MASW survey, the synthetic seismograms are first transformed to the phase velocity vs. frequency domain.

Dispersion curves calculated from the full spread length closely match theoretical curves calculated by Schwab and Knopoff (1972), (Figure 35).

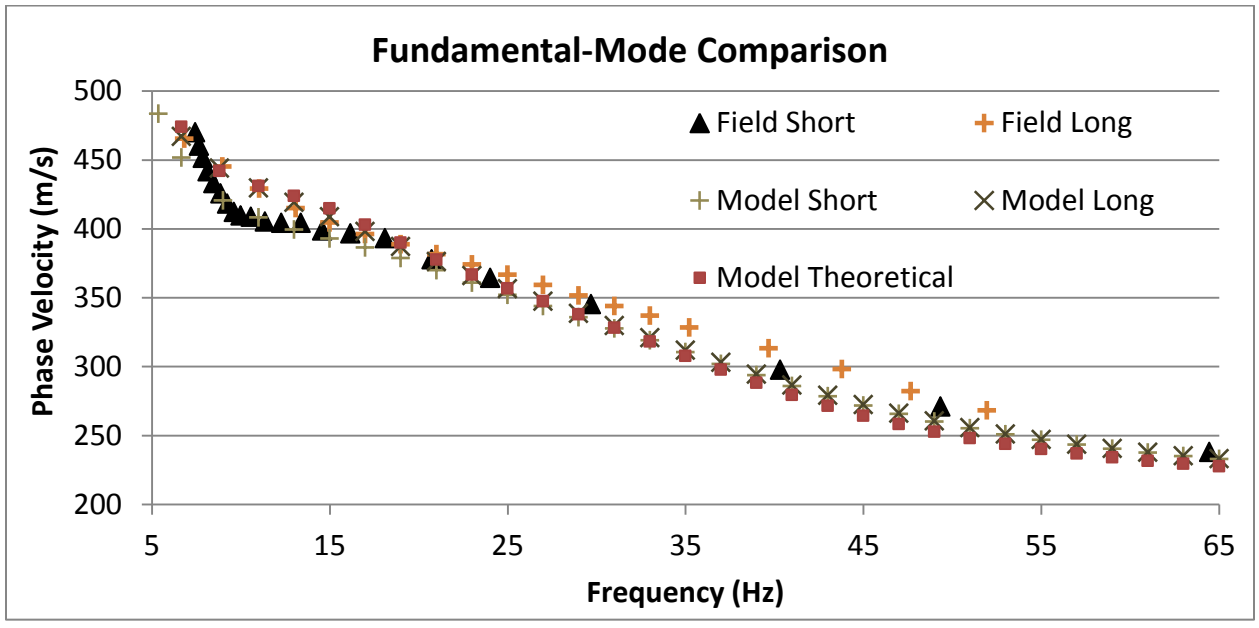

Figure 35: Graph of phase-velocity variation with spread length. All subsets have a 1 m source offset, where short refers to a 78m 65-geophone spread and long refers to a 178m 147-geophone spread. At maximum deviation, percent difference is under 6% for corresponding spread lengths. The slight overestimation at high-frequency model data, in comparison to the theoretical curve, is a result of the automatic picking routine.

Several inferences may be drawn from the comparison of the field and synthetic dispersion results. Reductions in spread length resulted in a separation of apparent phase-velocity trends at 10 Hz for both field and synthetic data sets. This verifies that the separation is not a function of lateral heterogeneity. Analysis of modeled dispersion images confirms that direct higher-mode interference and superposition is negligible (e.g., Figure 36, Figure 37). The velocity pull-down, of shorter-spread lengths, is attributed to spectral leakage and smearing within the frequency domain, resulting in a loss of resolution. Also, the slight separation above 25 Hz, observed in long spreads of the field data, is interpreted as spread-length averaging induced by lateral heterogeneity in the upper several meters of overburden.

The synthetic dispersion curves suggest the analysis begins to lose phase-velocity resolution below 19 Hz using the short spread. However, the curve trends back towards long-spread values below 7 Hz. This empirically quantifies the necessity of adjusting the processor's picking routines, which would otherwise be made on qualitative assumptions of curve variance with offset (as made in the preliminary phase of this thesis; even if correctly so). These frequency-dependent effects of the domain transformation were associated with an optimized spread length (e.g. Figure 37). The 65-geophone gather was obtained from a systematic sampling of field data. This resulted in an optimal spread-length and source-offset subset which balanced image and lateral-velocity resolution under the assumption of a subjective interpretation. Synthetic comparison reaffirms preliminary dispersion interpretation and gives a quantitative measure of initial qualitative assessments.

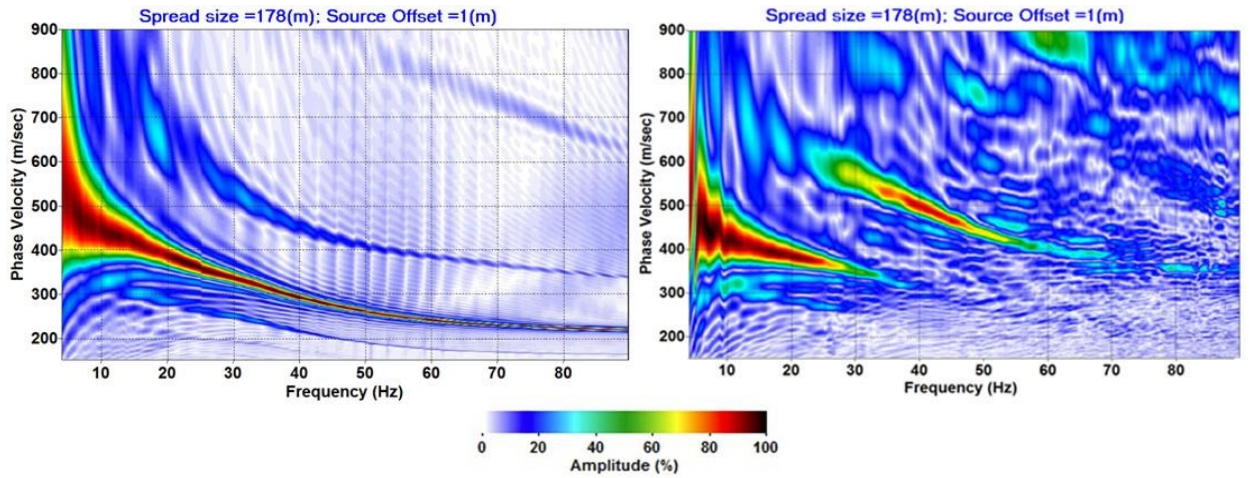

Figure 36: Dispersion curve comparison for the full 147-geophone spread length (178 m spread: synthetic data to left, field data to right). Note the higher-amplitude HM energy in the field data.

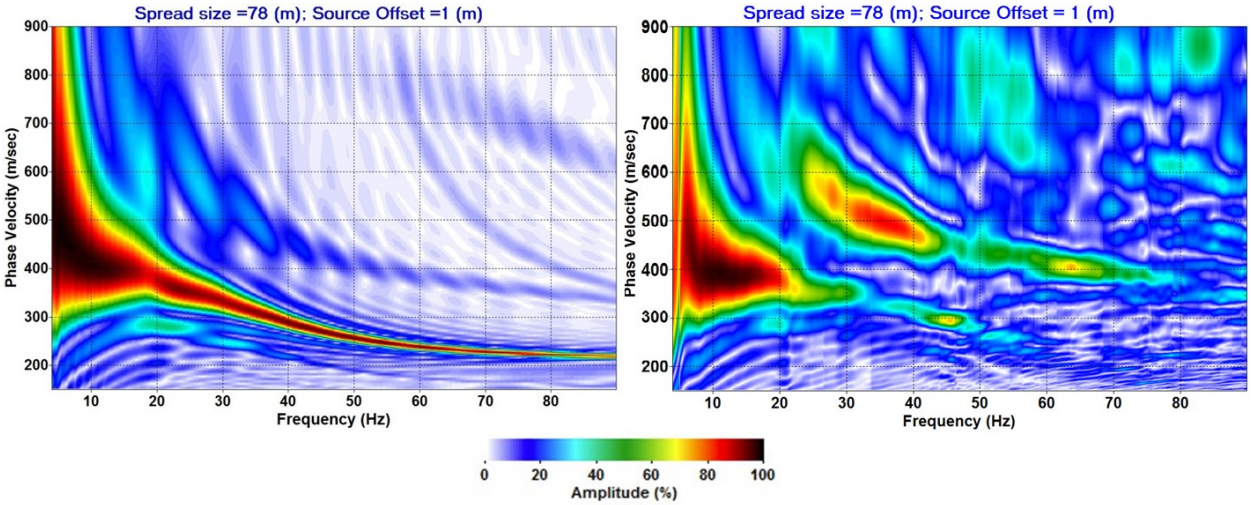

Figure 37: Dispersion character comparison for the optimized 65-geophone spread length (78 m spread: synthetic data to left, field data to right). Note the amplified HM interference at frequencies greater than 25 Hz on the field data.

Longer source offsets resulted in mode superposition and higher-mode velocity pull-ups of the fundamental in the same frequency-band affected by spectral leakage (Figure 38). Field data suffered more than modeled data from these mode-interference patterns; this is believed to be due to attenuation effects and additive coherent signal (scattering, etc.) from local heterogeneity not incorporated into the synthetic model. These disruptions of the wave field produced a zigzag

phase-velocity trend that was the most compelling support for using closer source-offsets, with the optimized spread-length, during preliminary investigations.

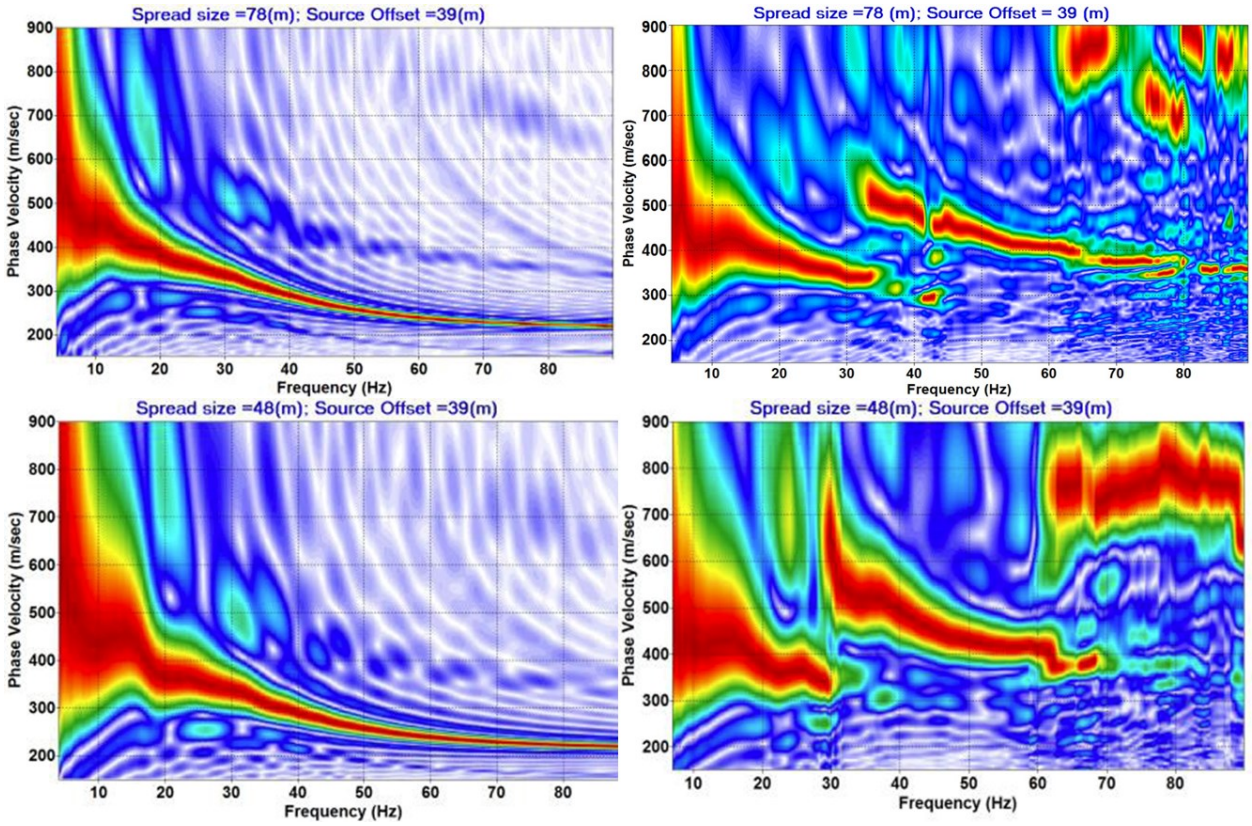

Figure 38: Sequence of dispersion curves prepared from different acquisition parameter subsets: Left) Model data, Right) Field data.

The field data was affected by attenuation, resulting in incoherent and discontinuous fundamental-mode signatures below a 200-800 ms sloping 'timeline' on the shot gathers (Figure 33). Conversely, the elastic-modeling algorithm did not incorporate attenuation analysis into wave propagation. This discrepancy between the synthetic and field data was approximated with muting (Ivanov et al., 2005a). A long-taper bottom mute was applied to both data along this slope to introduce attenuation. The field data showed little change in the dispersion image, while the modeled image saw a drop in the high-frequency amplitudes of the fundamental (Figure 39). Moreover, muting on synthetic gathers enhanced the cut-off frequency around 30 Hz, past which

the fundamental-mode became over-estimated and the true trend was obscured in field data. This suggests that attenuation and near-field near-surface scattering of the fundamental-mode Rayleigh wave may intensify the effects of higher-mode excitement and hamper dispersion interpretation after domain transformation.

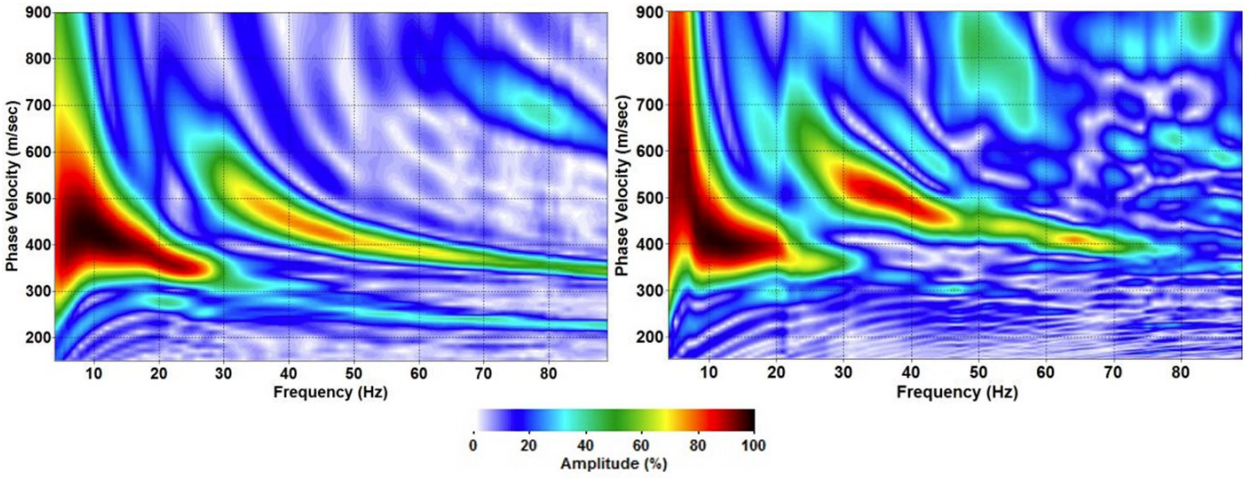

Figure 39: Muted gathers of the model (left) and field (right) data. Note the improvement in overall qualitative match between the curves' modal trends.

Using the muted gathers, the dispersion character of the model data reaches a better match for the entire overtone image. The higher-mode starting below 600 m/sec, which previously had comparatively lower contrast in the model data, now more closely matches the field response. Calculating the theoretical higher-mode curve of the synthetic model, we see that this HM energy is the first higher mode. My approach allows for a HM evaluation of the model space, which was based entirely off of fundamental data analysis. This check on model fitness is a major advantage of this approach and allows significant constraint on the interpretation of modal trends beyond standard MASW workflows.

8.3. Modeling Conclusions

Complicated *Vs* structures introduce some potential error when interpreting dispersion images. Selecting optimal acquisition parameters may be seriously under-constrained without ample site analysis. For the inversely dispersive model, analysis of the processed waveform was negatively affected by loss of resolution and the finite windowing of the x-t domain; which agrees with previous research (Foti et al., 2002; Xia et al., 2006). Comparison of low-frequency synthetic data with complimentary field gathers verified that the modal responses of certain frequency data were an effect of wavelength sampling and domain transformation rather than local heterogeneity, as assumed in preliminary interpretation. Understanding how modal curves were affected by spatial sampling and acquisition parameters increased confidence in the optimal spread length and dispersion interpretations used in MASW investigations.

Classical research (Park et al., 1999) suggests a proper source offset is equal to the maximum depth of investigation (half the longest wavelength); in this case, approximately 40m. This rule of thumb caused erroneous modal trends and a 10% maximum overestimation of phase velocity. Non-optimal spreads were shown to add, or increase the severity, of modal inflection points, which could introduce inversion instability and lead to erroneous layer perturbations. On the other hand, a short offset resulted in a more sinuous curve, matching site dispersion characteristics, which underestimated velocities by less than 6% at maximum deviation. These outcomes suggest that shorter offsets, together with longer spread lengths, may be preferable to improve sampling of long wavelengths in certain geologic terrains (e.g. dry sand/clay soil sites).

Utilizing this modeling approach would benefit future surveys with a secondary estimate on dispersion interpretation, *Vp*:*Vs* ratios, layer-model parameterization, and the depth to the half-space. If dispersion interpretation would ignore zigzag patterns and introduce some

smoothing constraint on modal sinuosity, one might minimize the effects of imperfect acquisition parameter sets. For new sites, however, past experience and best-guess interpretation is often what geoscientists must rely on for preliminary results. Data-driven methodologies are always preferable, and adding synthetic modeling to compliment a constrained-parameterization MASW investigation gives greater insight into modal trends and their interpretation, with a final constraint on MASW inversion.

9. Final Thoughts

The constrained-parameterization approach outlined in previous sections, and repeated in Appendix III, combines qualitative interpretations and quantitative measurements geared to optimize the inversion of MASW data. The complimentary use of refraction and surface-wave methods allowed an in-depth examination of the seismic wavefield at the YPG site using body and surface waves. Mode consistent *Vs*-JARS provided multiplicity that improved confidence in the final structural interpretations of the MASW inversion.

The mixing of inverse theory and modeling permitted a dramatic increase in interpretability of the dispersive events captured with the experimental data and gave a secondary evaluation of the earth model. The synthetic modeling incorporated 2D-wavefield calculations into the MASW method. This could be used in future MASW research to limit the inherent 1D-2D disassociation of the approach. Integrating a 2D MASW inversion scheme, with the use of synthetic modeling as a forward-model operator, would dramatically increase the constraint on lateral resolution of the method and the overall information content of the analysis. Moreover, attenuation analysis could easily be integrated into the forward problem.

As a whole, each new analysis dictated a change in the parameterization of the MASW inverse problem. With proper refinement of the system, each new empirical data set better constrained the solution space. This led to a higher-resolution, higher-confidence, constrained-parameterization MASW *Vs* model. The gradual change of the earth model, given an evolving hierarchy of constraint, is seen as the main finding of this thesis.

10. References

Ackerman, H. D., L.W. Pankratz, and D. Dansereau, 1986, Resolution of ambiguities of seismic refraction traveltime curves: Geophysics, **51**, 223–235.

Anbazhagan, P. and T.G. Sitharam, 2008, Mapping of average shear wave velocity for Bangalore Region: A case study: Journal of Environmental and Engineering Geophysics, **13**, 69-84.

Anderson, N., T. Thitimakorn, A. Ismail, and D. Hoffman, 2007, A comparison of four geophysical methods for determining the shear wave velocity of soils: Environmental and Engineering Geoscience, 13, no. 1, 11-23.

Beaty, K.S. and D.R. Schmitt, 2003, Repeatability of multimode Rayleigh-wave dispersion studies: Geophysics, **68**, 782.

Bergamo, P., D. Boiero, and L.V. Socco, 2012, Retrieving 2D structures from surface-wave data by means of space-varying spatial windowing: Geophysics, **77**, no. 4, EN39-EN51.

Billington, E.D., R.J. Palm, and A.T. Grosser, 2006, MASW imaging of an abandoned Minnesota mine: Proceedings of the Symposium on the Application of Geophysics to Engineering and Environmental Problems (SAGEEP 2006), Seattle, WA, April 2-6, 482-491.

Boiero, D. and L.V. Socco, 2010, Retrieving lateral variations from surface wave dispersion curves: Geophysical Prospecting, **58**, 997-996.

Boore, D.M., 2007, David Boore's notes on poisson's ratio: David M. Boore Webpage, <www.daveboore.com>. March 10, 2013.

Boore, D.M., 1969, Efffect of higher mode contamination on measured love wave phase velocity: Journal of Geophysical Research, **74**, no. 27, 6612-6616

Casto, D.W., B. Luke, C. Calderon-Macias, and R. Kaufmann, 2009, Interpreting Surface-wave Data for a Site with Shallow Bedrock: Jounal of Environmental and Engineering Geophyscis, **14**, 115-127.

Cercato, M., F. Cara, E. Cardarelli, G. DiFilippo, G. DiGuilio, and G. Milana, 2010, Surface-wave velocity profiling at sites with high stiffness contrast: A comparison between invasive and noninvasive methods: Near Surface Geophysics, **8** , 75–94.

Cornou, C., M. Ohrnberger, D. M. Boore, K. Kudo, and P.-Y. Bard, 2006, Derivation of structural models from ambient vibration array recordings: Results from an international blind test: Proceedings of the 3rd International Symposium on the Effects of Surface Geology on Seismic Motion, paper NBT.

Dal Moro, G., 2008, Vs and Vp vertical profiling via joint inversion of Rayleigh waves and refraction travel times by means of bi-objective evolutionary algorithm: Journal of Applied Geophysics, **66**, 15-24.

Dal Moro, G., E. F. Pipan, and P. Gabrielli, 2003, Determination of Rayleigh wave dispersion curves for near surface applications in unconsolidated sediments: Society of Exploration Geophysicists, Expanded Abstracts, 24, no.1, 1049-1052.

Das, B.M., 2002, Advanced soil mechanics, 3nd ed: Taylor and Francis Group. 567 p.

Davis, N.O., and M.J. Culig, 2009, Geophysical logging results, Yuma Proving Ground, Raytheon OTD, Yuma, AZ: COLOG Division of Layne Christensen Company, Report, Dec. 2009.

Di Giulio, G., Sawaidis, A., Ohrnberger, M., Wathelet, M., Cornou, C., Knapmeyer-Endrun, B., Renalier, F., Theodoulidis, N., and Bard, P.Y., 2012, Exploring the model space and ranking a best class of models in the surface-wave dispersion inversion: Application at European strong-motion sites: Geophysics, **77**, B147-B166.

Dorman, J., and Ewing, M., 1962, Numerical inversion of seismic surface wave dispersion data and crust-mantle structure in the New York–Pennsylvania area: Journal of Geophysical Research, 67, 5227–5241.

Duputel, Z., M. Cara, L. Rivera, and G. Herquel, 2010, Improving the analysis and inversion of multimode Rayleigh-wave dispersion by using group-delay time information observed on arrays of high-frequency sensors: Geophysics, **75**, no. 2, R13-R20.

Eastman, Steven A. *Arizona Physiobraphic Areas*. Map, Arizona Department of Mines and Mineral Resources, 2007.

Ewing, W. M., W. S. Jardetzky and F. Press, (1967). Elastic Waves in Layered Media, McGraw-Hill, New York.

Forbriger, T., 2003, Inversion of shallow-seismic wavefields: I. Wavefield transformation: Geophysical Journal International, **153**, 719–734.

Foti, S., L. Sambuelli, L.V. Socco, and C. Strobbia, 2003, Experiments of joint acquisition of seismic refraction and surface wave data: Near Surface Geophysics, **1**, 119–129.

Foti, S., L. Sambuelli, L.V. Socco, and C. Strobbia, 2002, Spatial sampling issues in FK analysis of surface waves: 72nd Annual International Meeting, Society of Exploration Geophysicists, Expanded Abstracts, 11p.

Gavin, H., 2011,The Levenberg-Marquardt method for nonlinear least squares curve-fitting problems, Department of Civil and Environmental Engineering, Duke University, Apr. 2011.

Google Earth. Image capture: Arizona Map. March 6, 2013.

Haskell, N.A. (1953). The dispersion of surface waves on multilayered media, Bulletin of the Seismological Society of America, **43**, 17-34.

Healy, J. H., 1963, Crustal structure along the coast of California from seismic-refraction measurements: Journal of Geophysical Research, **68**, 5777–5787.

Helbig, K., 1986, Shear-wave - What they are and how they can be used: in Shear-wave exploration, S.H. Danbom and S.N. Domenico eds., Society of Exploration Geophysicists, 19-36.

Hunter, J.A., D. Motazedian, H.L. Crow, G.R. Brooks, R.D. Miller, A.J.-M Pugin, S.E. Pullan, and J. Xia, 2010, Near-Surface Shear-Wave Velocity Measurements for Soft-soil Earthquake-hazard Assessment: Some Canadian Mapping Examples: in Advances in Near-Surface Seismology and Ground-Penetrating Radar, SEG Geophysical Developments Series No. 15, R. D. Miller, J. D. Bradford, and K. Holliger, eds., Society of Exploration Geophysicists, 339-359.

Ivanov, J., R.D. Miller, J. Xia, and S. Peterie, 2010, Multi-mode inversion of multi-channel analysis of surface waves (MASW) dispersion curves and high-resolution linear radon transform (HRLRT): 80th Annual International Meeting, Society of Exploration Geophysicists, Expanded Abstracts, 1902.

Ivanov, J., G. Tsoflias, R.D. Miller, and J. Xia, 2009, Practical Aspects of MASW Inversion Using Varying Density: Proceedings of the Symposium on the Application of Geophysics to Engineering and Environmental Problems (SAGEEP 2009), Fort Worth, TX, 171-177.

Ivanov, J., R. D. Miller, and G. Tsoflias, 2008, Some practical aspects of MASW analysis and processing: Proceedings of the Symposium on the Application of Geophysics to Engineering and Environmental Problems (SAGEEP 2008), Philadelphia, PA, April 6-10, 1186-1198.

Ivanov, J., R. D. Miller, N. Stimac, R. F. Ballard, J. B. Dunbar, and S. Smullen, 2006a, Time-lapse seismic study of levees in southern Texas: 76th Annual International Meeting, Society of Exploration Geophysicists, Expanded Abstracts , 3255-3258.

Ivanov, J., R. D. Miller, J. Xia, D. Steeples, and C.B. Park, 2006b, Joint Analysis of refractions with surface waves: An inverse solution to the refraction-traveltime problem: Geophysics, **71**, R131-R138.

Ivanov, J., C. B. Park, R. D. Miller, and J. Xia, 2005a, Analyzing and Filtering Surface-Wave Energy by Muting Shot Gathers: Journal of Environmental and Engineering Geophysics, **10**, 307-322.

Ivanov, J., R. D. Miller, J. B. Dunbar, and S. Smullen, 2005b, Time-lapse seismic study of levees in southern Texas: 75th Annual International Meeting, Society of Exploration Geophysicists, Expanded Abstracts, 1121-1124.

Kaufmann, R.D., J. Xia, R.C. Benson, L.B. Yuhr, D.W. Casto, and C.B. Park, 2005, Evaluation of MASW data acquired with a hydrophone streamer in a shallow marine environment: Journal of Environmental and Engineering Geophysics, **16**, no. 2, 87-98.

KGS. YPG Georectified Image. Open-file Report 2010-2 CD. The University of Kansas. Lawrence, KS: Kansas Geological Survey, 14 July 2009.

Lai, C. G., and G. J. Rix, 1998, Simultaneous inversion of Rayleigh phase velocity and attenuation for near-surface site characterization: Georgia Institute of Technology, School of Civil and Environmental Engineering Report GIT-CEE/GEO-98-2.

Lourakis, M.I.A., 2005, A Brief Description of the Levenberg-Marquardt Algorithm Implementation, Institute of Computer Science (FORTH), Feb. 2005.

Louie, J. N., 2001, Faster, better: Shear-wave velocity to 100 meters depth from refraction microtremor arrays: Bulletin of the Seismological Society of America, 91, no. 2, 347–364.

Luo, Y., Xu, Y., J. Xia, R.D. Miller, Y. Xu, J. Liu, and Q. Liu, 2008, Rayleigh-wave dispersive energy imaging using a high-resolution linear radon transform: Pure and Applied Geophysics, **165**, 903-922.

Luo, Y., J. Xia, Q. Liu, and S. Xu, 2007, Joint inversion of high-frequency surface waves with fundamental and higher modes: Journal of Applied Geophysics, **62**, 375-384.

Lyon, D., 2009, The discrete fourier transform, part 4: spectral leakage: Journal of Object Technology, **8**, no. 7, 23-34.

Mapsopensource: open source map portal. Arizona Outline Map. <www.mapsopensource/arizona.html>, March 6, 2013.

Maraschini, M., F. Ernst, S. Foti, and L.V. Socco, 2010, A new misfit function for multimodal inversion of surface waves: Geophysics, **75**, G31-G43.

Mavko, G., T. Mukerji, and J. Dvorkin, 2011, The rock physics handbook: Tools for seismic analysis of porous media: Cambridge University Press, 511 p.

McDonald, E.V., G.K. Dalldorf, and S.N. Bacon, 2009, Landforms and Surface Cover of U.S. Army Yuma Proving Ground. U.S. Army, YPG Environmental Report. Reno, NV: Desert Research Institute, Division of Earth and Ecosystem Sciences.

Miller, R.D., J. Ivanov, J. Xia, S.L. Peterie, and S. Sloan, 2010a, Seismic investigations of subsidence hazards: 80th Annual International Meeting, SEG, Expanded Abstracts, 3769-3773.

Miller, R.D., O.M. Metheny, J.M. Anderson, A.R. Wedel, 2010b, Study of Unconsolidated Sediments at Joint Tunnel Test Range (JTTR) on Yuma Proving Grounds, Arizona: Open-file Report 2010-1. The University of Kansas. Lawrence, KS: Kansas Geological Survey.

Miller, R.D., S.L. Peterie, B.C. Bennett, B.T. Rickards, J.D. Kearns, O.M. Metheny, A.R. Wedel, B.A. Wedel, and J.M. Anderson, 2010c, Baseline Near-Surface Seismic Characterization at the Joint Tunnel Test Range (JTTR) on the Joint Experimentation Range Complex (JERC) Site of the Yuma Proving Grounds, Arizona. Open-file Report 2010-2. The University of Kansas. Lawrence, KS: Kansas Geological Survey.

Miller, R. D, J. Xia, C. B. Park., J. Ivanov., and E. Williams, 1999a, Using MASW to map bedrock in Olathe, KS: 69th Annual International Meeting, Society of Exploration Geophysicists, Expanded Abstracts, 433-436.

Miller, R. D., J Xia, C. B. Park, J. C. Davis, W.T. Shefchik, and L. Moore, 1999b, Seismic techniques to delineate dissolution features in the upper 1000 ft at a power plant site: 69th Annual International Meeting, Society of Exploration Geophysicists, Expanded Abstracts, 492-495.

Nazarian, S., and K. H. Stokoe II, 1984, In situ shear wave velocities from spectral analysis of surface waves: 8th Conference on Earthquake Engineering, v. 3, 31–38.

O'Neill, A., T. Campbell, and T. Matsuoka, 2008, Lateral resolution and lithological interpretation of surface-wave profiling: The Leading Edge, **27**, 1550-1563.

O'Neill, A. and T. Matsuaka, 2005, Dominant Higher Surface-wave Modes and Possible Inversion Pitfalls: Journal of Environmental and Engineering Geophysics, **10**, 185-201.

Office of National Drug Control Policy (ONDCP), 2009, National Southwest Border Counternarcotics Strategy. Governmental Policy. Washington D.C.: Executive Office of the President of the United States.

Palmer, D., 2010, Non-Uniqueness with refraction inversion – a syncline model study: Geophysical Prospecting, **58**, 203-218.

Park, C.B. and C. Taylor, 2010, 3D MASW Characterization of Sinkhole: A Pilot Study at USF Geology Park, Tampa, Fl: Proceedings of the Symposium on the Application of Geophysics to Engineering and Environmental Problems (SAGEEP 2010), Keystone, CO, April 11-15, 498-507.

Park, C. B., R. D. Miller, and J. Xia, 1999, Detection of near-surface voids using surface waves: Proceedings of the Symposium on the Application of Geophysics to Engineering and Environmental Problems (SAGEEP 1999), Oakland, CA, March 14-18, 281-286.

Park, C. B., R. D. Miller, and J. Xia, 1999, Multichannel Analysis of Surface Waves: Geophysics. **64,** 800-808.

Park, C. B., J. Xia, and R.D. Miller, 1998, Imaging dispersion curves of surface waves on multichannel record: 68th Annual International Meeting, Society of Exploration Geophysicists, Expanded Abstracts, 1377-1380.

Parolai, S., S.M. Richwalski, C. Milkereit, and D. Fah, 2006, S-wave velocity profile for earthquake engineering purposes for the Cologne area (Germany): Bulletin of Earthquake Engineering, **4**, no.4, 65–94.

Piatti, C., L.V. Socco, D. Boiero, and S. Foti, 2012, Constrained 1D joint inversion of seismic surface waves and P-refraction traveltimes: Geophysical Prospecting, Early View, 1-15.

Prasad, M., M.A. Zimmer, P.A. Berge, and B.P. Bonner, 2004, Laboratory Measurements of Veolocity and Attenuation in sediments: Lawrence Livermore National Laboratory, Society of Exploration Geophysicists, Report: UCRL-JRNL-205155, 34 p.

Press, W.H., Teukolsky, S.A., Vetterling, W.T., Flannery, B.P., 1992, Numerical Recipes in C: The Art of Scientific Computing, Second Edition (New York: Cambridge University Press).

Pujol, J., 2007, The solution of nonlinear inverse problems and Levenberg-Marquardt method: Geophysics, **72**, W1-W16.

Renalier, F., D. Jongmans, A. Savvaidis, M. Wathelet, B. Endrun, and C. Cornou, 2010, Influence of parameterization on inversion of surface wave dispersion curves and definition of an inversion strategy for sites with a strong Vs contrast: Geophysics, **75**, no. 6, B197-B209.

Richart, F. E., J.R. Hall, and R.D. Woods, 1970, Vibrations of soils and foundations: Prentice-Hall, Inc.

Richwalski, S., M. Picozzi, S. Parolai, C. Milkereit, F. Baliva, D. Albarello, K. Row-Chowdhury, H. van der Meer, and J. Zschau, 2007, Rayleigh wave dispersion curves from seismological and engineering-geotechnical methods: a comparison at the Bornheim test site (Germany): Journal of Geophysics and Engineering, **4**, 349–361

Rickards, B., 2011, Near-surface shear-wave velocity measurements in unlithified sediments, The University of Kansas, Master's Thesis.

Ryden, N., and C.B. Park, 2006, Fast simulated annealing inversion of surface waves on pavement using phase-velocity spectra: Geophysics, **71**, R49-R58.

Ryden, N., C.B. Park, P. Ulriksen, and R.D. Miller, 2004, Multimodal approach to seismic pavement testing: Journal of Geotechnical and Geoenvironmental Engineering, **130**, no. 6, 636–645.

Salem, H.S., 2000, Poisson's ratio and the porosity of surface soils and shallow sediments, determined from seismic compressional and shear wave velocities: Geotechnique, **50**, no. 4, 461-463.

Schuler, J., 2008, Joint inversion of surface waves and refracted P- and S- waves: M.S. Thesis, Eidgenössische Technische Hochschule Zurich.

Schwab, F. A. and L. Knopoff (1972). Fast surface wave and free mode computations, in Methods in computational physics, Academic Press, ed. B. A. Bolt, pp. 87–180.

Sheriff, R. E., 2002, Encyclopedic dictionary of applied geophysics: SEG Geophysical Reference Series No. 13, 4th Ed., Society of Exploration Geophysicists, Tulsa, Oklahoma, 429 pp.

Sherrod, D.R., and R.M. Tosdal, 1991, Geologic setting and tertiary structural evolution of southwestern Arizona and southeastern California: Journal of Geophysical Research, **96**, no B7, 12407-12423.

Sloan, S. D., S. L. Peterie, J. Ivanov, R. D. Miller, and J. R. McKenna, 2010, Void detection using near-surface seismic methods; in Advances in Near-Surface Seismology and Ground-Penetrating Radar, SEG Geophysical Developments Series No. 15, R. D. Miller, J. D. Bradford, and K. Holliger, eds.: Society of Exploration Geophysicists, 201-218.

Sloan, S. D., 2009, Proceedings of the European Meeting of Environmental and Engineering Geophysics (Near Surface 2009), Dublin, Ireland, September 7-9, 27-30.

Sloan, S. D., R. D. Miller, J. Ivanov, and S. L. Walters, 2009, Shear-Wave Velocity as an Indicator of Increased Stress and Failure Potential Associated with Dissolution-Mining Voids Proceedings of the Symposium on the Application of Geophysics to Engineering and Environmental Problems (SAGEEP 2009), Fort Worth, TX, March 29-April 2, 363-372.

Socco, L.A., S. Foti, and D. Boiero, 2010, Surface-wave analysis for building near-surface velocity models – Established approaches and new perspectives: Geophysics, **75**, v.5, 75A83-75A102.

Socco, L. V., D. Boiero, S. Foti, and R. Wisén, 2009, Laterally constrained inversion of ground roll from seismic reflection records: Geophysics, **74**, no. 6, G35–G45.

Socco, L.V., and D. Boiero, 2008, Improved Monte Carlo inversion of surface wave data: Geophysical Prospecting, **56**, 357-371.

Socco, L. V., C. Strobbia, and S. Foti, 2002, Multimodal interpretation of surface wave data: Proceedings of the 8th Meeting of the Environmental and Engineering Geophysics Society European Section (EEGS-ES), 21–25.

Song, Y.Y., J.P. Castagna, R.A. Black, and R.W. Knapp, 1989, Sensitivity of near-surface shear-wave velocity determination from Rayleigh and Love waves: Society of Exploration Geophysicists, Expanded Abstracts, 59th Annual Meeting, Dallas, TX, 509-512.

Stein, S. and M. Wysession, 2003, An introduction to seismology, earthquakes, and earth structure: Blackwell Publishing, 498 p.

Stephenson, W.J., J.N. Louie, S. Pullammanappallil, R.A. Williams, and J.K. Odum, 2005, Blind shear-wave velocity comparison of ReMi and MASW results with boreholes to 200m in Santa Clara Valley: Implication for earthquake ground-motion assessment, Bulletin of the Seismological Society of America, **95**, no. 6, 2506-2516.

Stokoe II, K. H., Wright, G. W., Bay, J. A., and Roesset, J. M., 1994, Characterization of geotechnical sites by SASW method, in Woods, R. D., Ed., Geophysical characterization of sites: Oxford Publishers.

Thomson, W.T. (1950). Transmission of elastic waves through a stratified solid medium, Journal of applied Physics, **21**, 89-93.

Tokimatsu, K., S. Tamura, and H. Kojima, 1992, Effects of multiple modes on Rayleigh wave dispersion, Journal of Geotechnical Engineering, **118**, 1529–1543.

Tosdal, R.M., 1990, Constraints on the tectonics of the Mule Mountains thrust system, southeast California and southwest Arizona: Journal of Geophysical Research, **95**, no. B12, 20025-20048.

Tosdal, R.M., and D.R. Sherrod, 1985, Geometry of Miocene extensional deformation, lower Colorado River Region, Southeastern California and Southwestern Arizona: Evidence for the presence of a regional low-angle normal fault: The Internet Archive, NASA, online.

U.S. Army, YPG Sector Map, U.S. Army, <www.yuma.army.mil>, August 15, 2010.

Watabe, Y. and S. Sassa, 2008, Application of MASW technology to identification of tidal flats stratigraphy and its geoenvironmental interpretation: Marine Geology, **252**, 79-88.

Wathelet, M., D. Jongmans, and M. Ohrnberger, 2004, Surface-wave inversion using a direct search algorithm and its application to ambient vibration measurements: Near Surface Geophysics, **2**, (4), 211-221.

Xia, J., R. D. Miller, X. Yixian, L. Yinhe, C. Chao, L. Jiangping, J. Ivanov, and C. Zeng, 2009, High-frequency Rayleigh-wave method: Journal of Earth Science, **20**, 563–579.

Xia, J., 2008, Multichannel analysis of surface waves inversion, Lecture Notes, Kansas Geological Survey, April 25 and 30, 2008.

Xia, J., R.D. Miller, and J. Ivanov, 2007a, Sensitivity of high-frequency Rayleigh-wave data revisited: Society of Exploration Geophysicists, Expanded Abstracts, 77th Annual Meeting, San Antonio, TX, 1142-1146.

Xia, J., J.E. Nyquist, Y. Xu, M.J. Roth, and R.D. Miller, 2007b, Feasibility of detecting near-surface feature with Rayleigh-wave diffraction: Journal of Applied Geophysics, **62**, is. 3, 244-253.

Xia, J., Y. Xu, C. Chen, R.D. Kaufmann, Y. Luo, 2006, Simple equations guide high-frequency surface-wave investigation techniques: Soil Dynamics and Earthquake Engineering, **26**, 395-403.

Xia, J., C. Chen, G. Tian, R. D. Miller, and J. Ivanov, 2005, Resolution of high-frequency Rayleigh-wave data: Journal of Environmental and Engineering Geophysics, **10**, 99–110.

Xia, J., R.D. Miller, C.B. Park, and G. Tian, 2003, Inversion of high frequency surface waves with fundamental and higher modes: Journal of Applied Geophysics, **52**, 45–57.

Xia, J., P.H. Li, M.J. Lewis, R.D. Miller, and C.B. Park, 2002, Using surface wave method to define a sinkhole impact area in a noisy environment: Proceedings of the Symposium on the Application of Geophysics to Engineering and Environmental Problems (SAGEEP 2002), Las Vegas, NV, February 10-14, CAV7.

Xia, J., R.D. Miller, C.B. Park, J.A. Hunter, and J.B. Harris, 2000, Comparing Shear-Wave Velocity Profiles from MASW with Borehole Measurements in Unconsolidated Sediments, Fraser River Delta, B.C., Canada: Journal of Environmental and Engineering Geophysics, **5**, 1-13.

Xia, J., R.D. Miller, and C. B. Park, 1999, Estimation of near-surface velocity by inversion of Rayleigh waves: Geophysics, **64**, 691-700.

Xu., C. and S.D. Butt, 2006, Evaluation of MASW techniques to image steeply dipping cavities in laterally inhomogeneous terrain: Journal of Applied Geophysics, **59**, 106-116.

Xu, Y., J. Xia, and R.D. Miller, 2006, Quantitative estimation of minimum offset for multichannel surface-wave survey with actively exciting source: Journal of Applied Geophysics, **59**, 117-125.

Yilmaz, O., M. Eser, and M. Berilgen, 2006, Seismic, geotechnical, and earthquake engineering site characterization: 76th Annual International Meeting, SEG, Expanded Abstracts, 1401–1405.

Yilmaz, O., 2001, Seismic data analysis: Processing, inversion, and interpretation of seismic data, Vol. 1: Investigations in Geophysics 10, Society of Exploration Geophysicists, Tulsa, OK. 1000 p.

Zeng, C., J. Xia, R. D. Miller, and G. P. Tsoflias, 2011, Application of the multiaxial perfectly matched layer (M-PML) to near-surface seismic modeling with Rayleigh waves: Geophysics, **76**, no. 3, T43–T52.

Zhang, S.X., L. S. Chan, and J. Xia, 2004, The selection of field acquisition parameters for dispersion images from multichannel surface wave data: Pure and Applied Geophysics, **161**, 1-17.

Zhdanov, M.S., 2002, Geophysical Inverse Theory and Regularization Problems, Methods in Geochemistry and Geophysics 36, Elsevier, Amsterdam.

11. Appendix I

Related KGS Processing of MASW/Backscatter data sets

Passive Hutchinson March 2013

Tecate/Nogales February 2013

Otay Mesa/Calexico January 2013

Passive Hutchinson October 2012

Passive Hutchinson August 2012

San Luis 2012

AFG/OCONUS 2012

AFG/OCONUS 2011

YPG December 2011

San Luis April 2011

YPG April 2011

YPG February 2011

Dugway November 2010

Otay Mesa March 2010

YPG October 2009

YPG July 2009

12. Appendix II

Equation and Variable List

Variables

x	Distance, offset	$\boldsymbol{\rho}$	Density
t	Time	$\mathbf{h}$	Thickness/Layer model
k_{X}	Spatial wavenumber	$\mathbf{J}$	Jacobian matrix
ω	Angular frequency	$\Delta\mathbf{x}$	Model minimization adjustment
f	Frequency	$\Delta\mathbf{b}$	Minimization vector
p	Slowness	$\boldsymbol{x_0}$	Initial model parameterization
τ	Tau – time transform	$\mathbf{W}/\boldsymbol{L}$	Weighting matrix
ϕ	Phase-shift	α	Damping factor
c_{R}	Rayleigh Wave phase velocity	$\mathbf{I}$	Identity matrix
$\mathbf{v_s}$	Shear-wave velocity (Vs)	$\mathbf{v_p}$	Compressional velocity (Vp)
T	Period	$\boldsymbol{\pi}$	Pi
μ	Shear modulus	k	Compressibility
$\mathbf{U}, \mathbf{\Lambda}, \mathbf{V}$	Singular-Value Decomposition Matrices		

f-k$_x$ Method

Input Data Function $F(x,t)$

$$F(x,\omega) = \int P(x,t)e^{-\mathrm{i}\omega t}\mathrm{d}t \tag{1}$$

$$F(k_{\mathrm{X}},\omega) = \int P(\omega,x)e^{\mathrm{i}k_{\mathrm{x}}x}\mathrm{d}x \tag{2}$$

Slant-Stack p-τ method

$$\text{Linear Moveout: } \tau = t - p_{\mathrm{n}}x\,, \qquad \text{for } p_{\mathrm{n}} = [p_1, p_2, \dots, p_{\mathrm{m}}] \tag{3}$$

$$\text{Slant Stack: } S(p_{\mathrm{n}}\,,\tau) = \int_x F(x, t = \tau + p_{\mathrm{n}}x)\,dx \tag{4}$$

$$S(p_{\mathrm{n}}\,,\omega) = \int_\tau S(p_{\mathrm{n}}\,,\tau)e^{\mathrm{i}\omega\tau}\mathrm{d}\tau \tag{5}$$

Phase-Shift Method

$$U(x,\omega) = \int_t F(x,t)e^{\mathrm{i}\omega t}\mathrm{d}t \tag{6}$$

$$U(x,\omega) = P(x,\omega)A(x,\omega) \tag{7}$$

$$U(x,\omega) = e^{-\mathrm{i}\Phi x}A(x,\omega), \text{where } \Phi = \omega/c_{\mathrm{R}} \tag{8}$$

$$V(\omega,\phi) = \int_x e^{\mathrm{i}\phi x}\left[\frac{U(x,\omega)}{|U(x,\omega)|}\right]\mathrm{d}x \tag{9}$$

$$= \int_x e^{\mathrm{i}(\Phi-\phi)x}\left[\frac{A(x,\omega)}{|A(x,\omega)|}\right]\mathrm{d}x$$

Inversion

$$F(\,f_{\mathrm{j}}\,, c_{\mathrm{Rj}}\,, \mathbf{v_s}\,, \mathbf{v_p}, \boldsymbol{\rho}, \mathbf{h}) \;=\; 0 \;\; ; \text{ where (j } =\; 1, 2, \dots, \mathrm{m}) \tag{10}$$

$$\mathbf{J}\Delta\boldsymbol{x} \;=\; \Delta\mathbf{b} \tag{11}$$

$$\mathbf{J_S} = -\frac{\partial F/\partial v_{\mathrm{si}}}{\partial F/\partial c_{\mathrm{Rj}}}\bigg|_{f=f_{\mathrm{j}}} \tag{12}$$

$$\Psi \;=\; \|\mathbf{J}\Delta\mathbf{x} - \Delta\mathbf{b}\|_2\,\mathbf{W}\|\mathbf{J}\Delta\mathbf{x} - \Delta\mathbf{b}\|_2 + \;\alpha\|\Delta\mathbf{x}\|_2^2 \tag{13}$$

$$\mathbf{W} = \mathbf{L}^{\boldsymbol{T}}\mathbf{L} \tag{14}$$

$$\Delta\boldsymbol{x} = (\mathbf{A}^T\mathbf{A} + \alpha\mathbf{I})^{-1}\mathbf{A}^T\mathbf{d} \tag{15}$$

$$\Delta\boldsymbol{x} = [\mathbf{V}(\boldsymbol{\Lambda}^2 + \alpha\mathbf{I})^{-1}\boldsymbol{\Lambda}\mathbf{U}^{\boldsymbol{T}}]\mathbf{d} \;\text{ or }\; \Delta\mathbf{x} = \;[\mathrm{G}]^{-1}\mathbf{d} \tag{16}$$

13. Appendix III

Constrained-Parameterization MASW Flow Diagram

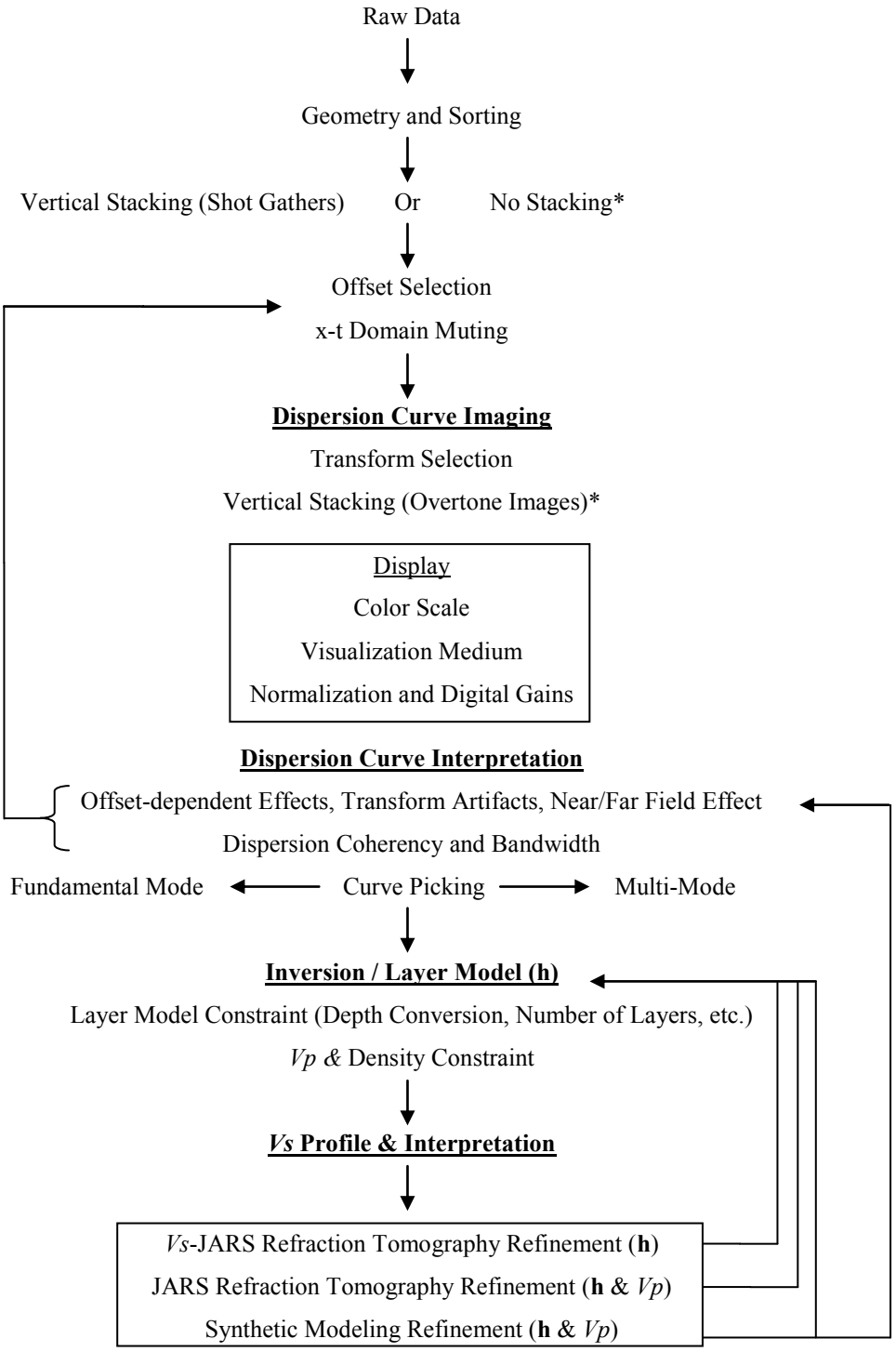

14. Appendix IV

Abbreviations List

1D	One-dimensional
2D	Two-dimensional
DC	Dispersion Curve
e.g.	*exempli gratia*; for example
HM	Higher mode
HRLRT	High-Resolution Linear Radon Transform
HVL	High-velocity layer
Hz	Hertz
i.e.	*id est*; that is/in other words
IRTP	Inverse Refraction Travel-Time Problem
JARS	Joint Analysis of Refractions with Surface Waves
JCTD	Joint Capability Technology Demonstration
JTTR	Joint Tunnel Test Range
KGS	Kansas Geological Survey
LTU	Line Tap Unit
LVL	Low-velocity Layer
m	meter
MASW	Multichannel Analysis of Surface Waves
ONDCP	Office of National Drug Control Policy
OT	Overtone Image
P-	Primary, compressional-wave
RAWD	Rubber-band Assisted Weight-Drop
s	second

S-	Secondary, shear-wave
SASW	Spectral analysis of surface waves
sec	second
SWM	Surface Wave Methods
YPG	Yuma Proving Ground
USCS	Unified Soil Classification System
USDA-NRCS	United States Department of Agriculture-Natural Resources Conservation Service
Vp	Compressional-wave velocity
vs.	versus
Vs	Shear-wave velocity
Vs-JARS	Mode-consistent *Vs* Joint Analysis of Refractions with Surface waves